3-10-2010

A Structural Dynamic Analysis of a Manduca Sexta Forewing

Travis W. Sims

A STRUCTURAL DYNAMIC ANALYSIS OF A *MANDUCA SEXTA* FOREWING

THESIS

Travis W. Sims, 2d Lt, USAF

AFIT/GAE/ENY/10-M22

DEPARTMENT OF THE AIR FORCE
AIR UNIVERSITY

AIR FORCE INSTITUTE OF TECHNOLOGY

Wright-Patterson Air Force Base, Ohio

AFIT/GAE/ENY/10-M22

A STRUCTURAL DYNAMIC ANALYSIS OF A *MANDUCA SEXTA* FOREWING

THESIS

Presented to the Faculty

Department of Aeronautics and Astronautics

Graduate School of Engineering and Management

Air Force Institute of Technology

Air University

Air Education and Training Command

In Partial Fulfillment of the Requirements for the

Degree of Master of Science in Aeronautical Engineering

Travis W. Sims, BS

Second Lieutenant, USAF

March 2010

AFIT/GAE/ENY/10-M22

A STRUCTURAL DYNAMIC ANALYSIS OF A *MANDUCA SEXTA* FOREWING

Travis W. Sims, BS

Second Lieutenant, USAF

Approved:

//signed//	05 Mar 2010
Dr. Anthony Palazotto (Chairman)	Date
//signed//	05 Mar 2010
Dr. Richard Cobb (Member)	Date
//signed//	05 Mar 2010
Lt Col Eric Swenson, PhD (Member)	Date

Abstract

Micro air vehicles (MAVs) are intended for future intelligence, surveillance, and reconnaissance use. To adequately fulfill a clandestine capacity, MAVs must operate in close proximity to their intended target without eliciting counter-observation. This objective, along with DARPA's constraint of a sub-15 centimeter span, requires future MAVs to mimic insect appearance and flight characteristics. This thesis describes an experimental method for conducting a structural analysis of a *Manduca Sexta* (hawkmoth) forewing. Geometry is captured via computed tomography (CT), and frequency data is collected using laser vibrometry in air and vacuum. A finite element (FE) model is constructed using quadratic beams and general-purpose shell elements, and an eigenanalysis is conducted. A preliminary verification of the FE model is carried out to ensure the *Manduca Sexta* forewing is adequately characterized, providing a basis for future fluid-structural interaction computations. Included is a study regarding the aeroelastic effects on flapping-wing insect flight, and an analysis of the structural dynamic anomalies of conventional, flat, semi-rigid flapping wings.

Experimental tests revealed the first three modes of a clamped *Manduca Sexta* wing in vacuum are 86 Hz, 106 Hz, and 155 Hz; tests in air reveal a frequency shift of 26.5% from vacuum, indicating a possible aeroelastic contribution to frequency response. The finite element model produced first three modes of 84.6 Hz, 106.1 Hz, and 317.7 Hz, indicating that the model is limited to the second wing mode and lower frequencies. Possible sources of error include poor geometric modeling due to low CT resolution, inadequate modeling of camber, and inaccurate estimation of material properties.

Acknowledgements

First, I would like to extend a very special thanks to my advisor, Dr. Anthony Palazotto. Without his constant guidance, thought-provoking inquiries, and patience, this effort would certainly have been impossible. Next, thanks to Major Aaron Norris for his mentoring, academic forerunning, and the countless hours he donated to help me succeed. Thanks also go to Dr. Richard Cobb and Dr. Rashid Abu Al-Rub for the time and effort they spent teaching and troubleshooting along the way. Further thanks go to my brother. He is a true code-warrior, without whose expertise I would have been unable to finish the modeling process. My heartfelt gratitude goes to my beautiful wife for her love, patience, support, and willingness to hear me ramble about all things nerdy – and even pretend to be interested. Most of all, I thank God for all His blessings. "What is man, that you are mindful of him? [Psalm 8:4]"

Table of Contents

Page

Page

List of Figures

Page

Page

Page

Page

Page

List of Tables

List of Abbreviations

A STRUCTURAL DYNAMIC ANALYSIS

OF A *MANDUCA SEXTA* FOREWING

I. Introduction

1.1. Background

Over the course of last two decades, the demand for unmanned intelligence, surveillance and reconnaissance (ISR) assets has grown at an extraordinary pace. Physical separation of an aircraft and its human operator has provided unprecedented loiter times, range, low-cost compared to equivalent manned systems, and pilot safety. To supplement future ISR capabilities, many have proposed "micro" air vehicles (MAVs) that would revolutionize the field of remote sensing with their low cost[1], extreme maneuverability, and inconspicuous operation. As part of their proposed mission, these vehicles will have a wingspan of less than 15 centimeters, complete with flapping wings, to minimize counter-observation[2] [27]. If successfully manufactured, the MAV of the future will be capable of a multitude of close-quarters reconnaissance tasks, ranging from battlefield operations to safety inspections of civilian structures. Table 1 outlines the Defense Advanced Research Projects Agency's (DARPA) vision for the MAV [38].

A brief look at any conventional flight-line reveals the stark contrast between current aircraft design and that of the proposed MAV. Today, all conventional, powered aircraft feature prominent engines with unnatural-looking wings. Moreover, a primary goal in wing design is maintaining structural integrity by reducing the magnitude of structural oscillations. Even

[1] Current specifications are for MAVs to cost less than approximately $1,500 (2009 USD) [27].
[2] Minimizing counter-observation is not only visual. Detecting an appropriately designed MAV out of a crowd of insects with a radar would be an extraordinary feat.

bounded harmonic responses – such as limit cycle oscillations – are avoided to circumvent material fatigue [23].

Table 1. MAV Design Requirements [38]

Specification	Requirements	Details
Size	< 15.24 cm	Maximum Dimension
Weight	~ 100 g	Objective GTOW
Range	1 to 10 km	Operational range
Endurance	60 min	Loiter time on station
Altitude	< 150 m	Operational ceiling
Speed	15 m/s	Maximum flight speed
Payload	20 g	Mission dependent
Cost	$1,500	Maximum cost, 2009 USD

Turning to nature for insight into future MAV designs reveals a sharp departure from over a century of design practice: not only are insect wing oscillations permitted, they are abundant, highly-efficient, flight mechanisms [28]. Following in these biological footsteps, the micro air vehicle of the future will be purposely designed with flapping wings, closely mimicking insect flight. This fundamental shift from quasi-rigid wings – be they fixed or rotary – with separate power plants, to a flexible airfoil that integrates the generation of lift and thrust, constitutes a dramatic change in design philosophy. Through research, the ubiquitous flying insects serve as a blueprint from which structural engineers might learn important design criteria; among these insects is the *Manduca Sexta*, or hawkmoth (see Figure 1) [20]. One of the most notable advantages of mimicking *Manduca Sextae* is that they lie within the bounds of DARPA's MAV requirements in Table 1 [29].

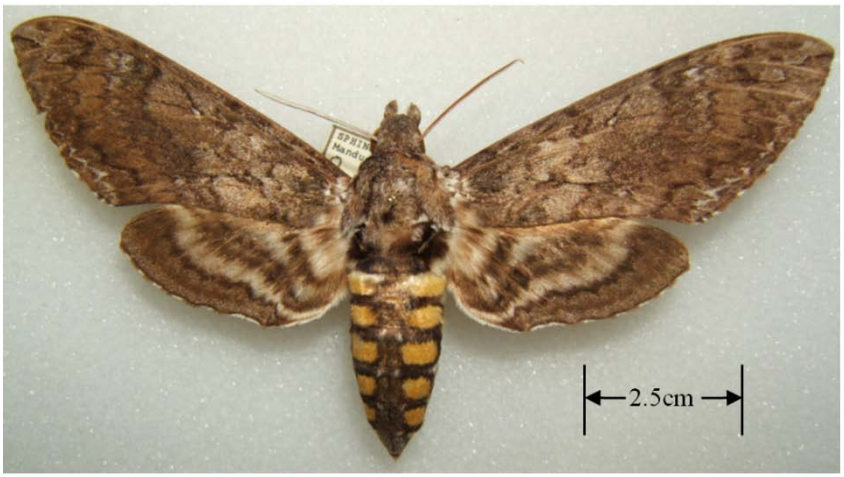

Figure 1: An adult, female *Manduca Sexta* (Hawkmoth) [21].

Many biologists and entomologists have studied the mechanics of *Manduca Sexta* flight. During these studies and ensuing debates, several fundamental, structural questions arose. To date, published research has not conclusively addressed such important issues as the magnitude of aeroelastic contributions, the structural linearity of the wings, the natural frequencies and modeshapes of the wings, or the level of sophistication required to manufacture a wing of similar capabilities and characteristics. With these questions unanswered, it is impossible to produce a validated structural model that might be useful in future numerical studies.

1.2. Research Objectives

The *Manduca Sexta* has been identified as an ideal research candidate to assist the study of insect flight. Still, there are many questions that remain unanswered by previous work. Does the *Manduca Sexta* beat its wings near its natural frequency? Is the hawkmoth's forewing a linear or nonlinear structure? Is the response dominated by inertial forces or aeroelastic effects – or both? What level of model sophistication is necessary to adequately represent biological wings? Asked another way, what simplifications could a manufacturer of synthetic *Manduca Sexta* forewings make to achieve structural characteristics similar to the biological wing?

Answering these questions requires numerical analyses of the structural and fluid mechanics that dominate *Manduca Sexta* wings. Furthermore, fluid-structural interactions cannot be adequately modeled without first producing a validated structural model. Therefore, the objective of this work is to produce a finite element model of a *Manduca Sexta* forewing grounded in experimental vibration testing. In so doing, many of the above questions are addressed and answered, laying the foundation for future work.

In an effort to elucidate the above issues, liberated wings from *Manduca Sextae* are used to pursue two research endeavors. First, the natural modes (frequencies) and modeshapes of the hawkmoth forewings are identified via laser vibrometry. Testing is accomplished in air and vacuum, to observe aeroelastic effects. Second, a finite element model capable of representing the observed modal behavior is developed and analyzed.

1.3. Motivation

The pace of unmanned aerial vehicle (UAV) development and operation is currently at an all-time historical high, with no apparent end in sight. World air forces of all sizes, private corporations, and even terrorist groups currently operate UAVs for purposes ranging from weather observation to munitions delivery [36]. As the number of UAVs in existence grows, it is only natural that the level of specialization of these systems also increases. Due to the widely-recognized potential afforded by MAVs, there are a multitude of nations with ongoing research and development programs, as shown in Figure 2 [29]. Micro air vehicle development may prove to be a critical step in keeping America's technological edge on the battlefield.

To date, the vast majority of MAV research is concentrated in the fields of fluid mechanics and controls, with a small minority – about 10% – in structures [29]. As a result, little work has concentrated in structural dynamics of MAVs, with most of the work focusing on fluid-

structural interaction. Even less research has focused on the structural dynamics of insect wings, and their applicability to bio-inspired designs.

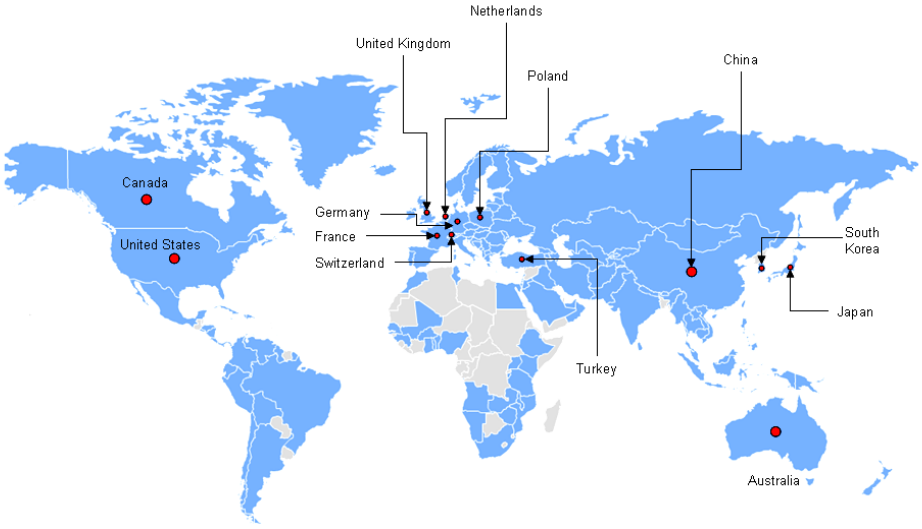

Figure 2: International MAV research locations. Major contributors are noted by name [29].

1.4. Flapping as a Flight Mechanism

In their work at the Georgia Institute of Technology, Michelson and Reece [28] produced several compelling arguments for flapping wing flight as the preferred mechanism for "stealthy" MAVs. Their rationale for selecting flapping wings over fixed-wing or rotary flight was based upon three criteria: necessary flight speed, energy efficiency, and stealthiness. The following three paragraphs are a summary of their conclusions:

Since MAVs will likely be operated in urban (including indoor) environments, reaction-time and automated obstacle avoidance are critical to operational success. Fixed wing designs require increased forward velocity to sustain flight, minimizing this precious reaction-time. Moreover, fixed-wing designs neither appear nor behave like similarly-sized biological specimens, increasing the probability of counter-observation. Thus, fixed-wing MAVs are ill-suited for their intended task.

Rotary-wing aircraft benefit from greater maneuverability at low flight-speeds, and are able to hover. Several commercial helicopters slightly larger than the MAV class already exist with high-resolution cameras (1080p[3]). These devices transmit at frequencies ranging from 80 MHz (FM) to 10 GHz (X-Band); one example is shown in Figure 3 [17].

Figure 3: The DraganFlyer X6 commercial UAV with a high-resolution (1080p) camera, has an 85 cm span [3].

Flapping wings are in many ways a compromise between fixed and rotary wing designs. As evidenced in nature, flapping wings are capable of low-speed flight and hovering, maximizing reaction time and observation capability. Like fixed-wing aircraft, flapping wing vehicles have chordwise rigidity, allowing them to expend less energy by gliding. Finally, flapping wings use varying wing stroke amplitudes, producing an overall average audible energy less than rotary wings.

Although not addressed by Michelson and Reece, it should be noted that several hybrid designs have been tested to address the issues listed above. Figure 4 shows one such example, the Sikorsky S-72 X-Wing hybrid configuration aircraft [42]. A significant benefit of the stopped rotor, or X-Wing, configuration is its ability to capitalize on the maneuverability of a

[3] 1080p is a video resolution standard with 1920 x 1080 pixels, updated sequentially in each frame [1].

helicopter and efficiency of a fixed wing aircraft. Although the S-72 is a manned aircraft with an 18.9 meter span, its capabilities could be ported to the MAV class.

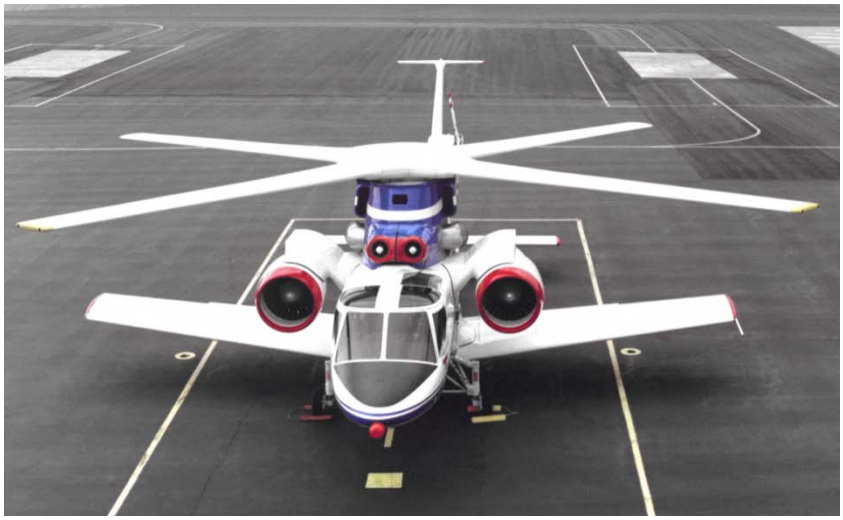

Figure 4: Sikorsky S-72 X-Wing hybrid, manned rotorcraft, 1986 [4].

Despite its design advantages, X-Wing hybrids are still comprised of unnatural-looking components, and emit a constant, audible whine. Additionally, hybrid designs such as the S-72 and the V-22 Osprey suffer from added weight due to the required system complexity [5], a challenge not easily overcome by MAVs.

1.5. Species Selection

Having settled on a flapping wing design, with the intention of producing an MAV easily mistaken for an insect, one begins the tedious task of selecting an insect to model. Certainly there are a plethora of species that lie well within the sub-15 centimeter wingspan dictated by DARPA, each with its own unique set of structural and motive behaviors. The challenge of selection is ensuring that the species is sufficiently "typical" – else any knowledge gained during the experimental and modeling processes might be too narrowly focused for broad design and application.

University of Cambridge researchers Willmott and Ellington reported the following regarding the *Manduca Sexta* [40]:

> *The wingbeat kinematics contain the major elements of which have been consistently identified in other insect species, but without any of the marked idiosyncrasies which have been seen in certain groups…The stroke amplitude is close to the value of 120° that is often cited as typical for insects* [39]*...The hawkmoth, therefore, offers a reasonably generalized wingbeat*.

Another important facet of the *Manduca Sexta* is the consistency of its wing structure and deflection from specimen to specimen. Willmott and Ellington go on to state [40],

> *The* Manduca Sexta *wingbeat proved to be remarkably consistent. Significant intraspecific variation has been reported for many insect groups including butterflies* [1] *and flies* [8]. *However, the variation in kinematics between successive wingbeats, and also between individuals, was small in the current study.*

Finally, the *Manduca Sexta* is consistent in the frequency of its wingbeat. During wind-tunnel testing, Willmott and Ellington found multiple specimens to exhibit flapping frequencies between 24.8 and 26.5 Hz, a narrow band independent of flight speed [40].

Although the *Manduca Sexta* is a four-winged synchronous flapper, Jantzen and Eisner experimentally determined that the hawkmoth can fly without its rear wings [24]. Similarly, Zhao and Deng [43] used a six-component force balance to the compute lift and drag coefficients of *Manduca Sexta* wings. Using these values, Zhao and Deng verified that the majority of the in-flight power distribution is contained in the forewings. Based on the above, sufficient evidence exists to select the *Manduca Sexta* forewing as a prototypical basis for studying flapping wing flight. The design is evidently viable, since the hawkmoth is capable of flight – even without rear wings.

1.6. System Identification

After successfully identifying the *Manduca Sexta* as an insect with reasonably typical wingbeat characteristics, Willmott and Ellington posited the following [40]:

> *The flight musculature must function at the natural resonant frequency of the mechanical system involving the thorax and wings.…Insects appear, therefore, to fly within the narrow range of frequencies which maximizes the mechanical performance of their flight muscles.*

This hypothesis – that *Manduca Sextae* operate near or at a resonant frequency of their wings where displacement is maximized – is based upon two factors. First, the *Manduca Sexta* has muscles in its thorax, but none in the wings. This configuration produces a response similar to a cantilever beam undergoing harmonic base motion. Second, multiple studies demonstrate a narrow wingbeat frequency range.

While these lemmata are correct, it is unclear whether hawkmoths are highly efficient flyers that achieve maximum deflection with minimal muscular input – that is, operate near a resonant frequency. Without validation, this inherent assumption seems to be generally accepted in the field of entomology [10, 15].

From a structural dynamics standpoint, one must consider the curious ability for the *Manduca Sexta* to fly without its rear wings, if indeed the forewings operate close to a natural frequency. If the forewing is lightly damped, the hawkmoth would be able to generate significant displacements – thus lift – by simply modulating its beat frequency. With a sudden, dramatic increase in energy, the *Manduca Sexta* would then be more than capable of evasive maneuvers, eliminating the need for rear wings altogether. Since the *Manduca Sexta* retains its rear wings for evasive procedures [24], it seems unlikely that the hawkmoth "must" operate near resonance, as posited by Willmott and Ellington [40]. If large damping is the reason for rear wing retention, the magnitude of the wing displacement would be small, even near resonance –

also casting doubt on the basis of the claim. Therefore, if damping is present, it must not lie near either of the extrema. A counter argument in support of Willmott and Ellington is the possibility that aeroelasticity is a moderate damping mechanism. If so, this moderate damping would both allow operation near resonance and require the presence of rear wings.

1.7. The Aeroelastic Question

After completing a review of over 700 papers archived by the American Institute of Aeronautics and Astronautics (AIAA), Norris [29] was unable to find any conclusive evidence supporting or disproving aeroelasticity as a dominant factor in the response of flapping wing flight. Instead, he reported a "controversy among scholars in the field" [29] regarding the issue. As a result, many researchers currently utilize aeroelastic fluid-structural interaction methods, either out of uncertainty or foregone conclusion.

Among the most prominent voices in the debate regarding aeroelasticity (specifically in *Manduca Sextae*) are Combes and Daniel [10, 11, 12, 13]. Combes and Daniel carried out their studies on the basis that understanding the fluid-structural interactions surrounding the hawkmoth's forewing helps guide the modeling process. If aeroelastic effects are negligible – that is, there is little or no feedback between wing deformations and fluid mechanics – they may be omitted during modeling [12]. This omission constitutes a dramatic, desirable simplification but cannot be made without substantiation.

Examining the degree to which hawkmoths are affected by aeroelastic forces, Combes and Daniel performed static loading tests on forewings of *Manduca Sextae*, as shown in Figure 5 and Figure 6 [11, 12]. During these tests, Combes and Daniel used a pin to apply a point load to various locations on the wing, and collect deflection data. From these deflection data, Combes and Daniel observed that wing stiffness varies with spanwise location, and produced a finite

element model to represent their findings. Inherent in their methodology is the assumption that structural (static) stiffness, *EI*, is a function of span. Since *I*, the moment of inertia, is a function of spanwise length, so is static stiffness – even if *E*, Young's modulus, were constant.[4]

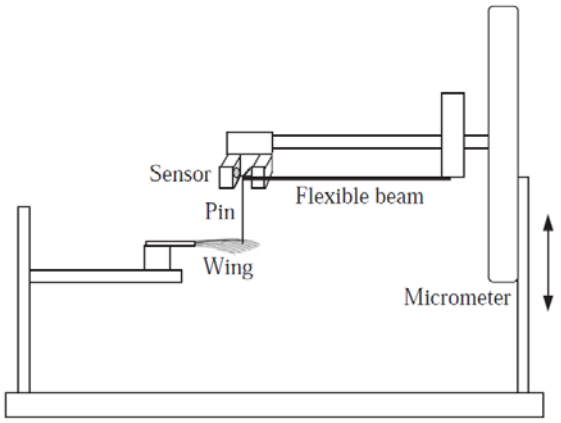

Figure 5: Static test setup used by Combes and Daniel [10].

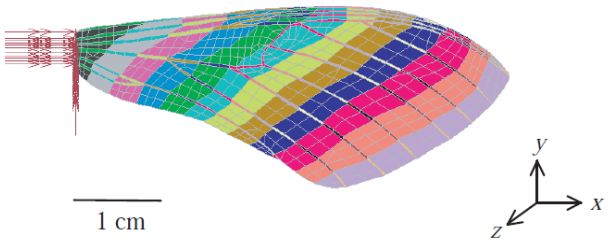

Figure 6: Finite element model developed by Combes and Daniel. Color bands denote stiffness as a function of spanwise distance [11].

Following their stiffness measurements, Combes and Daniel went on to perform flapping tests in air and helium [11]. During these experiments, hawkmoth forewings were recorded with high speed video. Observing their footage, Combes and Daniel concluded that aeroelasticity is a function of wing size and the spanwise stiffness distribution they previously calculated. Based on their static stiffness tests, Combes and Daniel developed a parameter to describe the degree to which aeroelasticity affects various flapping wing designs.

During their load analysis, Combes and Daniel, citing Gordon [19], used an Euler-Bernoulli beam formulation to compute stiffness as a function of wingspan [10]. Several assumptions underlie Euler-Bernoulli theory: beams are prismatic, isotropic, homogeneous structures, loaded in a plane of symmetry, with plane sections remaining plane. Furthermore,

[4] In this case, it is more likely that *E* is a weight modulus based on the moduli and volume fractions of the veins and membrane. Thus, the wing may be thought of as a composite material, obeying the rule of mixtures [16].

beams are characterized by one dimension that is greater than the other two by at least one order of magnitude, and undergo small deformations [18]. Unfortunately, inspecting *Manduca Sexta* wings reveals a very different picture. The forewings are non-prismatic, non-homogeneous plates with a venation pattern resembling composite fibers. Noting this contrast, Combes and Daniel acknowledged the possibility of a "systematic error in the reported values, which could potentially underlie the observed scaling relationships" [10].

In many ways, Combes and Daniel took a remarkable first step in studying the mechanisms behind insect flight. Certainly, their work is widely cited, highly publicized, and often debated. Their work has achieved prestige, as well as been mocked as conjecture [9]. Gogulapati, Friedman and Shy argued in support of Combes and Daniel, based on their finite element analysis of a flapping box-beam [20]. Chen, Chen and Chou argued against Combes and Daniel on the basis of their *in vacuo* photonic frequency analysis of a dragonfly wing [9].

Fortunately, applying classic structural dynamics theory serves to settle such an impassioned debate. While Combes and Daniel correctly identified the need for flapping tests to determine aeroelastic effects, their work was based upon previous static loading computations. As previously discussed, the validity of these findings is questionable, due to the simplifying assumptions inherent in Euler-Bernoulli beam theory. Second, static loading does not adequately characterize a structure's response to oscillations – structural dynamics theory is required.

The field of analytical structural dynamics is predicated upon determining equations of motion, applying an input (or forcing function), and solving for resultant singularities in those equations of motion [23, 26]. While computational methods exist, their purpose is to approximate singularities via numerical convergence, where analytical methods are intractable [14]. Combes and Daniel did invoke the finite element method (FEM), but only verify their

load-deflection tests [10]. Gogulapati, Friedman and Shy also utilized FEM, but their objective was to study fluid-structural interactions (FSI); due to the limitations of computational fluid dynamics (CFD) solvers, they modeled a beam [20]. The applicability of findings based on a box-beam model to a *Manduca Sexta* forewing is questionable.

In an attempt to eliminate concerns arising from the above methods, Chen, Chen, and Chou conducted a frequency analysis of a dragonfly [9]. Unfortunately, their photogrammetric analysis technique required them to paint metallic dots on the wing, adding nearly 30% to its mass (Figure 7). Moreover, Chen, Chen, and Chou failed to adequately refute the aeroelastic effects reported by Combes and Daniel, since their vacuum testing eliminated the possibility of aerodynamic contributions. Still, Chen, Chen, and Chou deserve credit for introducing structural dynamics testing to an aeroelasticity debate dominated by biologists and entomologists.

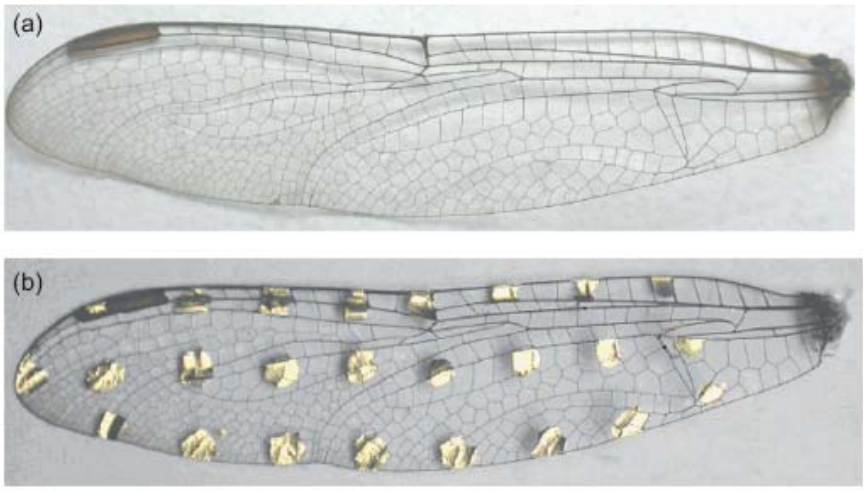

Figure 7: (a) Freshly liberated dragonfly wing; (b) painted wing used by Chen, Chen, and Chou [9].

1.8. Selected Approach

Borrowing from the best of approaches of Combes and Daniel [12] and Chen, Chen, and Chou [9], a motor was used to flap a liberated *Manduca Sexta* forewing at random frequencies

(technically, pseudo-random). A Polytec® scanning laser vibrometer was used to determine modes and modeshapes ,via fast Fourier transform (FFT), from frequencies approaching zero up to one-thousand Hertz. Unlike the method used by Chen, Chen, and Chou, the laser vibrometer offers the advantage of noninvasive measurement. The specimen remains unaltered, contributing neither mass nor stiffness.

Again combining the methods of Combes and Daniel and Chen, Chen, and Chou, tests were conducted in air at room temperature and pressure, then repeated in vacuum. Frequency response functions (FRFs) of both cases were compared to evaluate the extent to which aeroelastic forces affect flapping wings.

Computed tomography (CT) scans provided detailed X-Ray images of the *Manduca Sexta* vein structure, and were used as the geometric basis for modeling. A finite element model was constructed using SolidWorks®, Abaqus®[5], and CoordGen[6] [35]. Finally, the results of the frequency analysis in Abaqus were compared to the eigenvalues and eigenvectors produced by the Polytec scanning laser vibrometry studies. A preliminary investigation into what level of geometric simplification might be possible when manufacturing a synthetic *Manduca Sexta* forewing was also conducted.

Such simplifications are desirable for three reasons. First, manufacturing costs scale with design complexity. Since cost reduction is one of many attractive aspects of future MAVs, trade studies of simplification versus performance are valuable tools. Second, many fluid-structural interaction (FSI) codes do not interact well – or at all – with non-beam elements. The simpler the finite element model, the more feasible future CFD analyses become. Third, the proposed clandestine nature of the MAV warrants designing many types of synthetic insect look-alikes,

[5] "SolidWorks" and "Abaqus" are registered trademarks, and are proprietary works of Dassault Systemes SA.
[6] "CoordGen" is copyrighted, open-source work, published under license in Appendix A – CoordGen.

since not all insects are indigenous to all parts of the globe. In this sense, less specific wing designs offer increased flexibility in application, potentially reducing future research and development costs.

1.9. Document Overview

The following four chapters are arranged in chronological order. Chapter II discusses experimental work conducted at the Air Force Institute of Technology (AFIT) and at the Materials Directorate of the Air Force Research Laboratory (AFRL). The experimental data in Chapter II are the foundation upon which subsequent chapters are built. Chapter III details several finite element and numerical studies conducted before proceeding with the monumental task of producing a final, finite element model. These analyses are custom-tailored problems that represent the characteristics of the final model, but are far more tractable. Chapter IV is the results and discussion section. Here, such topics as aeroelastic effects, frequency analysis, tested biological and synthetic specimens, and wing stress are presented. Chapter V reviews the highlights of each of the preceding chapters to present conclusions and opportunities for future endeavors.

The appendices follow Chapter V, and contain supplemental material, from which one might gain further insight into the methods used, source code, instructions for those wishing to conduct similar, future research, and general information outside the primary scope of this work. Finally, a bibliography contains any references used in preparation of this document.

II. Experimental Methods

The primary focus during the experimental phase of studying the *Manduca Sexta* was recording the natural frequencies and associated modeshapes of the forewings. In an effort to reduce any possible anatomical variations, only females were studied. Laser vibrometry was selected as the preferred method of frequency extraction due to its noninvasive nature, repeatability, and rapid test times. The wings were mounted to a motor, exciting the wing at pseudo-random frequencies up to approximately 400 Hz. Time domain data was acquired with velocity decoders and converted to the frequency domain via the fast Fourier transform (FFT).

Tests were conducted in air and in vacuum (less than 530 Pa., or approximately $1/150^{th}$ of an atmosphere) to investigate the possible aeroelastic contributions during flight. Clamped boundary conditions were verified by comparing laser scans of beams to analytical solutions. The results of each of these tests are found in Table 2 and Table 3.

2.1. Experimental Setup

The frequency analysis of a *Manduca Sexta* forewing was conducted using the Polytec PSV-400 scanning laser vibrometer. Wings were mounted into a foam-lined clamp, which was bolted to a motor. The motor was connected to an amplifier that received signals from the Polytec function generator. The motor and wing were encased in a transparent, acrylic vacuum, angled to prevent back-scatter to the laser head (see Figure 8). During vacuum tests, the pressure was held constant at room temperature and approximately 530 Pa. During tests in air, the vacuum chamber was closed, but kept at room temperature and pressure.

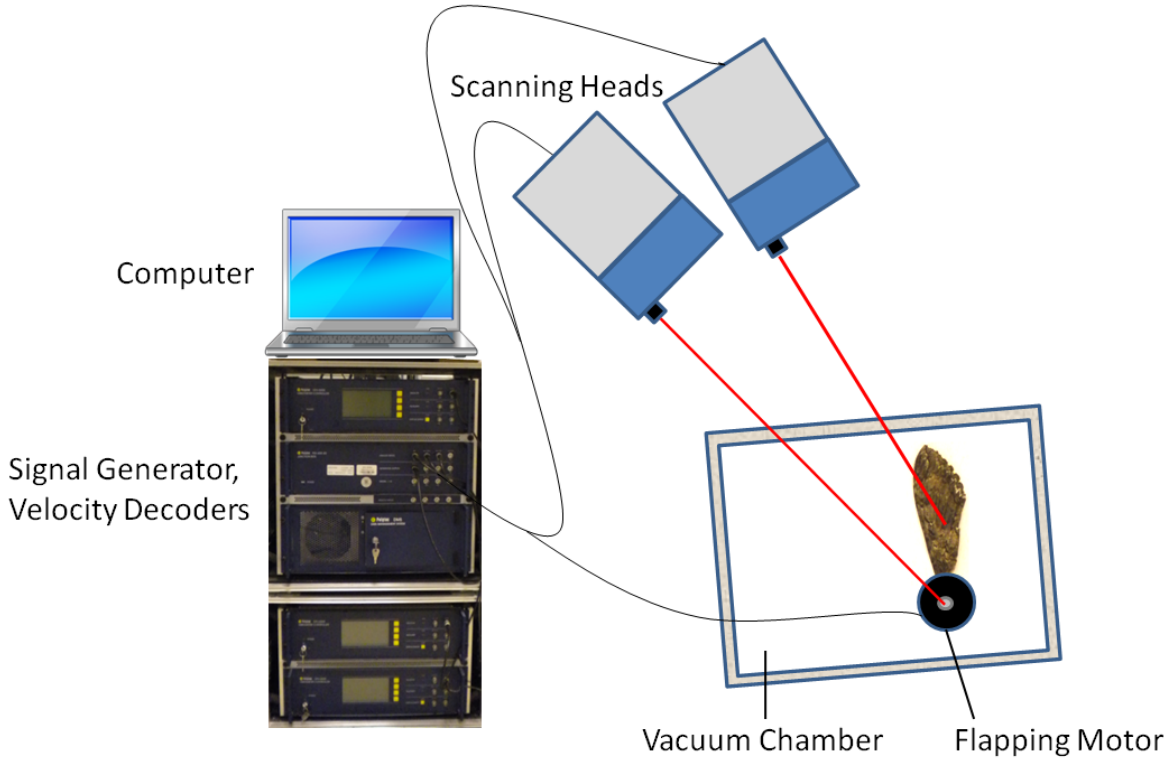

Figure 8: Schematic of experimental setup.

Two laser heads were used while conducting frequency extraction tests. A reference laser focused on the bolt-head holding the wing clamp in place, while the other laser scanned the wing, as shown in Figure 9. The scanning laser followed a pre-set pattern of scan points over the surface of the wing. This scanning point cloud was sufficiently dense, and an average of five scans per point was recorded and processed during the FFT. During the tests, the motor flapped the wing at very low amplitudes[7], to minimize any aeroelastic influence that might not be present during normal operation by the *Manduca Sexta*. A pseudo-random signal drove the motor at approximately 0.2 volts, at frequencies up to approximately 400 Hz. All signal processing, including coherence plots and frequency response function plots, was automatically achieved with Polytec's proprietary software suite.

[7] While not quantified, these amplitudes were small enough that they were barely visible with the naked eye.

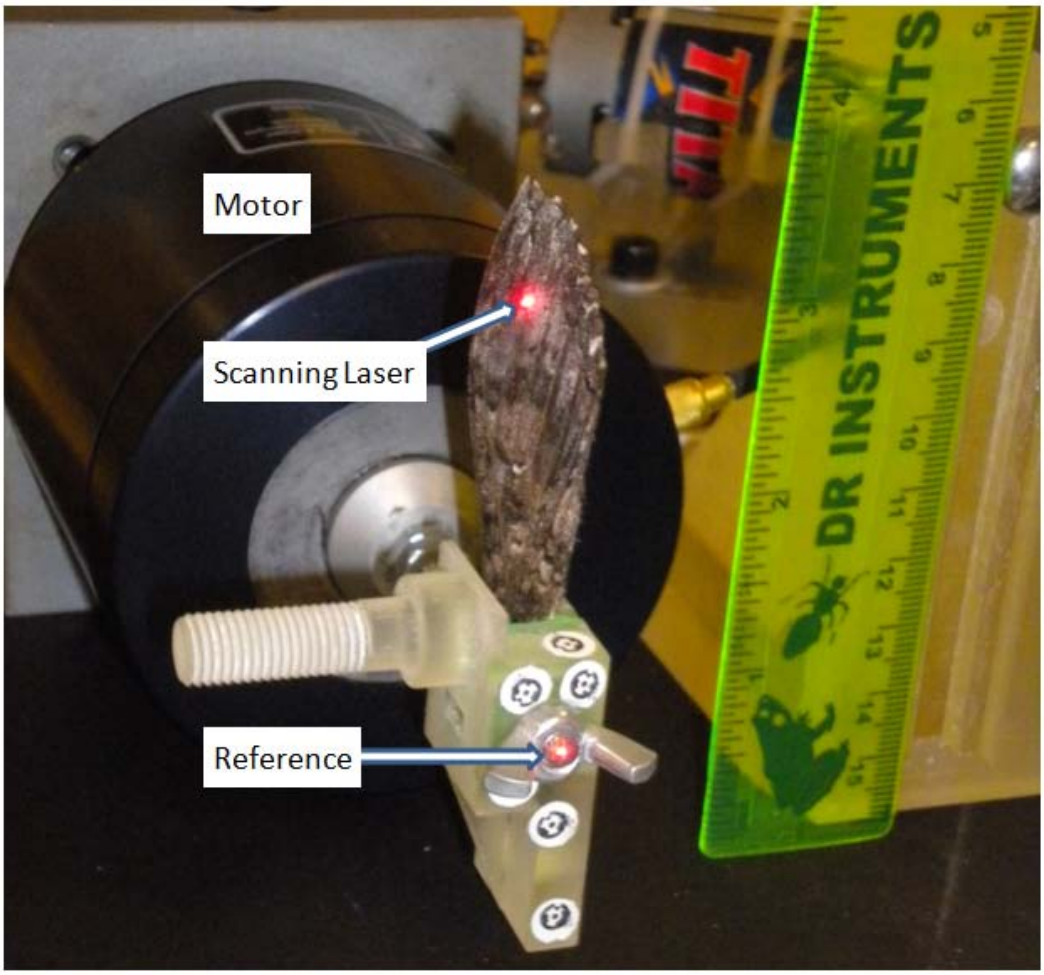

Figure 9: Wing motor and laser configuration used during testing.

Vacuum tests were conducted inside an Abbess Instruments stainless steel / acrylic vacuum. The vacuum chamber is a cube, transparent on five sides, each measuring 24 inches. To ensure no ambient air leaked into the vacuum during testing, a digital pressure gage is attached to the vacuum, and monitored during testing. The vacuum was manually operated, and was not configured to automatically compensate for any (small) changes in pressure; however, the vacuum is sufficiently sealed to provide quasi-equilibrium, at no point during vacuum testing did the pressure exceed the 4 Torr self-imposed limit. Tests in air were held at room temperature and pressure, by allowing the vacuum relieving valve to remain open.

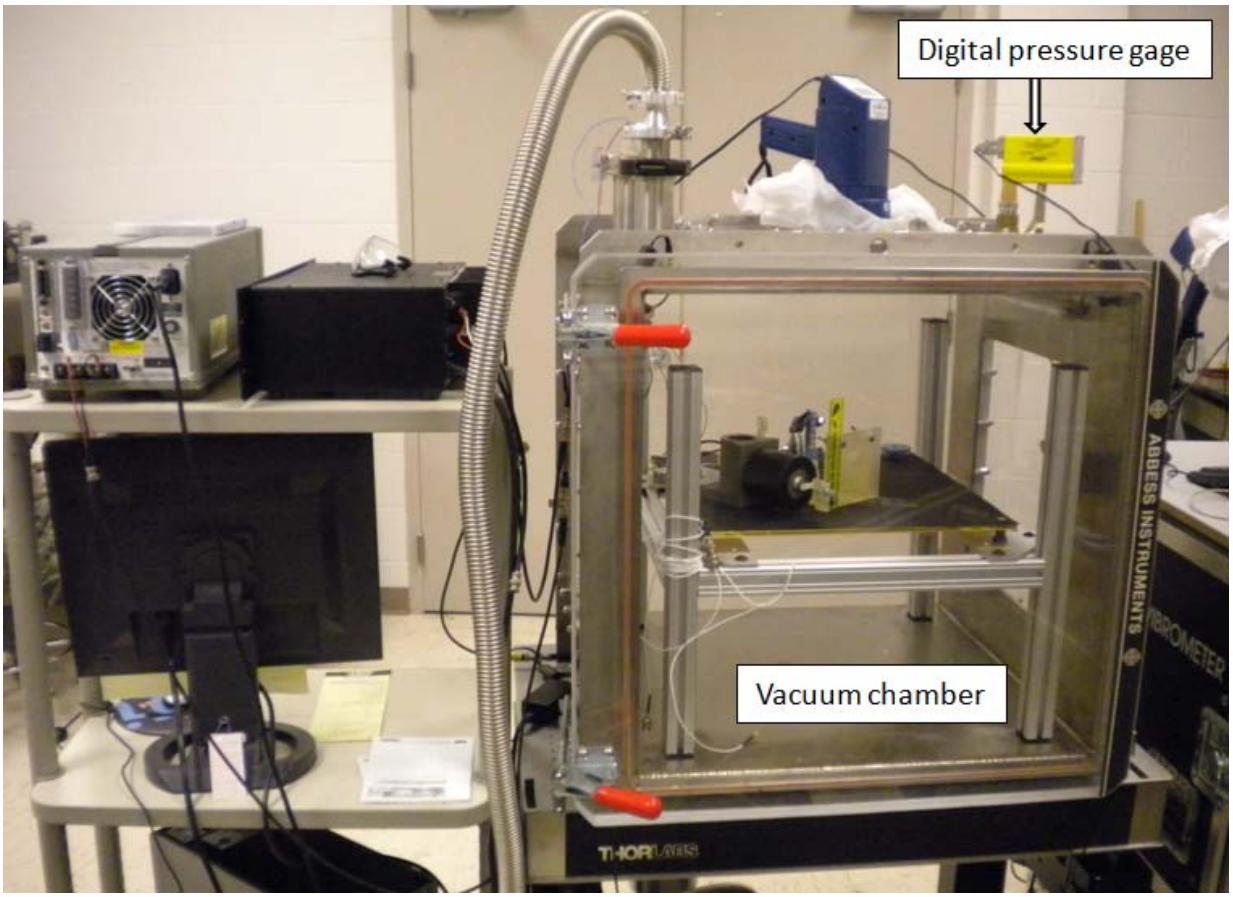

Figure 10: Abbess Instruments vacuum chamber used during testing.

2.2. Wing Preparation

Before any vibration testing can be conducted, the forewings must be liberated from the *Manduca Sexta*. In an effort to minimize any unnecessary, potential suffering, the insects were cooled in a refrigerator for approximately thirty minutes, then checked for responsiveness. Using a scalpel, the wings were removed by an incision parallel to the body, and immediately distal of the wing-thorax adjacency (shown in Figure 11). During this process, great care was taken to avoid damaging the wing prior to testing.

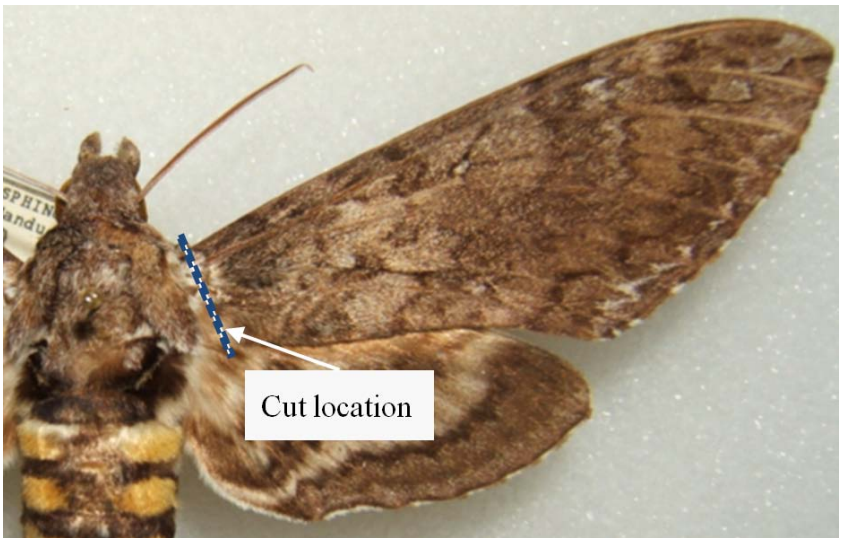

Figure 11: Cut location during wing liberation [21].

Observed during the wing liberation process was a natural camber in the *Manduca Sexta* forewing. In order to measure the frequency characteristics of the wing, it must be placed inside a rigid clamp. Unfortunately, clamping the wing flattens its arched center, thus changing the shape of the wing and producing internal stress. These changes in geometry and internal stress alter the natural frequencies and mode shapes, an unacceptable result in an analysis method selected for its noninvasive characteristics. To circumvent this unnatural flattening of the wing, a polymeric foam paint was applied inside the clamp on both sides of the wing, shown in Figure 12.

Figure 12: Side view of a clamped *Manduca Sexta* forewing (a), and the foam-lined clamp of cross-section A-A (b). The four symbols shown in (a) are reference points for future photo-modeling use.

2.3. Verification of Boundary Conditions

The *Manduca Sexta* wing was secured by a foam-coated clamp, sufficiently eliminating artificial changes to its natural shape (camber). During frequency analysis and subsequent finite element modeling, the nature of the applied boundary conditions is of critical importance [14, 26]. While adequately maintaining the hawkmoth wing's undisturbed shape, adding polymer foam causes one to question whether the boundary condition is sufficiently clamped, in the analytical sense. An easy way to answer this question is to conduct a frequency analysis of a well-known problem, for which an analytical solution is available – namely an isotropic, homogeneous, prismatic beam. If the results from the modal analysis of a beam held by the foam-lined clamp match the analytical solution, the clamp may be considered rigid.

2.3.1. Frequency Analysis of a Beam

A beam was constructed by cutting a rectangular strip from a piece of standard copier paper.[8] The beam was placed inside the foam-lined clamp intended for later use, and a frequency analysis was conducted using the Polytec scanning laser scanner. The test was conducted in vacuum conditions (less than 530 Pa., or approximately 4 Torr) to avoid any aeroelastic contributions, as well as verify the ability of the scanning laser to operate through a transparent, acrylic vacuum. The frequency response function (FRF) is plotted below, in Figure 13.

[8] Paper used was Hewlett-Packard Office Recycled Paper, 20lb, 92 brightness.

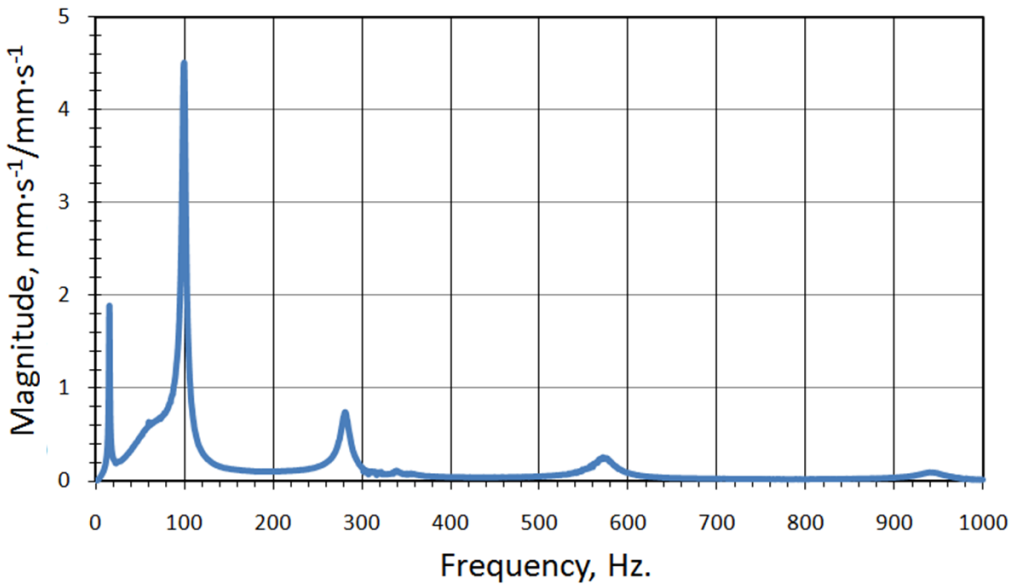

Figure 13: Frequency response function of a paper, fixed-free, cantilevered beam.

The spectral coherence is plotted versus frequency in Figure 14. Spectral coherence satisfies linearity and ergodicity[9], and is described by

$$C_{xy} = \frac{|G_{xy}|^2}{G_{xx}G_{yy}} \tag{1}$$

for two signals, *x(t)* and *y(t)*, where G_{xy} is the cross-spectral density between *x(t)* and *y(t)*, and G_{xx} and G_{xy} are the autospectral densities of *x(t)* and *y(t)*, respectively [5]. Since coherence describes the degree to which the signals *x(t)* and *y(t)* are related in a linear system, it also serves as an indicator of effectively calibrated instrumentation: assuming a structure is linear, its vibration measurement and reference signals should produce a coherence equal to one. As one might expect, the beam used here is a linear structure that produces adequate values of coherence up to approximately 250 Hz.

[9] A signal is ergodic if it contains sufficient data to be considered stochastic. In so doing, its statistical properties may be computed from a single signal that is recorded for a sufficiently long time [5].

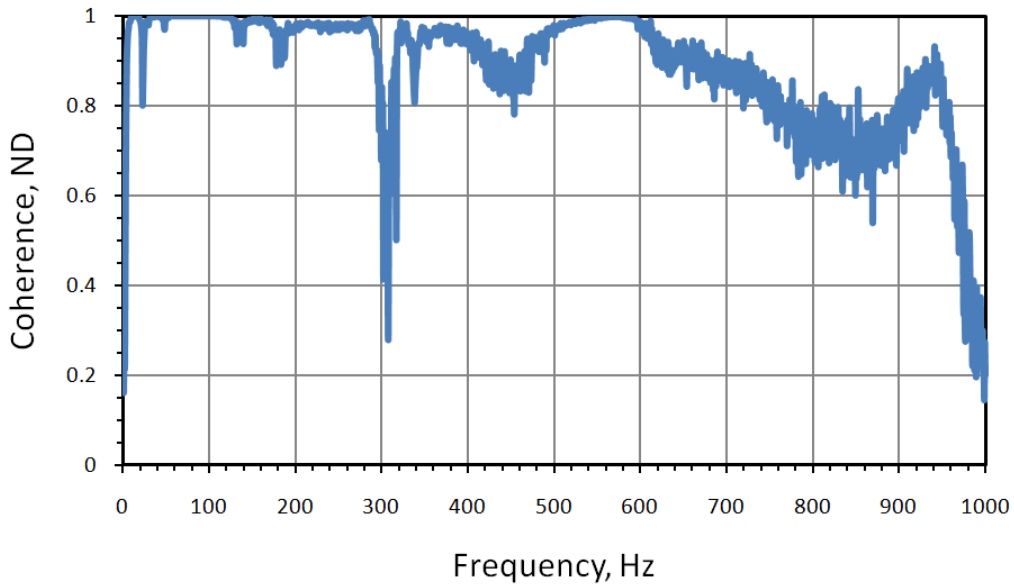

Figure 14: Spectral coherence for the fixed-free beam analysis.

2.3.2. Analytical Fixed-Free Beam Theory

Euler-Bernoulli beam theory has many useful applications for structures that experience negligible shear through the thickness [34]. A vibrating, cantilevered beam of constant Young's modulus, *E*, satisfies this basic requirement and – as will be demonstrated in the paragraphs that follow – has a predictable modal behavior. Most notably, the natural frequency ratios of an Euler-Bernoulli beam are always the same, so long as the beam properties and boundary conditions are unchanged. As a result, the experimentally obtained modes of any prismatic, homogeneous, isotropic beam – for which the material properties are unknown – can be compared to the analytical solution to assess the effectiveness of the real-world boundary condition. Matched analytical and experimental frequency ratios are only possible if the boundary conditions in the experiment satisfy the criteria of the analytical end conditions.

The equation of Euler-Bernoulli beam bending is given in Eq. (2) [34], where *E* is Young's modulus, *I* is the moment of inertia, *F* is the forcing function, *M* is the bending moment,

x is the horizontal coordinate, y is the vertical coordinate, t is time, and L is the length of the beam. A schematic of the beam described by Eq. (2) is shown in Figure 15 [26].

$$-\frac{\partial^2}{\partial x^2}\left[EI(x)\frac{\partial^2 y(x,t)}{\partial x^2}\right] + F(x,t) = M(x)\frac{\partial^2 y(x,t)}{\partial t^2}, \qquad 0 < x < L \tag{2}$$

Since the beam is homogeneous and prismatic, Young's modulus, the moment of inertia, and the beam's mass are constant: *EI(x)=EI*, and *m(x)=m.*

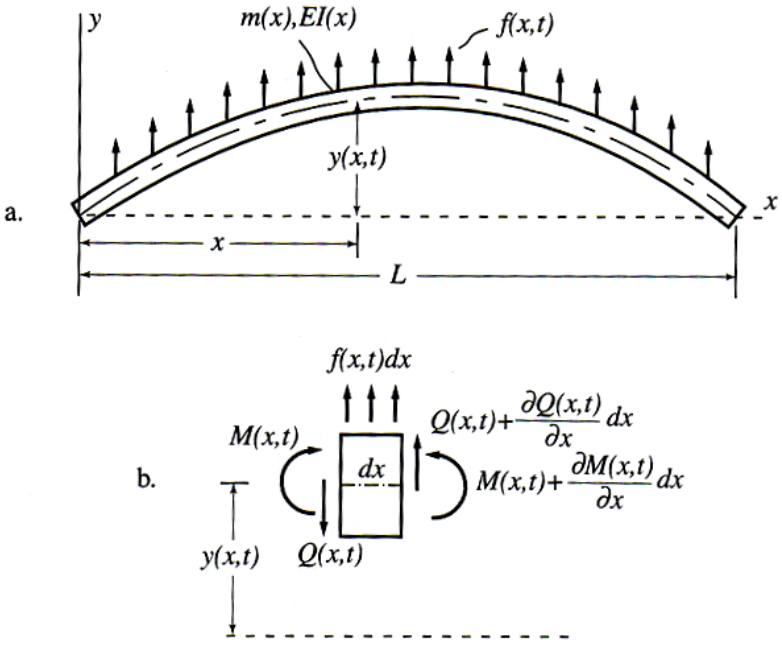

Figure 15: Euler-Bernoulli beam in bending vibration (a), and the free-body diagram for a planar, infinitesimal beam element (b) [26].

Inserting the homogeneous, prismatic assumptions into Eq. (2), and assuming *F(t)* is a harmonic function, yields Eq. (3), where ω is the frequency of oscillation.

$$\frac{d^4Y(x)}{dx^4} - \beta^4 Y(x) = 0, \;\; 0 < x < L; \;\; \beta^4 = \frac{\omega^2 m}{EI} \tag{3}$$

Applying the rigidly clamped boundary condition, the displacement and rotation are both zero at the wall:

$$\begin{cases} Y(x) = 0 \\ \dfrac{\partial Y(x)}{\partial x} = 0 \end{cases}, \qquad x = 0 \tag{4}$$

Likewise, the free end is not subjected to a bending moment or shear stress, thus:

$$\begin{cases} \dfrac{d^2Y(x)}{dx^2} = 0 \\ \dfrac{d^3Y(x)}{dx^3} = 0 \end{cases}, \qquad x = L \tag{5}$$

Finally, invoking the known, general solution of Eq. (3), applying the boundary conditions in Eqs. (4) and (5), and considerable algebraic simplification yields the canonical bending equation for a fixed-free cantilevered beam:

$$cos(\beta L)\, cosh(\beta L) = -1 \tag{6}$$

Meirovitch gives the transcendental equation governing the mode shapes in Ref. [26], and provides the associated frequencies shown in Figure 16. Included in Figure 16 are the frequency values corresponding to the numerical solutions of Eq. (6).

An important facet of Eq. (6) is that for a prismatic, isotropic, homogeneous beam, the ratio of the natural frequencies is always the same (provided the fixed-free boundary conditions are satisfied). In other words, one is not required to know the material properties (*i.e.*, Young's modulus, *E*), measure the beam's length, or calculate the moment of inertia to assess whether a beam is satisfactorily clamped. Simply comparing the ratios of a beam's measured natural frequencies to the ratios given in Figure 16 provides an excellent metric for comparison.

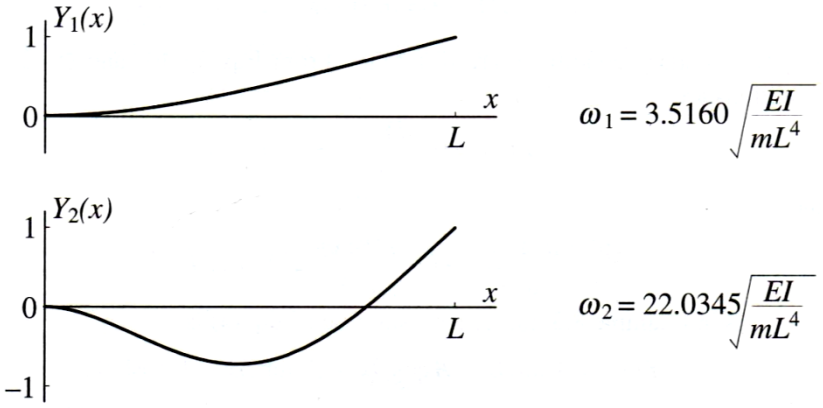

Figure 16: The first two natural frequencies and associated modeshapes for a fixed-free, cantilevered beam [26].

2.3.3. Comparison of Analytical and Experimental Values

The results of the frequency extraction are shown below in Table 2. Table 3 compares the ratios of the paper beam's frequency values to those obtained analytically.

Table 2. Natural frequencies of a fixed-free paper beam.

	Frequency, Hz.
ω_1	15.625
ω_2	100.0

Table 3. Natural frequency ratios of analytical and experimental beams.

	Analytical Solution	**Paper Beam**	**Error**
ω_2/ω_1	6.267	6.40	2.08 %

The values given in Table 3 lead one to the conclusion that the paper beam is made of a homogeneous, isotropic material, and sufficiently satisfies the clamped boundary condition[10]. In so doing, the simple exercise of conducting a frequency analysis of a strip of paper produced important results. One can now say with confidence that the polymer foam painted onto the

[10] Prior to this experiment, it was unknown whether copy paper was isotropic and quasi-homogeneous.

clamp does not adversely affect its performance as a fixed boundary condition, without changing the geometry of a mounted *Manduca Sexta* wing. Moreover, it is evident that the Polytec scanning laser vibrometer is capable of testing through the transparent vacuum used in the setup described above.

2.4. Test Flow and Timeline

With the clamped boundary condition verified, and the successful, optical frequency analysis through acrylic completed, the process of testing a *Manduca Sexta* wing begins. Wing testing is a multi-step, time-consuming process. Unfortunately, liberating the wing exposes the circulatory members at the wing root, causing the wing to dry. As the wing dries, its properties change, nullifying the frequency data and any conclusions drawn from them. As part of his work at AFIT, Norris conducted an investigation of *Manduca Sexta* wing drying effects. During this exercise, he acquired frequency data from multiple liberated wings, and compared their responses to the liberation timeline. He concluded that, under normal, indoor conditions, wings were still "healthy" up to approximately four hours from separation [30].

Operating within this four-hour window, two main studies were conducted. Computed tomography (CT) scans captured the geometry of the wing members. Immediately following the CT imaging, the wing was placed inside the vacuum chamber and analyzed using laser vibrometry.

2.5. Computed Tomography (CT) Imaging

The *Manduca Sexta* forewing is a highly complex structure. There are a multitude of veins and membranes, many of which intersect multiple times. Because of this complexity, a high-fidelity geometric model is required to proceed with any finite element efforts.

Unfortunately, the scale and intricacy of the wing limit the number of devices capable of accurately resolving its components. One apparatus (among others) that is capable of characterizing the geometry of the wing is a computed tomography (CT) "scanner."

Computed tomography scanners rotate an X-Ray imager around a specimen, while taking a series of two-dimensional X-Ray images. These two-dimensional images are then post-processed to build a three-dimensional digital model [22]. The resolution of the model is strongly dependent on the number of images taken, however increasing the number of X-Ray images results in longer scan times. Fortunately, CT is a popular imaging technique in the medical community, thus many of its post-processing features are optimized for examining organic tissue – including moth wings.

2.5.1. Imaging a Manduca Sexta *Wing*

A freshly liberated wing was clamped, as shown in Figure 12, and placed inside the CT scanner at the Materials Directorate of the Air Force Research Laboratory (AFRL/RX). Previous tests by Norris resulted in high-fidelity CT models after only eight minutes [30]. Choosing to err on the side of caution, the *Manduca Sexta* test specimen was scanned for 20 minutes. A plan view of the wing X-Ray is shown below, in Figure 17.

The nature of multi-image composite modeling used in computed tomography allows one to view cross-sectional "slices," through varying tissue densities. This becomes an important feature when attempting to dimension the components in the hawkmoth's wing. Previously, others have assumed the veins were circular in cross-section and measured vein widths (diameters) from above [25]. A quick glance at Figure 17 reveals the difficulty one might have in such a process. Where does the vein stop, and the membrane begin? How large is the inner diameter of each vein (they are, after all, circulatory members)?

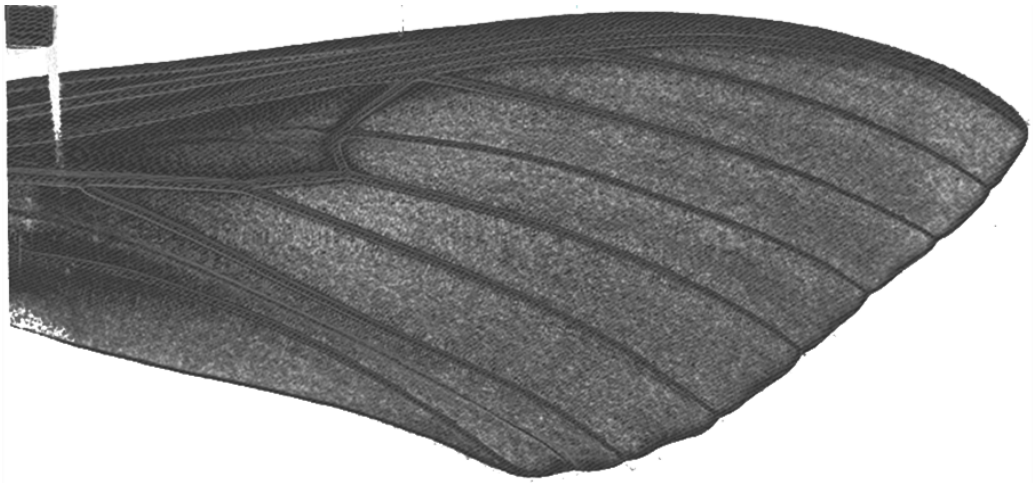

Figure 17: Unprocessed CT image of a female *Manduca Sexta's* right forewing.

Changing the density threshold in the CT model helps answer these questions.

Figure 18 shows the same wing as Figure 17, capturing only high-density tissue. Note that in this image, the inner and outer diameters of the veins are clearly visible upon close inspection. Likewise, the boundary between vein and membrane is much easier to distinguish. Perhaps one of the most obvious artifacts of only resolving the higher-density structures is the noticeable lack of membrane tissue. It appears that the wing skin is of equal density at all points, possibly indicating homogeneity – casting doubt on previous assertions of varying material properties [10,11, 25].

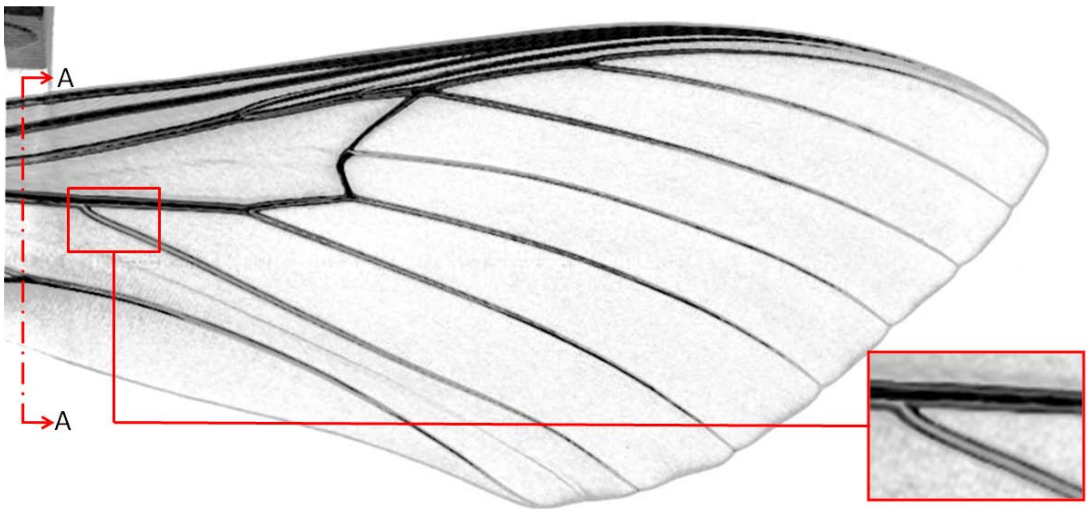

Figure 18: Processed CT image of a female *Manduca Sexta's* right forewing, showing a prominent vein structure.

2.5.2. Wing Geometry

Ultimately, the goal of utilizing CT imaging techniques is capturing the geometry of the wing components. Once completed, these measurements are used to create a finite element model of the wing. Since the CT model is three-dimensional, it is possible to measure the dimensions of the veins and membranes. This is accomplished by measuring cross-sectional "slices" of the wing, from root to tip. Figure 19 shows one such slice, located approximately two millimeters from the wing root[11].

Consisting of a total of five veins, the image illustrates the complexity of the *Manduca Sexta* vein structure – no two veins are alike, though all are approximately circular. Furthermore, the vein closest to the trailing edge (right-most in Figure 19) is dramatically different than the others at this particular cross-section location (Figure 18, A-A). Here, two veins are merging into one, larger vein.

Figure 19: Cross-section A-A (see Figure 18) from a *Manduca Sexta* wing, approximately 2 mm. from the root. The prominent left vein is the leading edge.

With the vein and membrane dimensions clearly visible, measurements were taken at 16 locations, or approximately every six percent of the 46 cm. spanwise length[12]. Cross-sectional slices were concentrated at areas where the vein diameter changed most rapidly (especially near the tip). Although the vein diameters tapered with length, their cross-sectional shapes remained

[11] For readability's sake, grey pixels within 3% of white (denoted in hexadecimal color code as #FFFFFF) were converted to white. The original, unaltered image is located in Appendix B – CT Images.
[12] The exact locations are given in Appendix B – CT Images.

relatively constant between measurement locations. Only at the locations where veins merge or branch were irregularities observed.

All veins were observed to be relatively circular in shape, with one exception. Near the midpoint of the leading edge, several veins merge into one structure; during this transition, the two leading edge veins gradually become closer, until the two circular structures merge into a binocular-shaped double pipe, then finally into a box-beam. At approximately 60% of the spanwise length, the box-beam-shaped leading-edge vein resumes its circular shape. Unlike the veins, however, the membrane remained a nearly constant 0.12 millimeter thickness, deviating only ±0.02 millimeters at the extrema.

2.6. Modal Identification of a Manduca Sexta *Forewing in Vacuum*

A *Manduca Sexta* wing was analyzed using a scanning laser vibrometer to determine its frequency content. As described previously, the frequency data were collected *in vacuo*, to eliminate any potential aeroelastic effects. The automatically-computed frequency response function for the *Manduca Sexta* forewing is shown below, in Figure 20. Table 4 gives the first three natural frequencies observed in this experiment.

Table 4. Natural frequencies of a *Manduca Sexta* forewing in vacuum.

	Frequency, Hz
ω_1	86
ω_2	106
ω_3	155

Notice that the coherence decreases as the frequency approaches the 400 Hz cutoff. Since this analysis is primarily concerned with only the first three modes, the reduction in coherence values at high-frequencies do not negatively impact the fidelity of the low-frequency

(less than 250 Hz) measurements. These high coherence values seem to indicate that the wing is a linear structure, since any structural response is strongly correlated to its excitation.

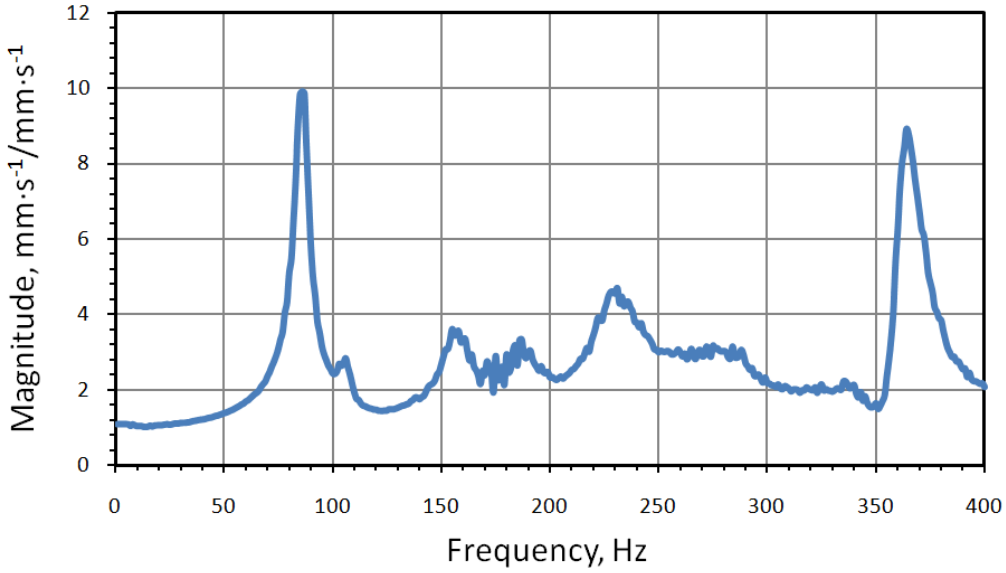

Figure 20: Frequency response function (magnitude) for a *Manduca Sexta* wing in vacuum.

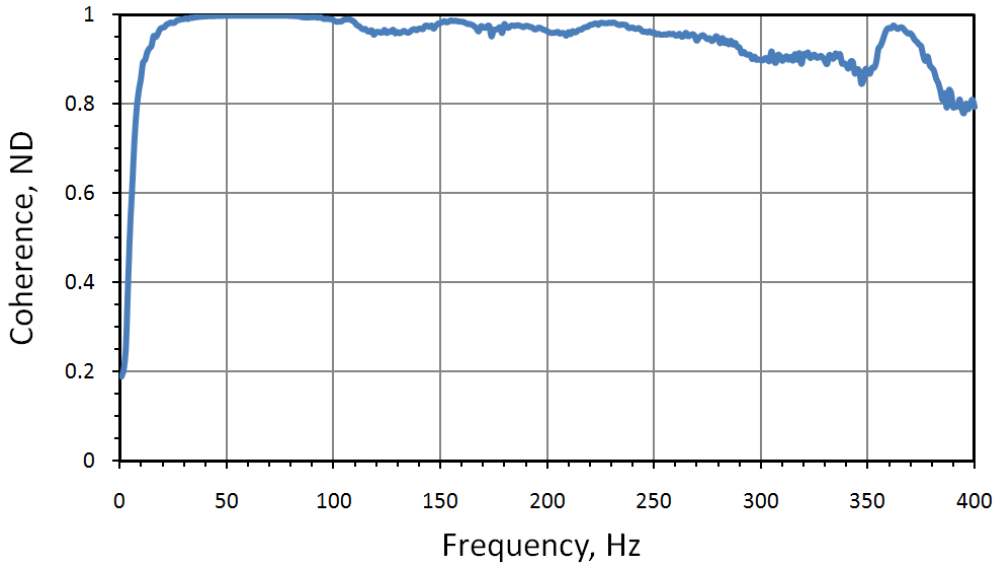

Figure 21: Spectral coherence for the *Manduca Sexta* wing analysis.

The modeshapes – how the structure responds to a natural frequency input – are important parameters in describing the wing[13]. Due to the orthogonality of the eigenvalues and eigenvectors, each of the natural frequencies (modes) listed in Table 4 has a unique, associated modeshape [26]. The modeshapes corresponding to the first three natural frequencies are shown below. For ease of understanding, all mode shapes are presented first in an isometric view with the trailing edge in front and the leading edge in the rear. Each modeshape is also accompanied by a tip view, looking inward towards the wing root.

The first natural frequency occurs at 86 Hz, and exhibits a modeshape analogous to the first bending mode of a cantilevered beam. Similar to the beam shown by Meirovich, the first modeshape of the *Manduca Sexta* forewing has a maximum displacement at the tip, and flaps in only one plane of motion.

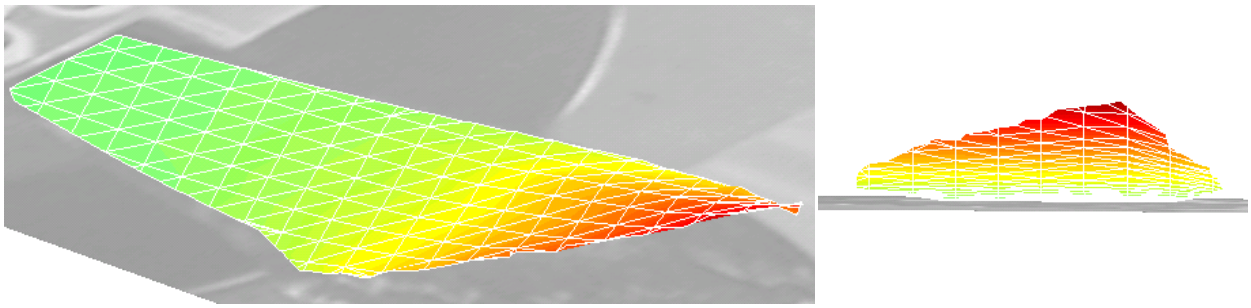

(a) (b)

Figure 22: First modeshape (86 Hz) of a *Manduca Sexta* wing, shown from an isometric view (a) and a tip view (b).

The second mode of the *Manduca Sexta* forewing occurs at 106 Hz with a modeshape similar to the first torsional mode of a plate fixed at one end. The maximum displacement is at the wing tip, with the leading and trailing edges deflecting asynchronously. Also akin to the second mode of a plate fixed at one end (first torsion), the second modeshape of the hawkmoth wing rotates about a central axis, approximately located at the half-chord line.

[13] It should be noted that the term "modeshape" is used here to denote an operational deflection shape that is strongly dominated by the wing response at resonance.

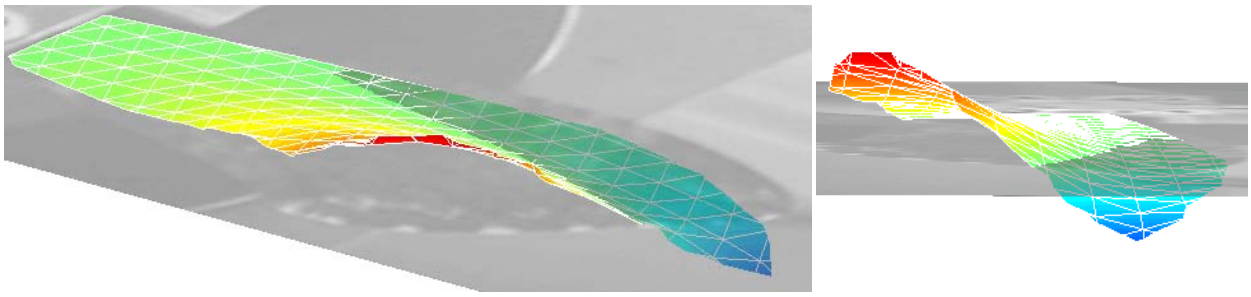

(a) (b)

Figure 23: Second modeshape (106 Hz) of a *Manduca Sexta* wing, shown from an isometric view (a) and a tip view (b).

The third mode occurs at 155 Hz. In many ways, the behavior of the wing at this frequency is similar to that of its second mode, with an important exception. Instead of asynchronous flapping about the half-chord line, this mode displays synchronous (in-phase) flapping of the leading and trailing edges at the tip. As this occurs, the half-chord line exhibits bending similar to the first-beam bending mode, but out of phase with the flapping in the leading and trailing edges. The combination of the leading / trailing tip flapping and half-chord bending creates an overall deflection shape resembling a saddle. This "saddle mode" is shown below, in Figure 24. A similar saddle mode is seen in the fifth modeshape of a rectangular plate fixed at one end.

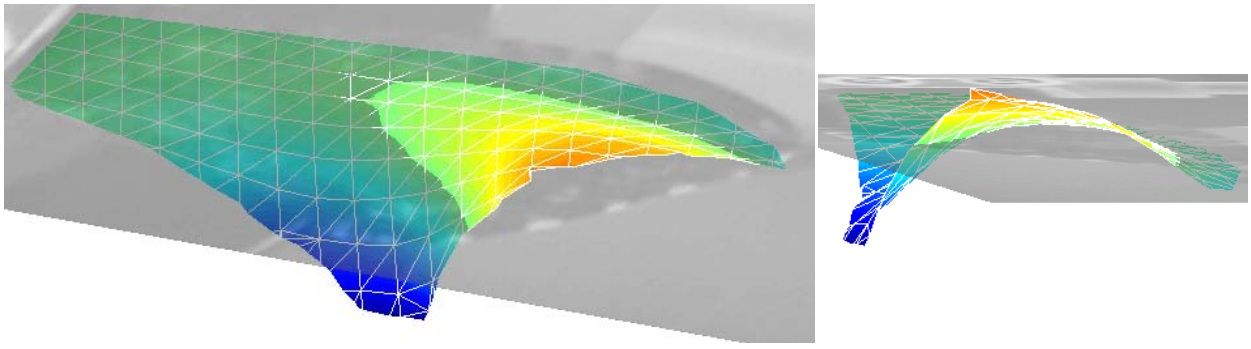

(a) (b)

Figure 24: Third modeshape (155 Hz) of a *Manduca Sexta* wing, shown from an isometric view (a) and a tip view (b).

Examining the frequency response function reveals that the magnitudes of high-frequency modes are small, with the exception of 368 Hz mode. Since the *Manduca Sexta* beats its wings near 25 Hz. [40], it is unlikely that the higher-frequency modes have more than miniscule effects on the operational deflection shape of the wing. The fourth and higher mode shapes are shown in Appendix C – Higher Order Modes, but are omitted from further analysis. Every continuous structure has an infinite number of natural frequencies, forcing one to define an upper bound during analysis [26]. Considering only the first three modes provides an adequate basis for future model verification, as well as limits the scope of the investigation.

2.7. Modal Identification of a Manduca Sexta *Forewing in Air*

The *Manduca Sexta* frequency identification experiment was repeated using the same setup and methods, only at room temperature and pressure. To eliminate drying effects, a fresh wing was used. The modeshapes of the wing were the same as those given above; however the frequencies at which they occurred were different. Evidently, the fluid interaction with the wing serves as a damping mechanism, reducing the frequency content by as much as 26% at the lower modes. Likewise, the ratios of the natural frequencies changed, and seemed to scale with increasing frequency.

This finding provides insight into the previously mentioned – and much debated – aeroelastic question. Furthermore, future studies regarding the nature of the damping involved will likely prove beneficial, since the *Manduca Sexta* does not operate in vacuum conditions in nature. Table 5 lists the frequencies associated with each mode, and Table 6 compares the frequency ratios.

Table 5. Natural frequencies of a *Manduca Sexta* wing in air and vacuum.

	Air, Hz	**Vacuum, Hz**	**Change**
ω_1	58.75	80	26.56%
ω_2	75	98	23.47%
ω_3	95	118	19.49%

Table 6. Comparison of frequency ratios of *Manduca Sexta* and wing in air and vacuum.

	Air	**Vacuum**	**Change**
ω_2/ω_1	1.28	1.23	4.04%
ω_3/ω_1	1.62	1.80	8.78%

2.8. Paper Wing Tests

In light of the camber observed during the computed tomography (CT) scans, one wonders whether camber is an important structural characteristic in the hawkmoth wing. Certainly, it is a widely accepted fact that camber increases low-Reynolds number aerodynamic efficiency [33] – a valuable attribute for small wings. However, to date, flat, rigid wing designs with homogeneous material account for a large number of MAV research [29]. These wings provide computational simplicity, and are cost effective.

Flat, rigid flapping wings are often relevant in the scientific endeavor. In fact, several studies have found rigid, plate-like wings on the *Calliphora* (blowfly), *Tibicen canicularis* (cicada), and others [25]. Since the *Manduca Sexta* falls inside the DARPA size, weight, and payload requirements, it is beneficial to know whether a flat, homogeneous wing reasonably approximates the actual forewing. While one could construct a finite element model, a simple process is to make a paper replica, conduct a frequency analysis, and compare the results to *Manduca Sexta* forewing data.

Previous tests showed that copier paper is a homogeneous material, suitable for testing simple, semi-two-dimensional cases. To explore the extent to which the veins and membranes are quasi-isotropic, and the degree to which camber effects the hawkmoth wing modeshapes, a paper wing of the same planform was constructed. To simplify the process, a *Manduca Sexta* wing was placed inside a photocopier; the copy was cut out in the shape of the printed wing and placed inside the vacuum chamber for testing[14]. Figure 25 shows the wing used, and the results of this test are shown in Figure 26 and Table 7.

Figure 25: Paper wing used in frequency experiments.

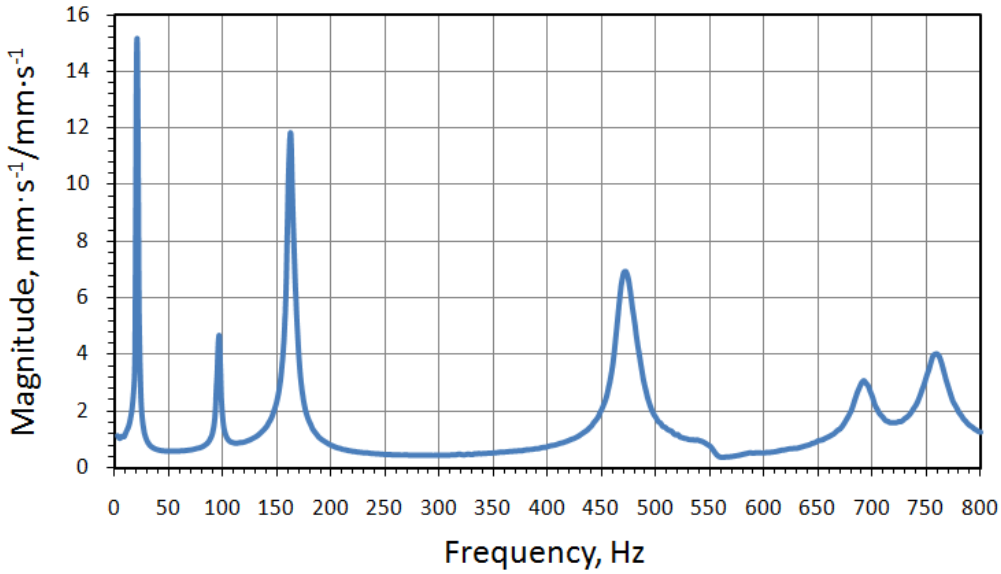

Figure 26: Frequency response function of the paper wing.

[14] A tacit assumption here is that the ink on the copier paper does not significantly affect the "wing" response.

Table 7. Natural frequencies of a paper wing in vacuum.

	Frequency, Hz
ω_1	20
ω_2	96
ω_3	162
ω_4	472
ω_5	692

Table 8 compares the ratios of the natural frequencies obtained during the paper wing tests to those of the *Manduca Sexta* in vacuum. Clearly, the two are unrelated in their frequency content, and for reasons other than their difference in materials and mass. While one would expect their natural frequencies to be different, the hawkmoth wing and paper wing would have similar frequency ratios if material properties and mass were their only differences. It is likely that the *Manduca Sexta* wing stiffening due to the presence of circulatory members is affecting its frequency content.

Table 8. Comparison of frequency ratios of *Manduca Sexta* and paper wings in vacuum.

	***Manduca Sexta* Wing**	**Paper Wing**
ω_2/ω_1	1.23	4.8
ω_3/ω_1	1.80	8.1
ω_4/ω_1	2.17	23.6
ω_5/ω_1	2.69	34.6

Examining the modeshapes of the paper wing reveals a different picture. In fact, the modeshapes are similar to the *Manduca Sexta*, even though their frequency content is radically different – suggesting wing geometry is a dominant factor in modeshape appearance. Although at different frequencies and a different frequency ratio, the first two modeshapes of the paper wing are nearly identical to those of the hawkmoth. The first mode is a flapping mode, similar to a homogeneous fixed-free beam's first bending mode (see Figure 27). The second modeshape is

similar to the second mode of a flat, rectangular plate fixed at one end: exhibiting torsion about the central axis, from root to tip (see Figure 28).

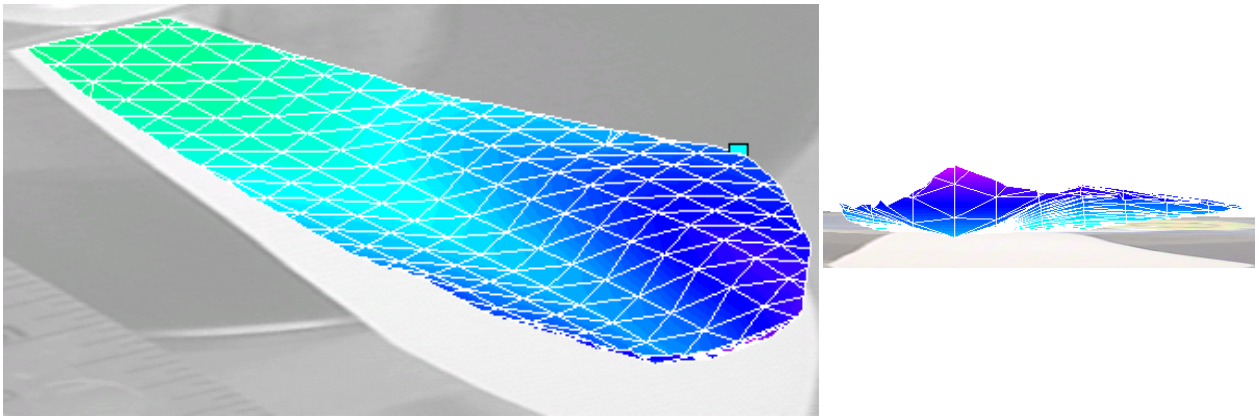

(a) (b)

Figure 27: First modeshape (20 Hz) of a paper *Manduca Sexta* wing, shown from an isometric view (a) and a tip view (b).

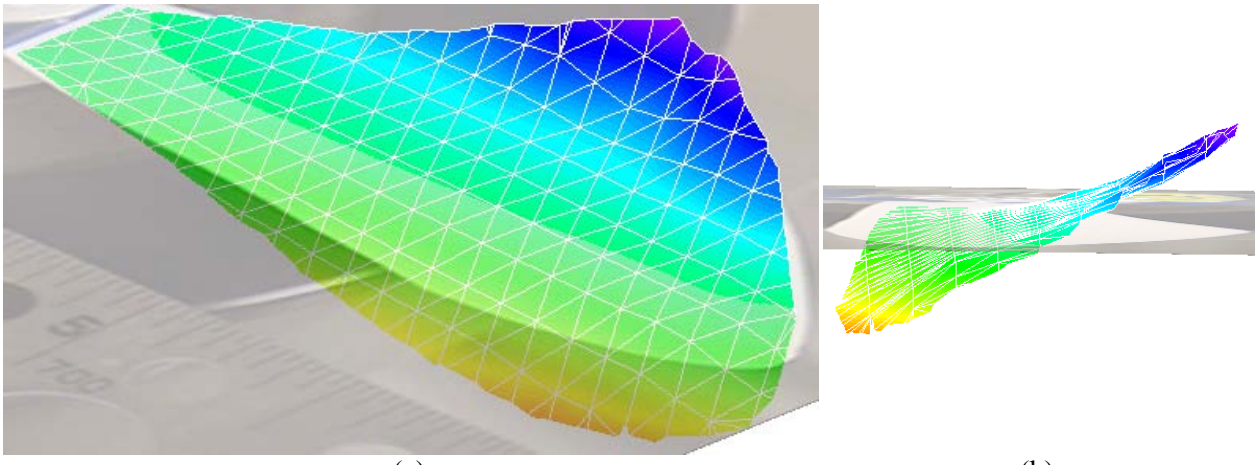

(a) (b)

Figure 28: Second modeshape (96 Hz) of a paper *Manduca Sexta* wing, shown from an isometric view (a) and a tip view (b).

The third modeshape, shown in Figure 29, appears at 162 Hz. Here, the wing appears to approximate the second bending mode of a fixed-free beam at the half-chord line. The leading and trailing edges appear to lag the phase of the half-chord line, but mimic its behavior. The

third mode shape is unique to a paper wing, suggesting the *Manduca Sexta* wing has more chordwise stiffness than its paper counterpart.

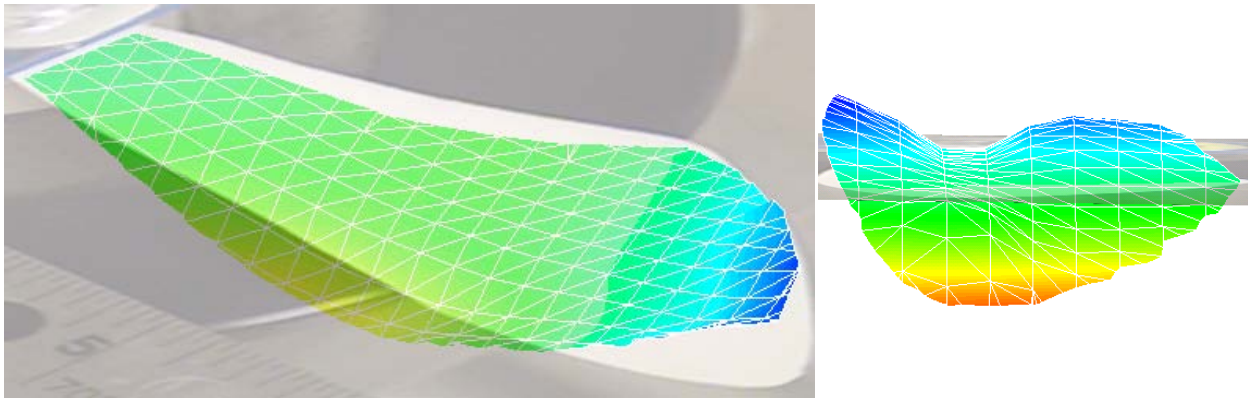

(a) (b)

Figure 29: Third mode shape (162 Hz) of a paper *Manduca Sexta* wing, shown from an isometric view (a) and a tip view (b).

As a counter-argument, one may suggest that the third mode shape in the paper wing might be present in the *Manduca Sexta* wing, but out of order, *i.e.*, it appears at higher frequencies. This is unlikely, however, since the higher frequency modes seem to excite the entire structure less with increasing frequency. The high-order mode shapes found Appendix C – Higher Order Modes paint a clear picture: high-frequency content is seen most at the wing tip and trailing edge, near the half-span.

The fourth paper wing mode appears at 472 Hz, and approximates the saddle mode (third mode) of the hawkmoth wing, but with added tip-deflection. The leading and trailing edges flap synchronously, and out of phase with the vertical motion of the half-chord line. An important distinction between the *Manduca Sexta* wing and the paper model is the tip behavior. A comparison of Figure 24 (b) and Figure 30 (b) highlights the increased tip motion in the paper specimen, relative to the rest of the wing. The third mode shape of the *Manduca Sexta* wing showed asynchronous deflections in the trailing edge and the tip of the wing, with only slight

leading edge movement. In contrast, the fourth modeshape of the paper wing shows prominent tip deflection in phase with the central portion of the wing. While this characterization is purely qualitative in nature, it provides useful insight into what features are important in the modal behavior of a *Manduca Sexta* wing.

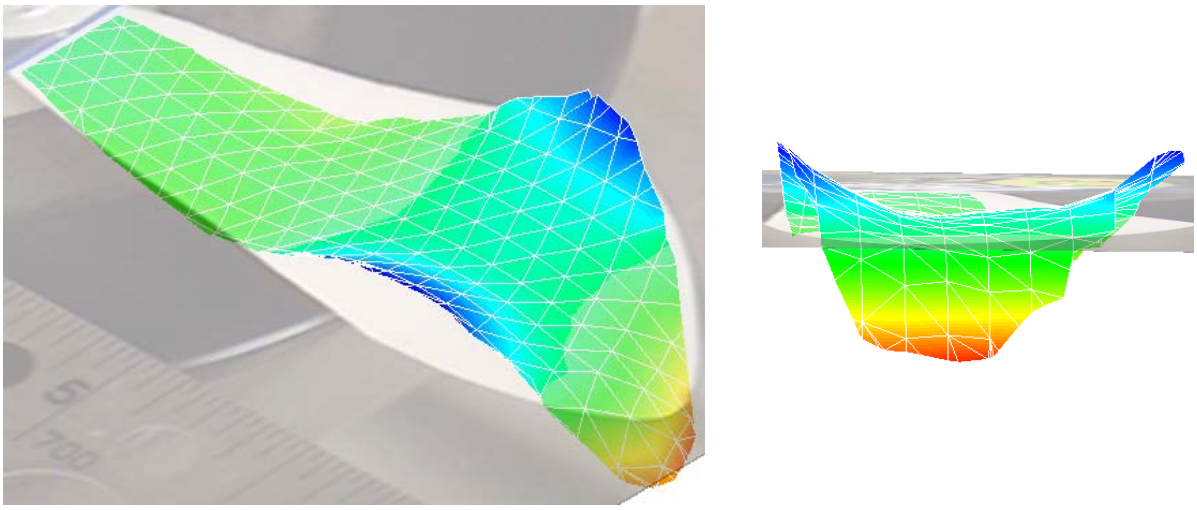

(a) (b)

Figure 30: Fourth modeshape (472 Hz) of a paper *Manduca Sexta* wing, shown from an isometric view (a) and a tip view (b).

Combined with the flexibility of the leading edge, the vertical deflection of the wing tip in Figure 30 appears to be much more dominant than that observed in the *Manduca Sexta* wing; this flexibility in the paper specimen likely results from the lack of veins or cambering stiffness. Tests were conducted *in vacuo*, leading one to postulate that the presence of veins increases kinematic tip-stiffness.

The fifth mode is given in Appendix C – Higher Order Modes. As described above, the higher-order modes, while useful for model validation play a miniscule role in the behavior of the *Manduca Sexta* wings. This is even more the case for the paper specimen, since the fifth mode occurs at 692 Hz – 28 times the beat frequency of the *Manduca Sexta* wing. Inspecting the

frequency response function of Figure 26 reveals that the first three modes are dominant, with a significant loss in power in the fourth and higher modes.

Comparing the actual *Manduca Sexta* wing and the flat, paper specimen gives insight regarding the importance of the wing components. The hawkmoth wing appears to be dominated by plate-like modeshapes – as one might expect given its dimensions. By contrast, the paper wing seems to exhibit a composite beam / plate behavior, intermittently resembling either structure. The absence of the second beam bending mode from the *Manduca Sexta* wing and the lack of tip motion in the saddle mode suggests the veins have structural importance – that is, they are not only useful as circulatory members. At this point, it is evident that mimicking *Manduca Sexta* flight will require stiffening members, though it is unclear to what extent camber plays in the wing response.

III. Numerical Methods

The primary focus during the numerical phase of study is identifying features of the finite element method that will prove useful in eventually modeling the *Manduca Sexta* forewing. The computed tomography (CT) images provided the geometric basis for modeling, and the laser vibrometry provided the wing modes and modeshapes. Together, these methods provide a vast amount of information about the hawkmoth wing structure. Indeed, reverse engineering a *Manduca Sexta* wing is no trivial task, and requires one to make simplifications in the modeling process. This chapter explores what simplifications are permissible, what attributes must closely mimic the *Manduca Sexta*, and how one might proceed with the modeling process.

Such topics as element selection, geometric simplification, camber effects, mesh convergence, and modal effects of vein diameter are discussed in the sections that follow. All modeling is carried out in Abaqus Standard, Version 6.8. From these analyses it is clear that the veins should be modeled using quadratic beams, and the wing membrane should be modeled using linear, general-purpose shell elements. A convergence study of the final model is presented in Chapter IV.

This chapter begins with a discussion of model construction using the data collected from the CT scans. A discussion of element selection follows, with convergence studies for each case. Following the results of the studies involving the membrane elements, a discussion of membrane element theory explains the formulation of plane-stress elements, and their shortcomings in modeling *Manduca Sexta* wings. Abaqus is validated through a comparison of experimental and finite element results involving a paper wing. Finally, studies are conducted examining the effects of wing camber and vein dimensions on natural frequency in the *Manduca Sexta* wing.

3.1. Model Construction

The computed tomography (CT) scans provided an excellent three-dimensional digital model of the moth wing. Since this model is built directly from X-Ray images of the wing, it has only one geometric simplification. The wing surfaces are exported to stereolithography (STL) CAD files, with continuous surfaces approximated by several triangular facets. These STL files can be imported into various CAD programs and then into Abaqus for analysis. There are several potential benefits in using this method for finite element analysis: the STL model approximates the actual structure well, no geometry measurements are necessary, and model construction – one of the most time-consuming tasks – is already complete.

Unfortunately, an analysis using the STL model of the *Manduca Sexta* forewing has one major downfall: meshing. Figure 31 shows a portion of the hawkmoth wing root. The second and third veins (from the leading edge) are shown, oriented with the leading edge to the right[15]. Inspecting only a small portion of the wing reveals it is unlikely that even a highly refined mesh, consisting only of tetrahedral elements, would successfully discretize this structure. Moreover, if such a mesh were successful, it would hardly be desirable due to the excess bending stiffness associated with tetrahedrons – especially in thin structures[16] [1, 2, 44].

As an alternative to attempting a direct mesh of the STL model, one could attempt a geometry "clean-up" process. A reasonable geometric simplification could be achieved with smooth surfaces instead of triangular facets. Likewise, one could enforce a discrete separation of veins and membrane instead of the nebulous transitions shown in Figure 31. Still, this approach is undesirable due to the induced stiffness of a tetrahedral mesh, and the time (possibly weeks)

[15] A planform view of this image is shown in Appendix B – CT Images.

[16] This statement is regarding volumetric and shear locking in linear tetrahedral elements. Quadratic tetrahedrons offer more accuracy, but the overall complexity would force the model to have large quantities (possibly millions) of unknown degrees of freedom.

required to achieve an adequately simple geometric representation. Conversely, the thinness of the wing membrane and tapering of the generally circular veins suggests it is possible to achieve a reasonably accurate solution using shell and beam elements, respectively. Thus, the selected approach was to create a CAD model that reasonably approximates the *Manduca Sexta* forewing using measurements taken from the CT images.

Figure 31: Stereolithography (STL) image of a *Manduca Sexta* wing root. Shown are the second and third veins from the leading edge (leading edge is to the image right).

3.2. Element Selection

The *Manduca Sexta* wing is divided into two major components: vein and membrane. The veins are generally oriented in the spanwise direction, and taper from root to tip. The membrane has no obvious orientation (from CT scans), and has a generally constant thickness of approximately 0.12 millimeters. The relative thinness of the wing membrane[17] requires one to consider what element type is appropriate for modeling. The veins, however, can be modeled as

[17] The term "membrane" is used here in the tissue sense of the term, not as an element type.

wire beams, with appropriately assigned cross-sections. Still, numerical studies must be conducted to determine to what extent the wing frequencies are affected by the vein taper. In other words, a total of 16 cross-sectional measurements were taken from the CT images; how many of these cross-sectional assignments are required to adequately model the behavior of the veins as wire beams? The studies that follow answer these questions.

3.2.1. Modeling with Membrane Elements

Physical handling of the *Manduca Sexta* wing reveals a structure that is highly dominated by vein stiffness, with the membrane fulfilling a displacement continuity role. It appears that the "membrane" – *i.e.*, the tissue between the veins – may be structurally characterized by membrane elements, in the finite element sense of the term. By convention, membrane elements are sheets that exist in plane-stress [1]. Any stresses are carried parallel to the midsection of the element, with all others assumed zero. Membrane elements have no bending or transverse shear stiffness. As a result, any strains normal to the element or in the transverse direction (ε_{3i}) the result of Poisson effects in the constitutive relations, when the element lies in the plane described by ε_{11} and ε_{22} [44]. A schematic of a four-noded membrane element and its positive normal vector, *n*, are shown below, in Figure 32.

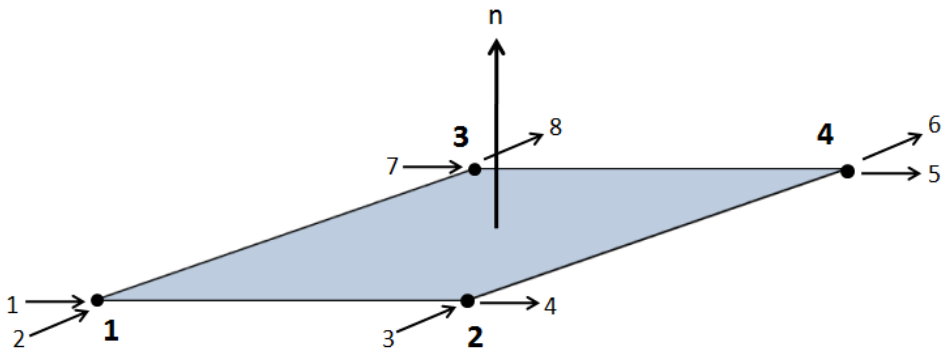

Figure 32: A four-noded linear membrane (plane-stress) element.

Before attempting to create a model that represents the entirety of the hawkmoth wing, a model was constructed to examine the behavior of the vein-membrane interaction. Three wire beams of circular cross-section are connected by two planar sections of membrane elements, as shown in Figure 33. The three beams and two membrane sections were tied together, forcing their displacements to be the same at the node locations, and were of dimensions representative of the *Manduca Sexta* wing. Two test cases were run: the first with linear membrane elements, and the second with quadratic elements. For simplicity, aluminum was selected as the material in both cases.

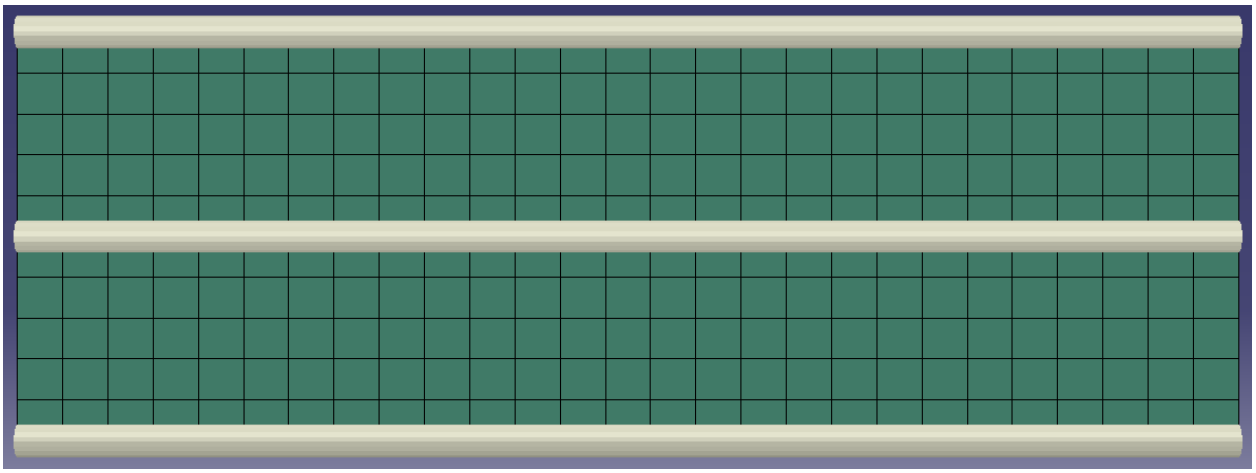

Figure 33: Finite element model of three wire beams (top, middle, bottom) connected by two membrane sections.

The first frequency analysis was conducted using two-noded linear beams (B31) and four-noded quadrilateral membrane elements (M3D4). Mesh densities between 304 elements (348 nodes) and 750,000 elements (756,504 nodes) were considered for convergence. The model is planar with only one element through the thickness, thus a full-integration method was used to avoid any idiosyncrasies associated with constant strain, reduced integration formulations [7]. The first modeshape is shown below in Figure 34. Most notably, the central beam (analogous to a vein) is in motion, affecting only its adjacent membranes. There is transference

of motion among the membrane elements in the out-of-plane direction; in its present state, this beam-membrane configuration is incapable of describing the eigenvectors seen experimentally in the *Manduca Sexta* wing.

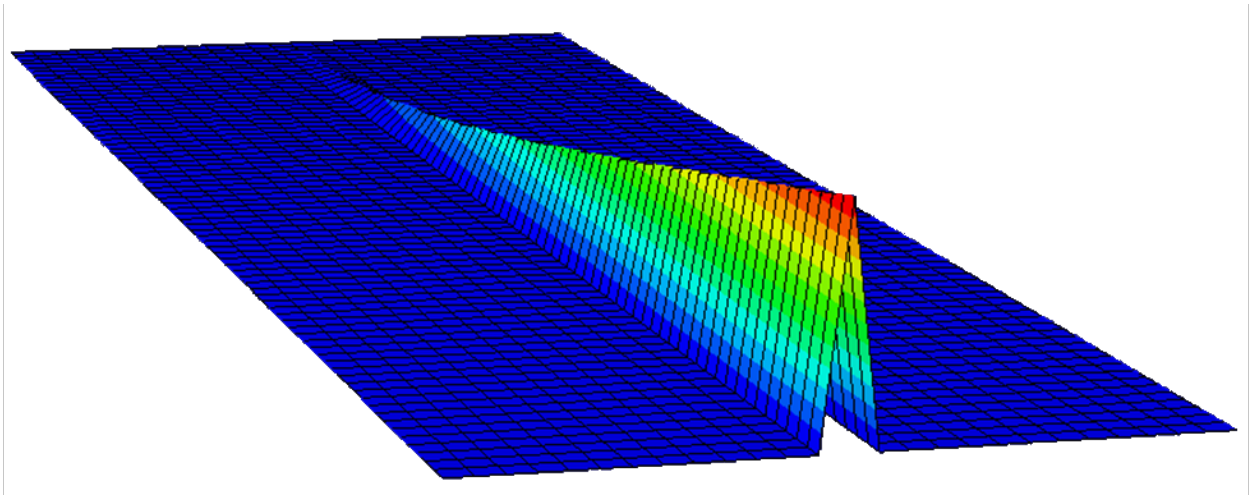

Figure 34: Finite element results of three quadratic wire beams connected by two linear membrane sections. Color bands denote displacement.

The large vertical displacement of the beam relative to the undeformed state suggests a more refined mesh may alleviate the discontinuity of slope near the central beam. To this end, a convergence study was conducted to determine how many linear elements are required to sufficiently conduct an accurate frequency analysis. The results of this convergence study are shown below, in Figure 35. Although the frequency values vary with mesh size, the modeshapes remain similar, even with as many as 750,000 membrane elements with 756,504 nodes (by comparison, Figure 34 shows 1,950 elements). In fact, the only change in the eigenvalue structure is the thickness of the membrane "peak" near the beam. As the membrane element size approaches an infinitesimal value, the width of the peak approaches the thickness of the beam.

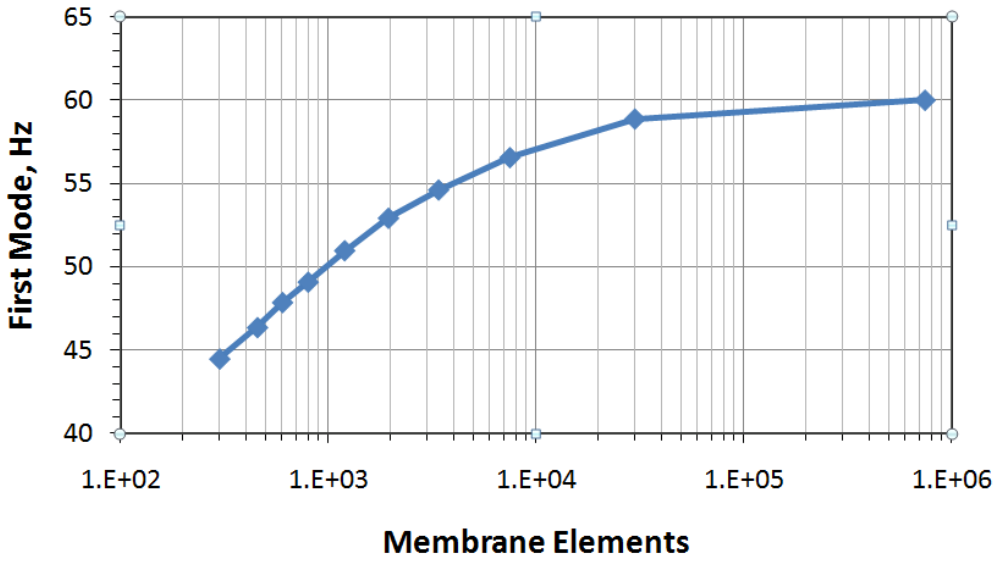

Figure 35: Convergence study of a finite element model with three quadratic wire beams connected by two linear membrane sections.

It is apparent from examining the results of the above convergence study that linear membrane elements are insufficient for modeling the *Manduca Sexta* wing. Even in a simple case involving three wire beams and two membrane sections, nearly one million elements were required before a behavior resembling convergence was achieved. Furthermore, unlike the behavior observed experimentally, the linear membrane elements do not allow continuity of displacement (or slope) normal to the element plane. Either a quadratic membrane, or a new element entirely, is required.

A second analysis was conducted using the model shown in Figure 33, this time with eight-noded quadratic, quadrilateral membrane (M3D8) elements. The M3D8 element resembles the linear membrane of Figure 32, with added midside nodes; like the linear membrane element, each node has only the two in-plane degrees of freedom. The first modeshape is shown below, in Figure 36. In this case, the results are somewhat similar to those obtained using linear membrane elements, with two distinctions. First, the added midside nodes in the quadratic element produce intra-element vibrations at the natural frequencies in the vertical direction.

Second, in keeping with their second-order shape functions, the quadratic membrane elements are able to affect the displacement of adjacent membranes; this advantage, however, should not be overstated since the model results show any displacement influence is negligible approximately three elements from the central beam.

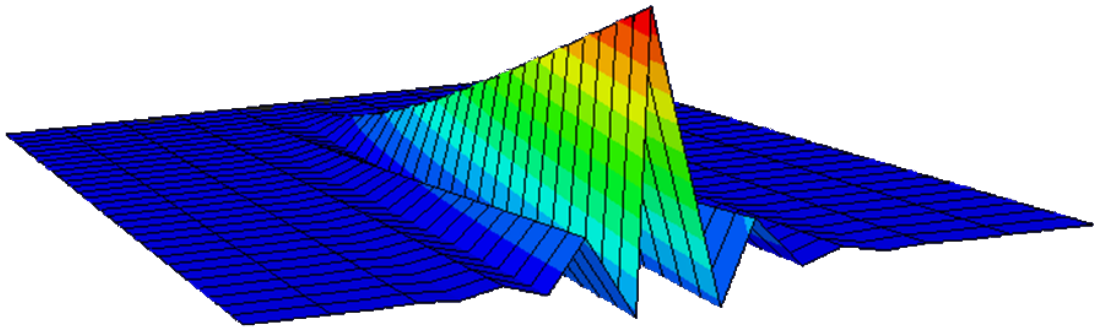

Figure 36: Finite element results of three quadratic, wire beams connected by two quadratic membrane sections. Color bands denote displacement.

Figure 37 shows the same model as in Figure 36, but with a more discretized mesh. The effects of mesh refinement using quadratic membrane elements are similar to those of the linear elements. Decreased element size, corresponding to an increase in the overall number of elements, results in an exaggerated modeshape that resembles a Dirac delta function at the middle beam. Again, the effects of the beam displacement are unfelt at a distance of only three membrane elements from the beam.

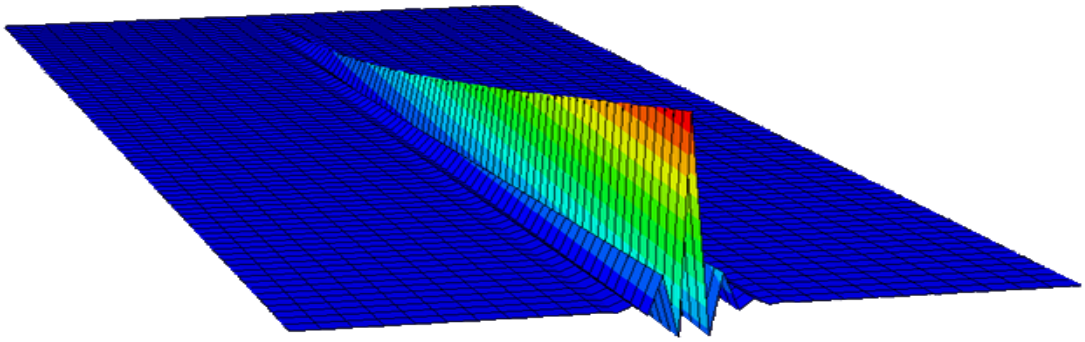

Figure 37: Finite element results of three quadratic, wire beams connected by two quadratic membrane sections, with a refined mesh. Color bands denote displacement.

Repeating the approach used with the linear membrane elements, a convergence study was conducted to determine whether the mesh produces a stable result. As before, if the model results are independent of mesh size, one may deduce that increasing the number of elements will have little (or no) effect on the behavior of the structure. Thus, if the problems of displacement only near the central beam persist, even though the frequency analysis is stable, it becomes evident that membrane elements are ill-suited for modeling the *Manduca Sexta* wing. The results of the convergence study involving quadratic membranes are shown below, in Figure 38.

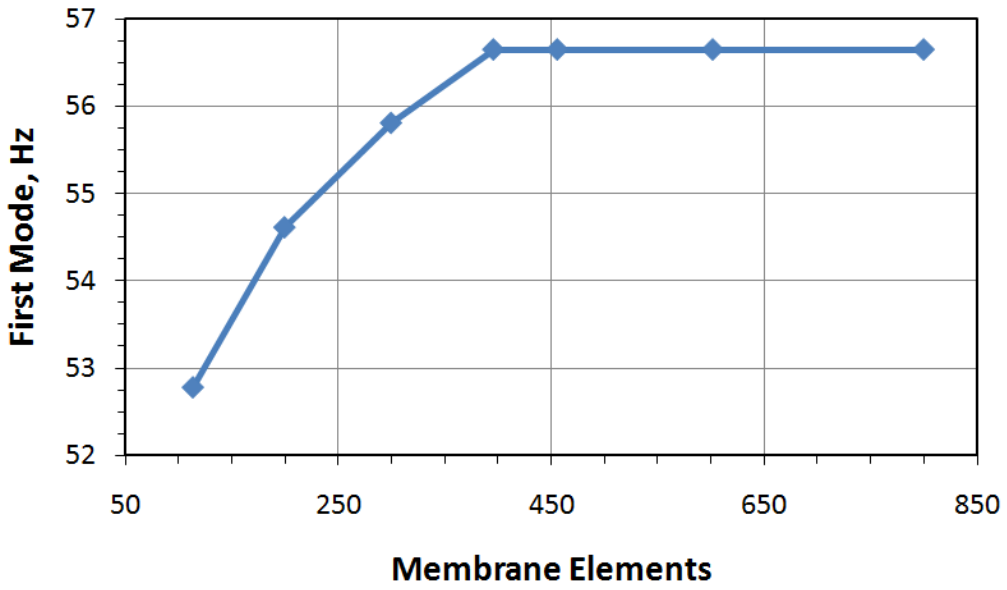

Figure 38: Convergence study of a finite element model with three quadratic wire beams connected by two quadratic membrane sections.

Highlighting the computational usefulness of quadratic formulations, this model achieved convergence after only 403 elements (1109 nodes), at approximately 3 Hertz below the linear membrane solution. Despite the usefulness of this well-known result, the behavior of the converged model is unchanged from that of Figure 37. Membrane elements – linear or quadratic

– are not able to describe the motion observed in *Manduca Sexta* wings, but why? To answer this question, one must revisit the first principals of membrane element formulation.

3.2.2. Membrane Element Formulation

Membrane elements are plane-stress formulations, that is, the only non-zero stresses lie in-plane with the midsection of the element. Figure 39 shows a membrane element described by the $x_{11} - x_{22}$ plane, in which all stresses in the $3i$-direction are *assumed* to be zero ($i = 1, 2\ 3$). There is a vast difference between a structure *in* plane-stress and a structure *assumed* to be in plane-stress, though the difference wording is minor. Structures in plane-stress are sufficiently thin, such that only stress tractions normal to the midplane are allowed to be nonzero. Computationally, elements assumed to be in plane stress leave components in the $3i$-positions of stress matrix uncalculated and filled with zeros [44]. In other words, any out-of-plane stress present in a membrane element will not be calculated; if stress values are included as initial conditions, they will be overwritten by zeros.

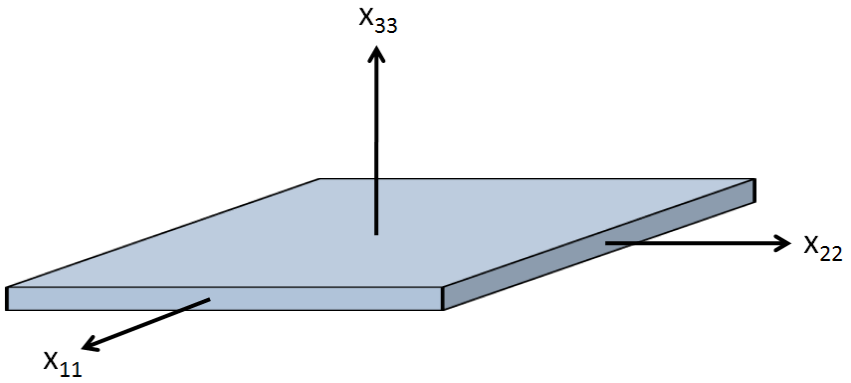

Figure 39: Membrane element described by the x_{11}–x_{22} plane.

To illustrate this point, a model is shown below in Figure 40, consisting of a rectangular part with a vertical load in the center. The part is bounded on all four sides by an encastré condition, and meshed with quadratic membrane elements. For convenience, aluminum material

properties are used, and the load in the center is a concentrated point-load of 1,000 lbf (4.448 kN). The results of this analysis are given below, in Figure 41.

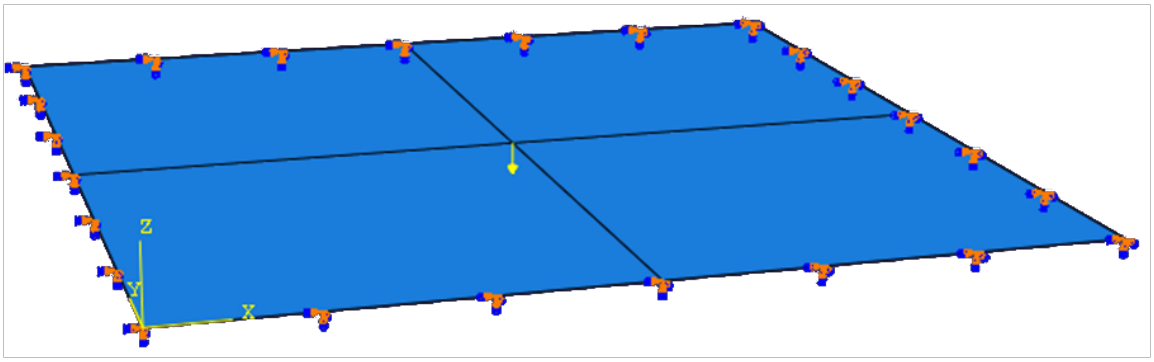

Figure 40: Rectangular structure comprised of membrane elements, with a central load.

The results might astonish one unfamiliar with the underlying mathematical basis of membrane elements: a vertical load of 1,000 lbf results in zero von Mises stress at all points. Clearly these results are erroneous, but only because the initial conditions violate the plane-stress scenario. The analysis results in a zero stress, zero displacement condition, because the solver set all loading terms normal to the midsection equal to zero – eliminating the 1,000 lbf load.

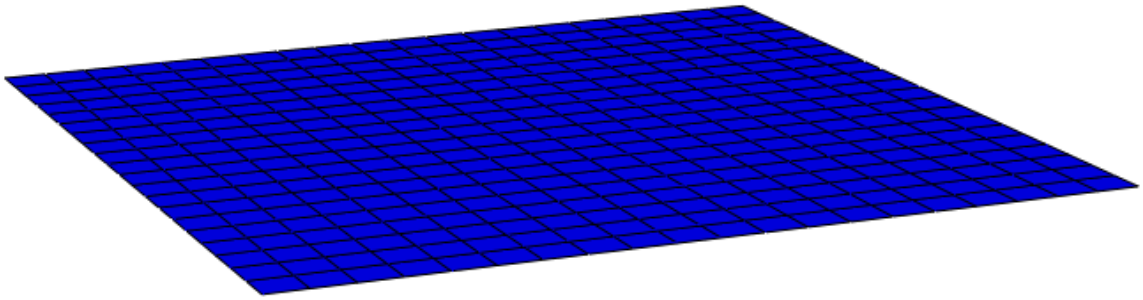

Figure 41: Results of a vertical point loads using only membrane elements. Blue denotes zero von Mises stress.

Returning to the frequency analysis of the above beam-membrane model with this understanding helps clarify why such odd behavior is observed. Consider the central beam, its adjacent linear membrane element, and another membrane element adjacent to the first, as shown in Figure 42. In this scenario, the beam is deflected vertically, as in Figure 36. Due to the tie

constraint, membrane one is forced to accept a rigid-body rotation and displace vertically at the right end, maintaining continuity of displacement with the beam. By definition, membrane elements are only able to transmit in-plane displacement; they can not accept out-of plane (transverse) strain or bending terms. Due to this formulation, membrane two in Figure 42 maintains continuity of in-plane (horizontal) displacement with membrane one, without rotation (due to lack of transverse shear). The result of these combined effects is the discontinuous "kink" seen in Figure 36. As the user refines the mesh, the angle between membrane elements one and two increases, approaching the limiting condition of element one being normal to element two. This results in the lack of convergence seen using linear membrane elements in Figure 35.

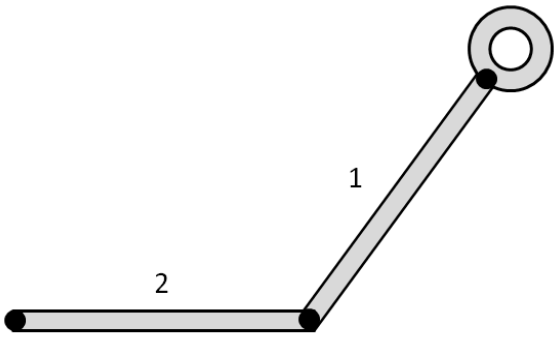

Figure 42: Schematic of a deflected wire beam connected to a linear membrane element, which is connected to another linear membrane element.

Although the above commentary describes the linear membrane elements, a similar effect is seen in the quadratic membrane elements. The key difference in their responses is their respective shape functions. As their names imply, linear serendipity elements have one node at each corner, and displace in a linear fashion along their edges, as shown in Figure 34. Conversely, quadratic serendipity elements have midside nodes between the corners, and displace according to a quadratic interpolation function. These interpolation functions are given in Ref. [44].

Another notable difference in the responses of the linear and quadratic elements is the displacement of membranes that are not adjacent to the wire beam. Figure 43 shows similar results as Figure 37, but with fewer quadratic membrane elements, to aid visibility. Due to the requirement of continuity of displacement at the nodes, the membranes adjacent to the center beam cause elements not connected to the beam to displace vertically. Furthermore, since the membrane elements have no bending stiffness, the slope is discontinuous at the nodes.

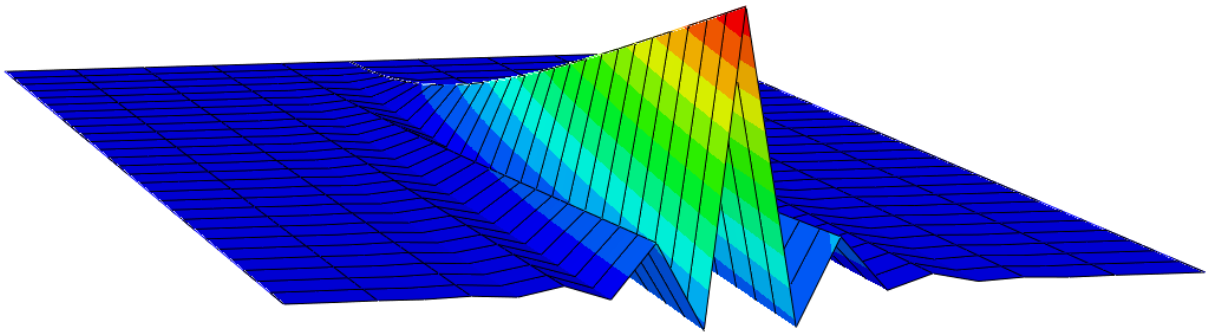

Figure 43: First modeshape of a three beam structure separated by quadratic membrane elements. Color bands denote *33*-displacement.

Despite their higher-order interpolation functions, the quadratic elements suffer from the same problem seen in the linear membrane elements: the discontinuity of slope at the nodes results in a loss of transmitted stress. Thus, the majority of the membrane section remains unaffected by the vibration of the central beam. From these studies, it is clear that a thin element capable of carrying bending and shear is required to describe the "membrane" tissue of the *Manduca Sexta* wing.

3.2.3. Modeling with Shell Elements

In light of the deficiencies of the membrane element for the purpose of modeling a *Manduca Sexta* wing, a shell element is selected for the next series of analyses. There are

essentially three types of shell elements used in Abaqus. The first type is a classical Kirchhoff shell, in which bending is restricted so that vectors normal to the midpoint of the shell surface remain normal after deformation. These elements are appropriate for sufficiently thin structures [44]. The second type of shell falls in the Mindlin plate family, in which bending is not restricted by the normal vector found in Kirchhoff elements. Shell elements of the Mindlin formulation are appropriate for thick plate scenarios [14]. The third type of shell element in the Abaqus library is the Koiter-Sanders shell. The Koiter-Sanders shell is a general-purpose shell, in which thickness is allowed to vary during deformation due to Poisson effects [1]. The general-purpose shell is a four-noded serendipity element resembling the membrane of Figure 32, but with all six degrees of freedom active. The Abaqus Theory Manual states the following regarding the Koiter-Sanders ("general-purpose") shell elements [1]:

> *The general-purpose elements provide robust and accurate solutions in all loading conditions for thin and thick shell problems. Thickness change as a function of in-plane deformation is allowed in their formulation. They do not suffer from transverse shear locking, nor do they have any unconstrained hourglass modes….No hourglass control is required for the axisymmetric general-purpose shells, nor in the bending and membrane response of the fully integrated element S4. The membrane kinematics of S4 are based on an assumed-strain formulation that provides accurate solutions for in-plane bending behavior….These elements use simplified methods for strain calculation and hourglass control and offer significant advantages in computational speed.*

With this knowledge, the previous exercise in which three beams were separated by two membrane sections was repeated. This time, the membrane sections were replaced by shell sections of the recommended Koiter-Sanders formulation. In light of the advantage offered by general-purpose elements, only four-noded, doubly-curved shells with reduced integration and hourglass control (S4R) were used; other shell types were excluded from this analysis. A total of 950 elements (1,020 nodes) were used in this example.

The first six modeshapes of this structure resembled plate-like modes, as though the beams were not present. The seventh modeshape, however, was of a configuration useful for comparison to the first modeshape of the beam-membrane analysis (shown below, in Figure 44). In this case, the central beam is flapping out of phase with the two end beams, but the shell elements are not exhibiting the discontinuities of displacement and slope observed in the membrane elements.

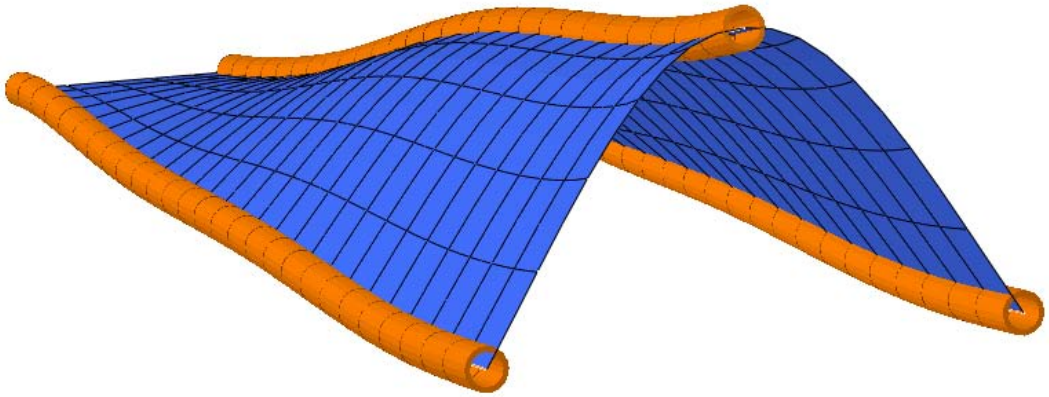

Figure 44: Seventh modeshape of a three beam structure separated by general-purpose shell elements.

The results shown in Figure 44 qualitatively resemble how one might expect the beam-shell structure to deform. Still, simply passing the first-glance "sanity-check" is an insufficient means of determining the appropriateness of the general-purpose, Koiter-Sanders element for modeling a *Manduca Sexta* forewing. With no physical beam-shell structure against which one might compare the finite element results, the efficacy of these shells remains in question. Fortunately there is another applicable structure with known frequency data and modeshapes.

Recall the results of the paper wing frequency tests, given in Chapter I of this document. A flat (non-cambered), paper wing of similar geometry to the *Manduca Sexta* forewing was scanned using a laser vibrometer. From these scans, natural frequencies and modeshapes were obtained for comparison to the actual *Manduca Sexta* wing. While these modeshapes proved

different than those of the hawkmoth wing at the third and higher modes, they nevertheless serve as an adequate basis for finite element model comparison.

3.2.4. Modeling a Paper Wing

Built into Abaqus is a feature in which the user can import an image, and trace over it to form sketches. These sketches can later be turned into parts. Using this method, a model of the paper wing was constructed with the same dimensions as the physical, paper wing. Figure 45 shows the completed outline of the paper wing. The wing used during modeling is truncated at the root so that the clamped portion of the wing (near the root) is not modeled. Instead, a fixed boundary condition is enforced at the left edge of the wing, denoted by the "V" in Figure 45[18].

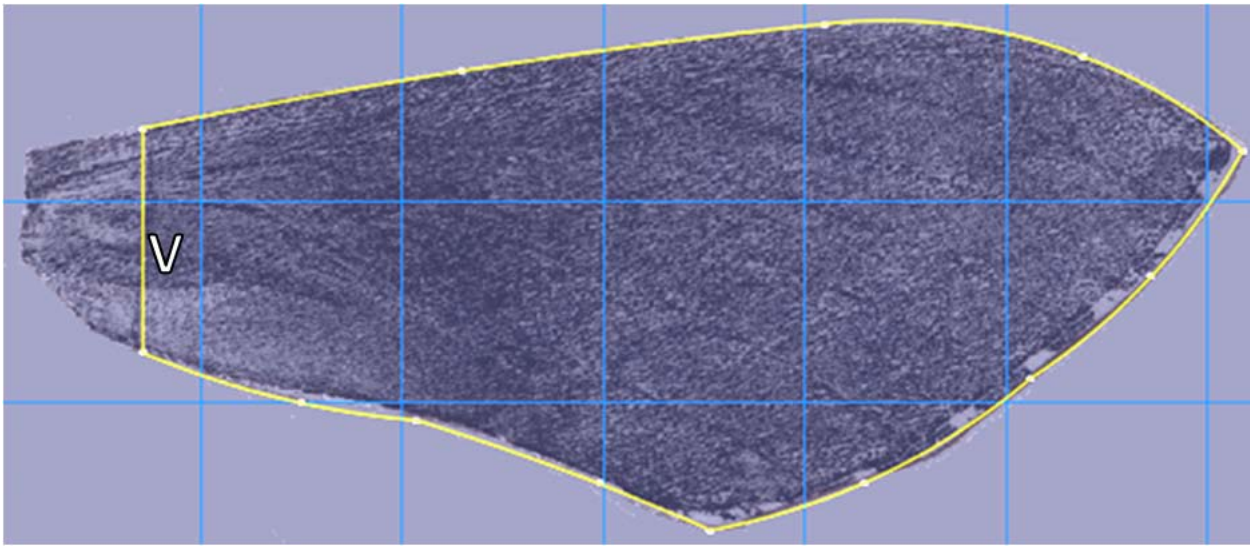

Figure 45: Geometry tracing of paper wing used in frequency experiments.

The wing model was meshed using the four-noded, doubly-curved shells with reduced integration and hourglass control (S4R) – the same Koiter-Sanders shell elements used in the previous analysis. A converged mesh of 929 of these general-purpose elements (1,016 nodes) was used. Material properties for the wing (made of copier paper) were obtained by calculating

[18] For comparison, see Figure 25.

the density based on known weight and volume measurements, estimating Poisson's ratio (assumed a value of 0.3), and changing Young's modulus until reasonable frequency values were obtained[19]. The results of this analysis are given below, in Table 9. As is evident from examining the values, even a poorly tuned model based on estimated material properties produces reasonably accurate results.

Table 9. Comparison of natural frequencies of a paper wing in vacuum, and an FE solution using general-purpose shell elements (S4R).

	Experimental Wing, Hz	**FE Result, Hz**
ω_1	20	22
ω_2	96	109
ω_3	162	159
ω_4	472	466

The modeshapes of the finite element model are also representative of those experimentally observed in paper wing. Recall from Chapter I, the first four modeshapes of the paper wing are, in order, first bending (or flapping), torsion, second bending, and finally the "saddle" mode with tip-deflection. The results of the finite element model of the paper wing are given below. Figure 46 shows the first modeshape, a bending mode; Figure 47 shows a torsional mode, Figure 48 gives the characteristic second-bending mode, and the modeshape shown Figure 49 resembles the saddle-mode with tip displacement noted in the paper wing.

The results of the finite element model – both the frequencies and modeshapes (displacements) – appear to sufficiently describe the paper wing tested in the vacuum chamber (modeshapes shown Chapter I, pages 39 through 41). Furthermore, the results of the modal analysis support the statement made in the Abaqus Theory Manual, in which the Koiter-Sanders elements were praised for their accuracy and robustness.

[19] Material properties used where: $\rho = 8.6\text{x}10^{-7}$ g/mm^3, $\nu = 0.3$, $E = 7.5$ MPa

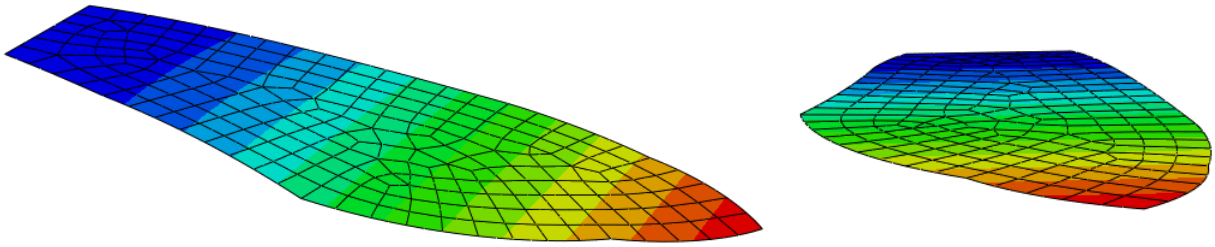

(a) (b)

Figure 46: First modeshape (22 Hz) of a flat, FE wing, shown from an isometric view (a) and a tip view (b).

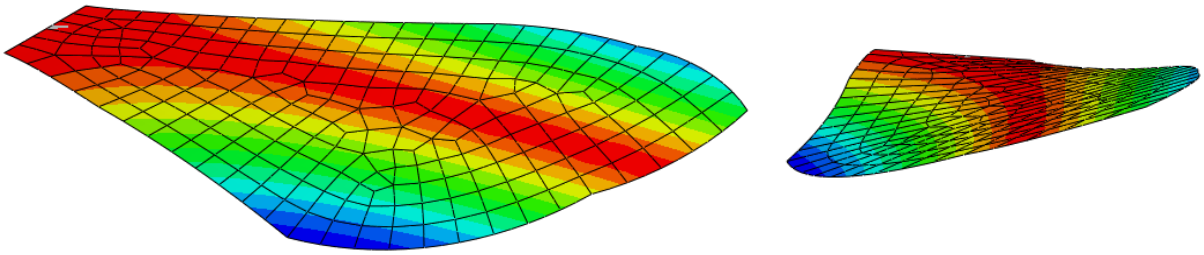

(a) (b)

Figure 47: Second modeshape (109 Hz) of a flat, FE wing, shown from an isometric view (a) and a tip view (b).

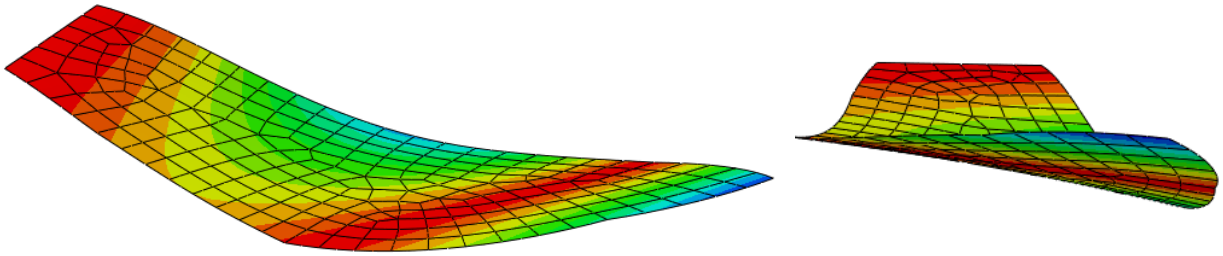

(a) (b)

Figure 48: Third modeshape (159 Hz) of a flat, FE wing, shown from an isometric view (a) and a tip view (b).

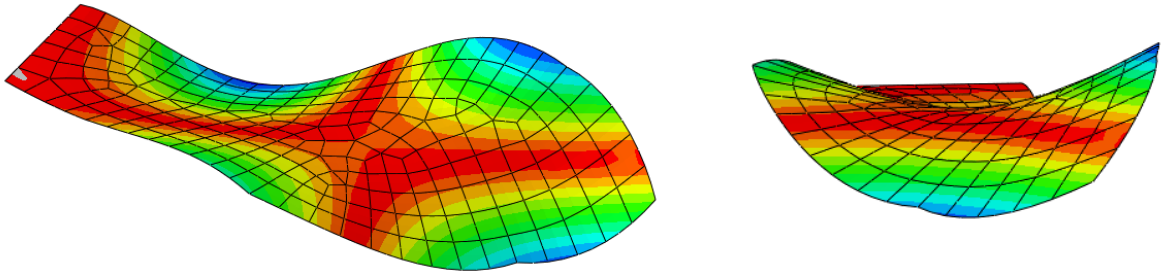

(a) (b)

Figure 49: Fourth modeshape (466 Hz) of a flat, FE wing, shown from an isometric view (a) and a tip view (b).

3.3. Camber Effects

Previous sections focused on the effects of various element types when modeling a flat wing. Based on the results, the quadratic beam and Koiter-Sanders shell were obvious choices. Despite promising results when comparing the finite element wing to the paper wing, neither provides a modal response similar to the actual wing. Indeed, at this stage in the structural dynamic analysis of the *Manduca Sexta* wing, it is unclear to what extent the response is dominated by camber or the presence of veins. To simplify the process of sorting camber and vein stiffness effects, the complexity of the finite element model will be incrementally increased. Now, we focus on camber.

Using an approach similar to that of Section 3.2.4, a model of a homogeneous, isotropic, cambered wing was constructed. However, in order to introduce camber without pre-stressing the wing, a slightly different approach to model creation was taken. This time, a curved surface of constant radius was created in Abaqus. Using the same photo sketching technique as before, the planform of the *Manduca Sexta* forewing was sketched onto a plane above the curved shell and projected downward, as shown in Figure 50. Finally, the material outside wing planform sketched on the curved surface was removed, leaving the cambered wing of Figure 51.

One of the disadvantages of using a planform view of a cambered wing to trace the venation structure is the loss of wing topography data. Despite any camber in the wing, a plan view of the venation structure is planar (*i.e.,* does not include three-dimensional topography). Thus, since the *Manduca Sexta* wing is a three-dimensional structure, a two-dimensional image simply cannot adequately describe the wing curvature. Creating a curved shell and sketching the venation pattern from the CT images as shown in Figure 50 helps to mitigate this loss in

topography data. Essentially, the goal of this method is to use a two-dimensional photo and an average value of camber to restore as much of the original wing geometry as possible.

The radius of curvature of the shell onto which the planform of the wing was projected is constant. In other words, all parts of the wing undergo the same camber. Conversely, the actual *Manduca Sexta* wing is not of constant curvature, with camber being dominant near the root. The camber value used in the model was achieved by examining images of the cross-sections from the CT scans. An arithmetic mean of the angle created between the leading edge and the wing centroid was taken[20] and used to construct a three-point arc. This arc was extruded and became the shell onto which the wing planform was sketched.

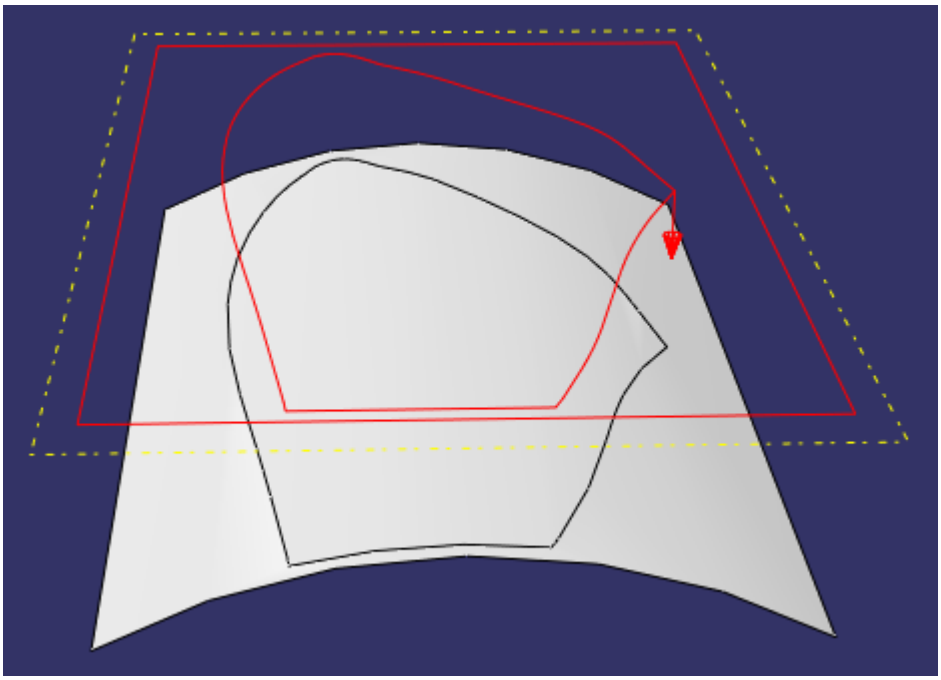

Figure 50: Projected *Manduca Sexta* wing planform used during cambered part creation. The part was sketched on the plane above the curved surface.

[20] This value was determined to be 15°, or 13% of the chord. An explanation of wing camber is found in Appendix D – Wing Camber.

(a) (b)

Figure 51: Cambered *Manduca Sexta* wing model. Shown are the isometric view (a) and tip view (b)

The wing shown in Figure 51 was meshed with the four-noded, doubly-curved shells (S4R) used previously. Nine hundred elements covered the cambered wing during the frequency analysis. In order to make a direct comparison to the flat wing model, the material properties of paper were used during the cambered analysis. For comparison, the frequency results for the flat and cambered cases are given below, in Table 10. By examining the results of both cases, one immediately finds that the curvature of the wing dramatically increases its stiffness.

Table 10. Comparison of natural frequencies of flat and cambered wing FE solutions, using general-purpose shell elements (S4R).

	Flat Wing, Hz	**Cambered Wing, Hz**
ω_1	22	159
ω_2	109	173
ω_3	159	797
ω_4	466	1057

The modeshapes of the cambered wing analysis are given in the figures below. The first modeshape, shown in Figure 52, differs slightly from that of the flat wing. Although the wing is still displacing in a fashion reminiscent of classical first bending, a large portion of the movement is now seen in along the trailing edge instead of at the tip. The second modeshape, however, appears to be similar in many respects to the deformations of the flat wing. Here,

torsion is the primary driver, though the axis of rotation also seems to have shifted slightly towards the trailing edge.

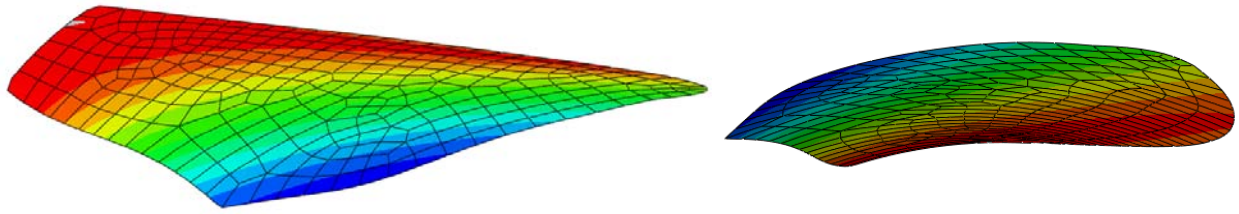

(a) (b)

Figure 52: First modeshape (159 Hz) of a cambered, FE wing, shown from an isometric view (a) and a tip view (b).

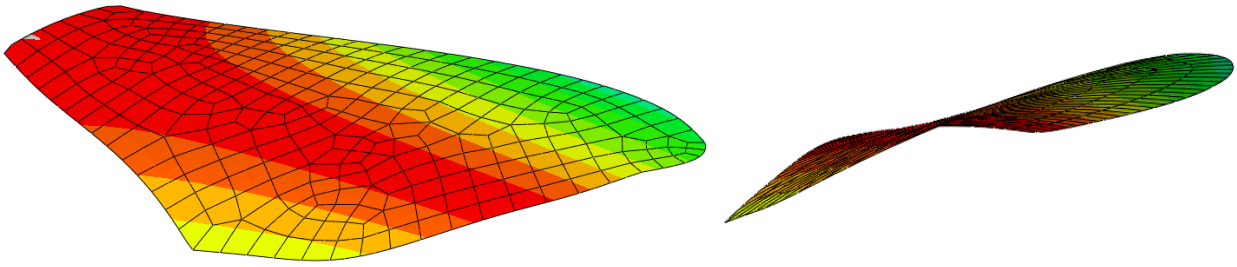

(a) (b)

Figure 53: Second modeshape (173 Hz) of a cambered, FE wing, shown from an isometric view (a) and a tip view (b).

The third modeshape, shown below in Figure 54, is by far the most striking evidence of the effect of cambering the wing. Here, the third mode is of a saddle shape, with similar deflections to the third mode of the actual *Manduca Sexta* forewing. This is an obvious departure from the flat wing analyzed previously, in which an extra second-bending mode was observed, pushing the saddle mode to the fourth position. The appearance of the saddle modeshape (corresponding to the third mode) indicates that camber is an important feature in the frequency response of the *Manduca Sexta* wing. Moreover, the large midside deflections at the leading and trailing edges of the homogeneous shell model highlight the structural importance of the stiffness imparted by the veins. By contrast, the hawkmoth wing shows little midside action in the third eigenvector, likely due to the added vein stiffness.

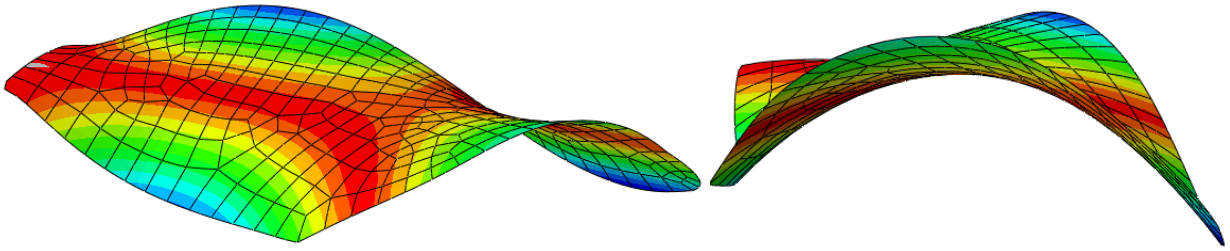

(a) (b)

Figure 54: Third modeshape (797 Hz) of a cambered, FE wing, shown from an isometric view (a) and a tip view (b).

The preceding study of camber effects on natural frequency was repeated for several values between zero and 15° (13% of chord)[21]. The same homogeneous, isotropic wing meshed with general-purpose shells was used. The results are plotted below, in Figure 55. The first natural frequency increases linearly with camber, while the second mode, also increasing, is substantially less affected by a change in camber. The third mode has the unique distinction of changing modeshapes during this analysis. At low camber values (less than 4.5% chord), the third modeshape is the second bending mode observed previously in flat wings. Above the cutoff value of 4.5% of chord, the camber-induced stiffness eliminates the second bending mode. Here, the saddle mode experiences a negative frequency shift, and becomes the third mode observed in the *Manduca Sexta* wing. It is notable that the second bending and saddle modes do not experience a mode reversal at high camber values. Instead, the second bending mode simply disappears – or changes shape so dramatically that it can no longer be characterized as "second bending." Regardless of the modeshape presented, the third mode is strongly affected by even slight changes in camber.

[21] The camber in the *Manduca Sexta* wing varies from 0 % c to approximately 20%c, with an average of approximately 13 %c.

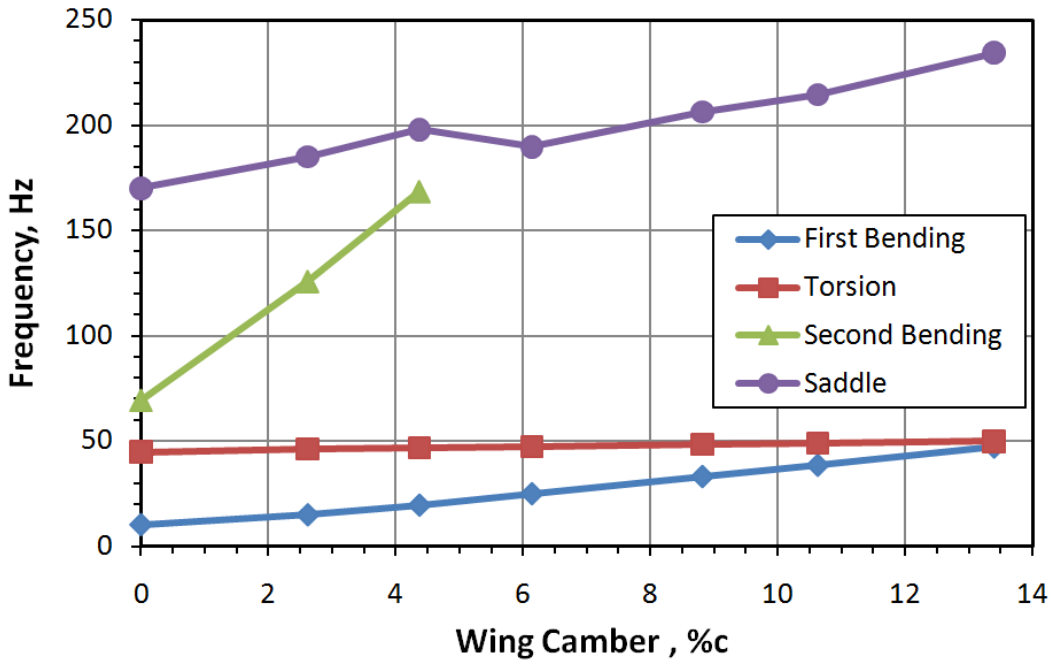

Figure 55: Effects of camber on natural frequency in a homogeneous *Manduca Sexta* wing.

3.4. Vein Effects

The *Manduca Sexta* wing is partially characterized by an intricate arrangement of veins, primarily arranged in the spanwise direction. At this point, it seems that the modeshapes are primarily dominated by planform in the first two modes, and camber in the third and higher modes. Still, the associated modeshapes show significant midside motion not observed in the hawkmoth wings – a likely indicator that the veins are structurally significant. From a future development standpoint, a significant cost savings may be realized by increasing the diameter of the veins. Recreating the small-diameter veins observed in the *Manduca Sexta* wing would involve manufacturing wing spars on the micro-scale, thus requiring great precision during manufacturing. With this view in mind, increasing the vein diameter is desirable; doing so lowers production costs and increases the wing volume, thus reducing intra-vein stress. These considerations invite a study of the structural dynamic effects of increasing vein diameter.

The presence of these veins causes one to ask several questions regarding their importance. Do they serve in a primarily circulatory capacity? Asked another way, to what extent do they influence the structural response of the wing? How significant is the thickness (diameter) of the vein structure? To answer these questions, a flat model of the *Manduca Sexta* wing was constructed in Abaqus. Although it is true that previous model results indicated that camber affects the response of the structure, it is equally important to isolate the impact of adding veins from that of adding camber.

3.4.1. Vein Contributions to Modal Behavior

The flat wing model was devised using the same photo-tracing method as the paper wing model. The beams (veins) are prismatic, each having a unique cross-section. Cross sectional properties of each vein were averaged using the CT measurements. The membrane (denoting tissue, not an element type) is also of constant thickness (0.12 mm) at all points[22]. The three-noded quadratic beam (B32) and membrane sections (four-noded general purpose shell, type S4R) were tied together, enforcing continuity of displacement and rotation among beam and shell elements. Figure 56 shows the assembly used during analysis.

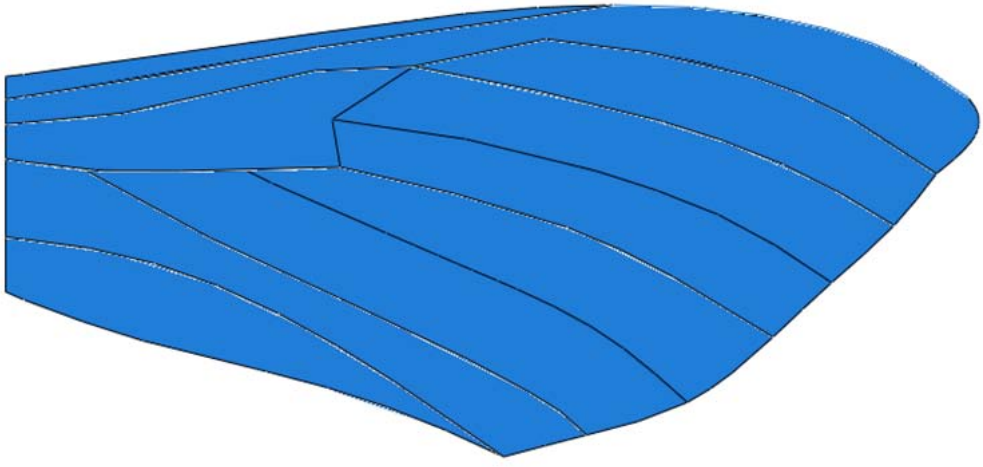

Figure 56: Assembly of vein (quadratic beam) and membrane (Koiter-Sanders shell) sections.

[22] Very little variation in membrane thickness was observed during the CT scans.

The inclusion of veins raises an important question regarding the material properties of the wing structures. To date, no work has been published on the material properties of the *Manduca Sexta*; however, follwing their work with the *Tibicen Canicularis* (cicada), Mengesha, Vallance, Barraja and Mittal published material property values for that species [25]. Table 11 gives the reported values for the cicada wing, obtained through a nano-indentation procedure. Note that the thickness of the cicada membrane is close to that of the *Manduca Sexta* – a heartening result.

Table 11. Material properties of a *Tibicen Canicularis* (cicada) reported by Mengesha, Vallance, Barraja, and Mittal.

	Veins	**Membrane**
Mass Density, g/cm^3	2.30	2.30
Young's Modulus, GPa	1.90	3.70
Poisson's Ratio	0.495	0.495
Thickness, μm		12.20

The Young's modulus of the membrane is greater than that of the veins in the cicada wing. This result is not surprising, since many entomologists have noted that there are two basic classes of insect wings: stiff and flexible. The *Tibicen Canicularis* (cicada) is of the order *Hemiptera*, and has a rigid wing [25], while the *Manduca Sexta* has a flexible wing, as do most insects in the order *Lepidoptera* [40]. As a result, the initial hawkmoth model constructed in Abaqus uses the material properties of the *Tibicen Canicularis*, but in reverse: the hawkmoth veins are assumed to be stiffer than its membrane.

The quadratic beam, Koiter-Sanders shell setup provided an accurate solution in Section 3.2. Building on this approach, the wing shown in Figure 56 was meshed with three-noded quadratic beams (B32), and four-noded general-purpose shells (S4R). A Lanczos method eigenvalue solver was used to compute the modes and modeshapes of the first three modes. The

natural frequencies obtained from this analysis are given below in Table 12. The robustness of the selected elements was evident from a convergence study that showed virtually no change with mesh refinement[23].

Table 12. Natural frequencies of a flat *Manduca Sexta* wing model

	Frequency, Hz
ω_1	41
ω_2	91
ω_3	225
ω_4	308

The modeshapes of the flat *Manduca Sexta* wing model are shown in the figures below. By now, the first two modeshapes are familiar; the planform dictates first bending and torsion at the first and second modes, respectively. The third modeshape shows some deviation from the flat paper wing and its model. Instead of the deformations resembling pure second-bending seen previously, the beams influence the modeshape to add significant flattening near the tip. Still, the third modeshape has many aspects that appear similar to second-bending, and is not seen experimentally in the *Manduca Sexta* wing.

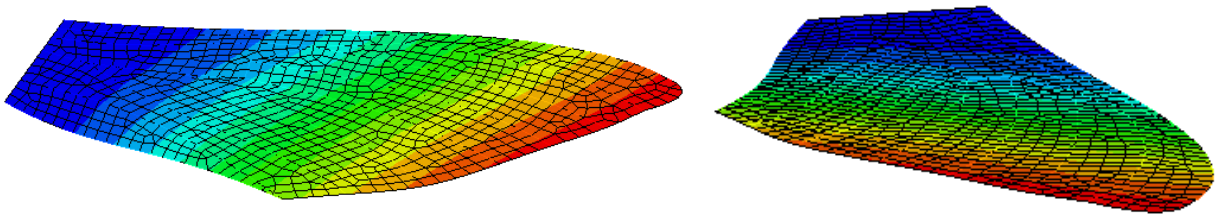

(a) (b)

Figure 57: First modeshape (41 Hz) of a flat, FE wing with added veins, shown from an isometric view (a) and a tip view (b). Color bands denote displacement.

[23] Largest change of any mode was 1.5 Hz when the mesh was refined from 348 elements to 4,121.

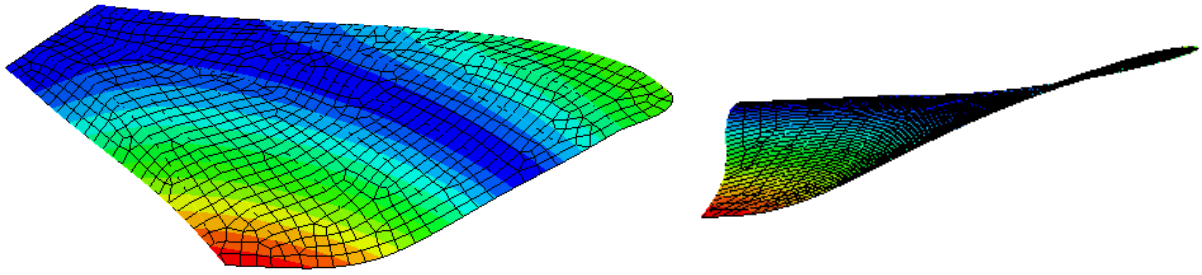

(a) (b)

Figure 58: Second modeshape (92 Hz) of a flat, FE wing with added veins, shown from an isometric view (a) and a tip view (b). Color bands denote displacement.

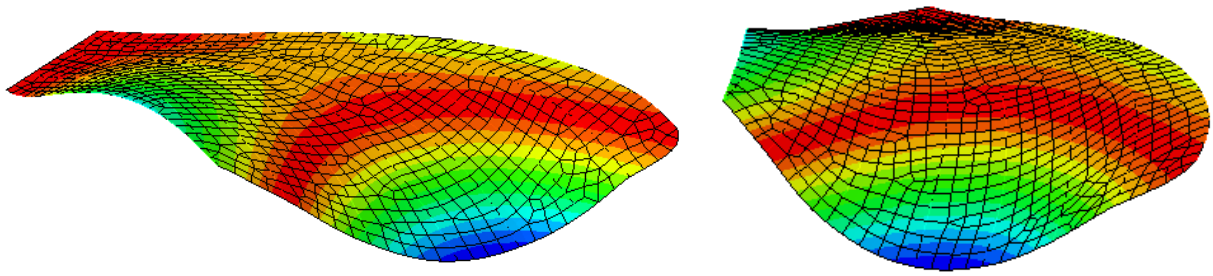

(a) (b)

Figure 59: Third modeshape (225 Hz) of a flat, FE wing with added veins, shown from an isometric view (a) and a tip view (b). Color bands denote displacement.

The fourth modeshape is shown below, in Figure 60, and is similar to the saddle mode seen previously. Adding the vein (beam) structure has shifted the central axis toward the trailing edge, and they are now nearly parallel. Accompanying the axis shift is a more prominent tip deflection than previously observed. Also notable is the lack of midsection motion in the leading and trailing edges, resembling the *Manduca Sexta* more than previous models. The midsection stiffness and the presence of the third (extra) mode not seen in the cambered model are indicative that both venation and camber are important structural characteristics.

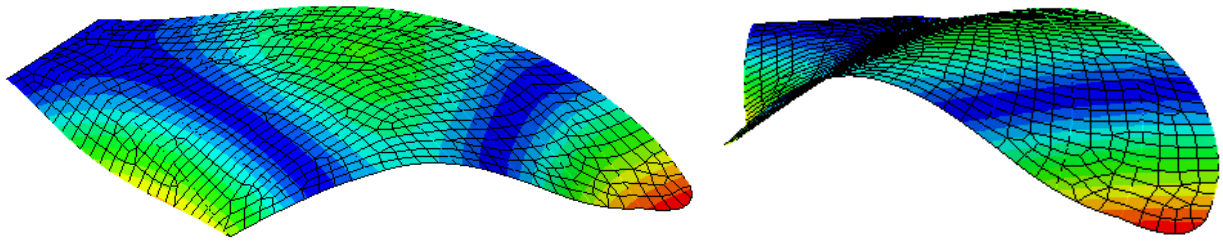

(a) (b)

Figure 60: Fourth modeshape (308 Hz) of a flat, FE wing with added veins, shown from an isometric view (a) and a tip view (b).

3.4.2. Effects of Vein Thickness (Diameter)

The preceding finite element case studies have provided valuable insight into the level of sophistication needed to reproduce a synthetic *Manduca Sexta* wing. From the results, it is apparent that the wing cannot consist of a single, homogeneous part. Moreover, to avoid a pseudo-homogenous response, the veins must have a Young's modulus greater than the membrane, due to their volume fractions. Likewise, the finite element models indicate camber is required to prevent spurious modes. From a manufacturing standpoint, it is important to gage how sensitive the wing is to changes in vein thickness (diameter). Tolerance control and uniqueness of vein geometry will almost certainly drive costs higher. Additionally, should it be proven that the wing is highly sensitive to changes in vein geometry, techniques offering greater resolution than CT scans will likely be required.

Using the flat wing model shown in Figure 56, a study of the effects of vein thickness on natural frequency was conducted. In this study, a vein thickness factor was defined as a coefficient that acted uniformly on all veins (*e.g.*, a thickness factor of 2 doubled the diameter of all veins). Throughout this study, a refined, converged mesh was held unchanged, using quadratic beams and general-purpose shell elements to model the veins and membranes, respectively. Based upon the previous assertion that the *Manduca Sexta* has a flexible wing

structure, th e ma terial properties o f *Tibicen Canicularis* veins a nd m embrane were a gain reversed. The results of the vein thickness study are plotted in Figure 61. Examining the results of t he f requency vs . v ein t hickness pl ot r eveals a c ommon t heme: t he f irst t wo na tural frequencies i ncrease n early l inearly w ith v ein s tiffness (via d iameter), a nd at t he s ame r ate; conversely, t he t hird m ode i s s trongly a ffected b y v ein t hickness (thus s tiffness). The t hird modeshape i s a second bending m ode a t l ow s tiffness v alues, a nd t he fourth m ode i s a s addle mode. Increasing t he v ein di ameter be yond 12 0% of t he m easured values causes the second bending m ode t o di sappear; w hen t his oc curs, the saddle m ode ex periences a r eduction i n frequency and becomes the third mode.

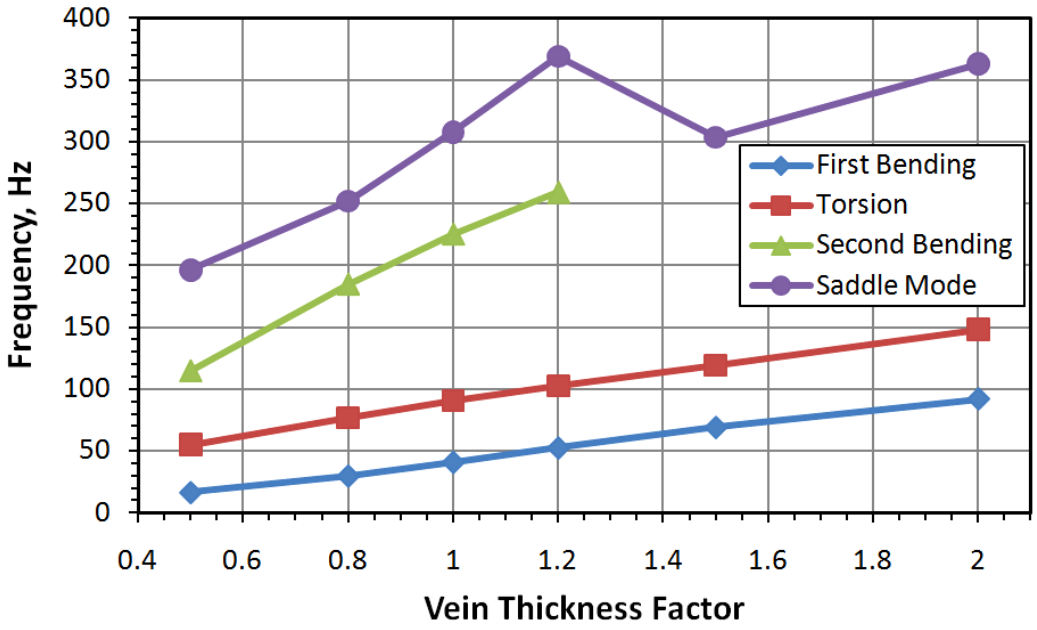

Figure 61: Natural frequency as a function of vein t hickness for a f lat wing, us ing r eversed *Tibicen Canicularis* material p roperties. A v ein t hickness o f 1 i s equivalent to t he av erage m easured value for each individual v ein. A verage v ein r adii v ary from 0.07 mm to 0.6 mm.

The validity of the hypothesis that the material properties of *Lepidopterae*[24] are the reverse of those of the *Hemipterae*[25] remains in question. To test this position, the previous study of vein thickness effects on natural frequency was repeated using the material properties from the *Tibicen Canicularis* (cicada), reported by Mengesha, Vallance, Barraja and Mittal [25]. The results of this analysis are plotted below, in Figure 62. The stunning conclusion is that the natural frequencies are nearly identical when the material properties are reversed (even though the membrane is nearly twice as stiff as the veins in the cicada). The same behavior as before is observed: there are small variations in the first and second natural frequencies with vein thickness, and a strong correlation of the third and fourth modes with vein thickness. As seen previously, increasing the vein thickness beyond a certain point results in the elimination of the second bending mode.

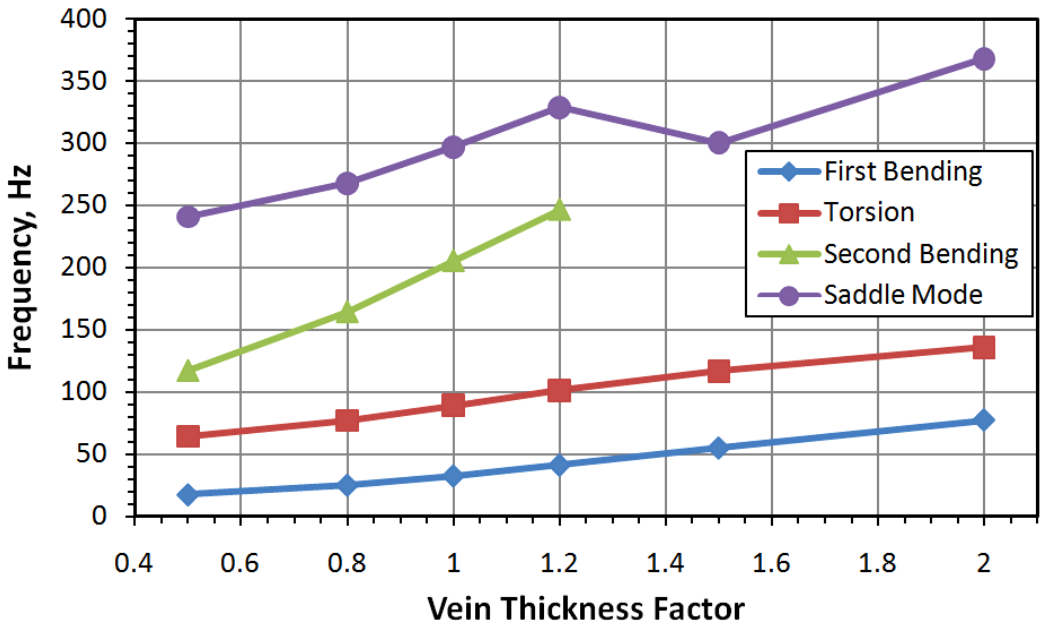

Figure 62: Natural frequency as a function of vein thickness for a flat wing, using *Tibicen Canicularis* material properties.

[24] Order to which the *Manduca Sexta* belongs
[25] Order to which the *Tibicen Canicularis* (cicada) belongs

As one might expect from a theoretical standpoint, the preceding investigations of material properties, camber, and vein dimensions reveal a possible non-uniqueness of modal solutions. Indeed, structural stiffness, *EI*, is a combination of material property and moment of inertia effects, in which an inadvertent underestimation of one contributing factor may be compensated for by a corresponding overestimation of another. With Young's modulus, Poisson's ratio, and density estimated (but unknown), and geometric measurements limited by the resolution of the CT scans, producing a validated structural model of a *Manduca Sexta* may be possible, albeit non-unique.

IV. Results and Discussion

A finite element model of a *Manduca Sexta* forewing was constructed in Abaqus for comparison to experimental frequency data. Throughout the model creation process, there were two competing requirements: maximizing geometric simplifications to ensure tractability, and minimizing unnecessary deviation from the physical structure to preserve the accuracy of results. The trade studies of Chapter III were heavily relied upon to produce a model that most accurately reflected the *Manduca Sexta* forewing, and to help understand its shortcomings. In light of the preceding investigation of appropriate element selection, four-noded, general-purpose (Koiter-Sanders) shells were used to model the wing membrane tissue, and three-noded quadratic beams served to represent the vein structure.

This chapter is organized chronologically beginning with model construction, to include material properties. Frequency analysis and convergence study results are shown, followed by a discussion of the model limitations. Recommendations are made regarding possible methods to improve the modeling process. With the model limitations in mind, a scaling factor is developed that normalizes the Abaqus and Polytech scanning laser outputs, and a stress analysis of the first two modes is conducted.

4.1. Model Construction

The finite element studies in Chapter III reveal that the natural frequencies of the *Manduca Sexta* wing are strongly correlated to camber and vein thickness (geometry), but only weakly correlated to material properties within the range of 2–5 GPa. Consequently, both camber and vein thickness variation as a function of span were included in the finite element

model. It was also assumed (without verification[26]) that the material properties of the *Manduca Sexta* are reasonably close to those of the *Tibicen Canicularis*.

An average camber value was computed based on CT measurements, and formed the foundation of the model. Using the approach described in Chapter III, a prismatic shell of constant curvature was extruded, creating a rectangular planform with constant thickness. A planform sketch of the *Manduca Sexta* wing was then projected onto the surface of the extruded shell, as shown in Figure 63. Next, an extruded cut was performed to eliminate material outside the wing planform, resulting in a similar wing to the one shown previously (see Figure 56).

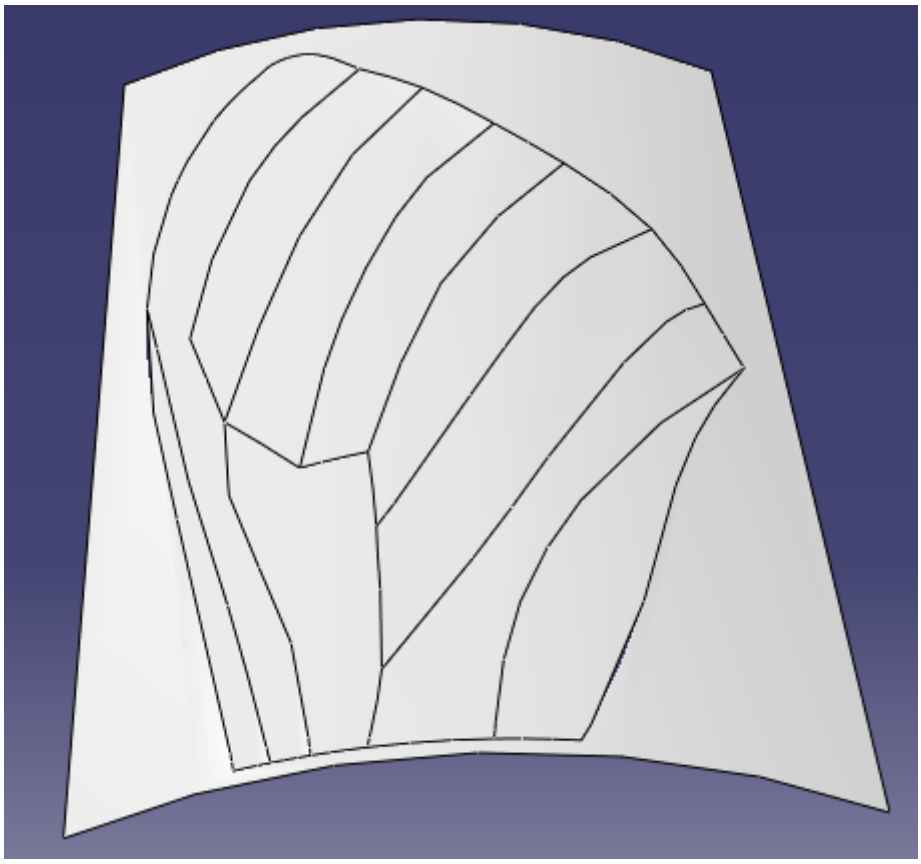

Figure 63: Planform sketch of a *Manduca Sexta* wing, projected on to a curved surface to simulate an average camber.

[26] Preliminary nano-indentation studies by O'Hara place the Young's modulus of dry, aged *Manduca Sexta* wings between 2 and 5 GPa [31]. Material properties for the veins have yet to be determined.

The venation shown in Figure 63 consists only of partition sketches, not parts, that effects only the mesh construction. Unfortunately, Abaqus/CAE currently lacks the capability to convert partition geometry to wire parts[27]. To circumvent this problem, a fine mesh of general-purpose shell elements (S4R) was created on the part shown in Figure 63. Using the script given in Appendix A – CoordGen, the coordinates of the nodes corresponding to the locations of the vein partitions were extracted from the Abaqus input files. These coordinates were imported into SolidWorks to create splines that were then exported as wire parts. With each of the veins saved as wire parts in a standardized format (IGES), they were imported into Abaqus and mated with the partition sketches from which they were created. Consistent with the vein-membrane models of Chapter III, the beams and their adjacent shells are held together using the "tie" constraint, forcing continuity of displacement at the beam nodes.

Beam sections (profiles) were created using the CT cross-section measurements. Each vein (beam) cross-section changes at different spanwise locations, and tapers at its own, unique rate. To reflect this behavior in the finite element model, veins were sectioned at irregular intervals based on changes in the CT measurements. Between each of the section locations, an average value of vein thickness was computed, and a new section was created when the vein thickness varied by more than 10% from the average section value. Since Abaqus/CAE lacks the capability to create tapered sections, beam cross-section changes occurred discontinuously. Figure 64, below, shows the *Manduca Sexta* wing model color-coded by cross-section.

The beams (veins) were tied at the midsection of the shells (membrane tissue) in the model of Figure 64 for two reasons. Recall Figure 19, the CT image of a wing cross-section near the root. From this figure it is evident that some of the veins pass through the midsection of the membrane structure, while others do not. Those veins that do appear to hang below the

[27] The author has requested this feature, and Simulia has agreed to include it in a future release of Abaqus/CAE [30].

membrane do s o near the root, and are gradually engulfed by the membrane as the vein tapers with span. Second, all veins, at all points, are surrounded by a thin coating of membrane in the actual *Manduca Sexta* wing. When modeling the membrane path (over or through) the veins, it was assumed that the thin layers of membrane above and below the veins were of roughly the same mass moment of inertia as an idealized membrane passing through the midsection.

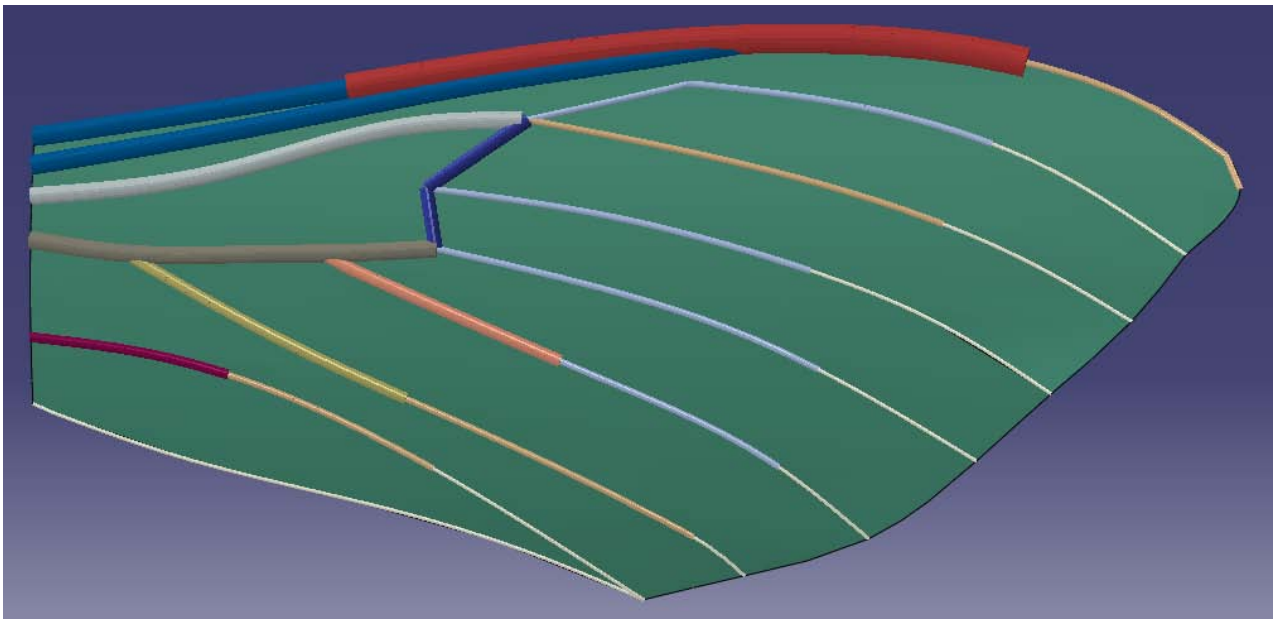

Figure 64: Planform view of a finite element model of a *Manduca Sexta* forewing, color coded by cross-section dimension.

In light of the previous studies asserting that the *Manduca Sexta* wing is far more flexible than the *Tibicen Canicularis* wing, and O'Hara's preliminary findings regarding the membrane modulus [31], the material properties used mirrored the reversed cicada properties. With the exception of the modulus of elasticity of the veins, all properties are the same as the *Tibicen Canicularis*; here, Young's modulus was increased slightly (7.5%), from 3.7 GPa to 4.0 GPa. Table 13 shows the material properties used during model construction.

Table 13. Assumed values of material properties for a *Manduca Sexta* (hawkmoth) wing.

	Veins	**Membrane**
Density, g/cm^3	2.30	2.30
Young's Modulus, GPa	4.00	1.90
Poisson's Ratio	0.495	0.495
Thickness, μm		12

4.2. Mass Properties

During the experimental phase of his research Norris demonstrated that the camber and frequency response of the *Manduca Sexta* wing change dramatically after approximately three hours, with mass being less dramatically effected [29]. As a result, preserving the freshness of the wing during CT and frequency investigations was of the upmost priority. Estimation of the wing mass was conducted using fresh-wing data previously acquired by Norris.

In the initial phase of his work at AFIT, Norris only conducted vibration experiments in air. During this time, one of his primary objectives was to develop a statistical database of *Manduca Sexta* wing properties. Using his data, the average wing mass was 0.0416 grams, with a standard deviation of 0.0037 grams. In comparison, Abaqus determined the mass of the finite element model to be 0.040 grams, well within one standard deviation of the average *Manduca Sexta* wing mass. This result lends further credence to the assumption that the material properties of the *Tibicen Canicularis* (cicada) are likely close to those of the *Manduca Sexta*.

4.3. Frequency Analysis Results

The wing model shown in Figure 64 was meshed with three-noded quadratic beams and four-noded, doubly-curved, shells, using a reduced integration formulation of 11 through the thickness integration points. The first three natural frequencies of this model (converged values)

are presented in Table 14, and compared to the experimentally obtained values of the *Manduca Sexta* forewing.

Table 14. Natural frequency results of a *Manduca Sexta* FE model, and comparison to experimental values.

	Experimental, Hz	**FE Model, Hz**	**Minimum Difference**
ω_1	86 ± 2	84.6	0.0%
ω_2	106 ± 2	106.1	0.0%
ω_3	155 ± 2	317.7	102.4%

Table 15. Comparison of frequency ratios of *Manduca Sexta* and FE wings.

	Experimental, Hz	**FE Model, Hz**	**Minimum Difference**
ω_2/ω_1	1.23 ± 0.05	1.25	0.0%
ω_3/ω_1	1.80 ± 0.07	3.91	100.8%

It is immediately obvious that the first two natural frequencies of the *Manduca Sexta* wing and the finite element model match very well, as does their ratio. The finite element model does not adequately match the third mode, however. The predicted third natural frequency and its ratio to the fist mode differs from experimental values by a factor of roughly two. As previous studies have shown, the third mode is the most sensitive (of the three modes considered) to stiffness effects resulting from camber, cross-sectional shape, and material property variation.

Not surprisingly, the first two modeshapes of the finite element model correlate well with the experimental results seen in the *Manduca Sexta* wing. The first modeshape of the finite element wing is plotted below, in Figure 65[28]. This modeshape is the familiar first bending

[28] For readability's sake, the most refined (converged) mesh is not shown in the figures. The converged mesh contains so many elements that the color bands denoting displacement are no longer visible due to the black outline of the elements.

mode, with color bands denoting magnitude of displacement. As seen experimentally in the *Manduca Sexta* wing, the wing displacement is a function of span, with little variation in the chordwise direction.

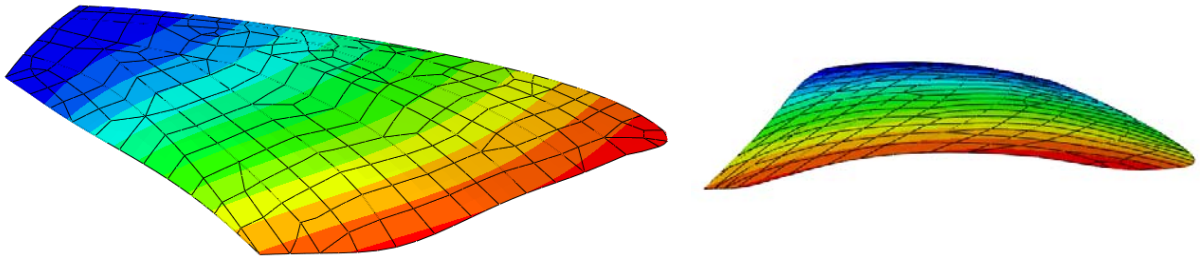

(a) (b)

Figure 65: First modeshape (84.6 Hz) of FE *Manduca Sexta* wing model, shown from an isometric view (a) and a tip view (b).

The second modeshape is a torsional mode, and is plotted in Figure 66. Unlike the torsional modes seen in Chapter III, the second modeshape of this model does not affect the wing in a rigid, plate-like fashion. That is, instead of the entire wing (or a majority of it) rotating as a single, planar unit about a central axis, the wing of Figure 66 shows significant curvature in the tip view. This deflection is consistent with the second modeshape of the *Manduca Sexta* wing, shown in Figure 23. In both cases, the central axis, about which the rotation occurs, is offset slightly forward of the half-chord line. Moreover, the finite element model accurately predicts that the vertical displacement of the trailing edge has a slightly greater magnitude than that of the leading edge.

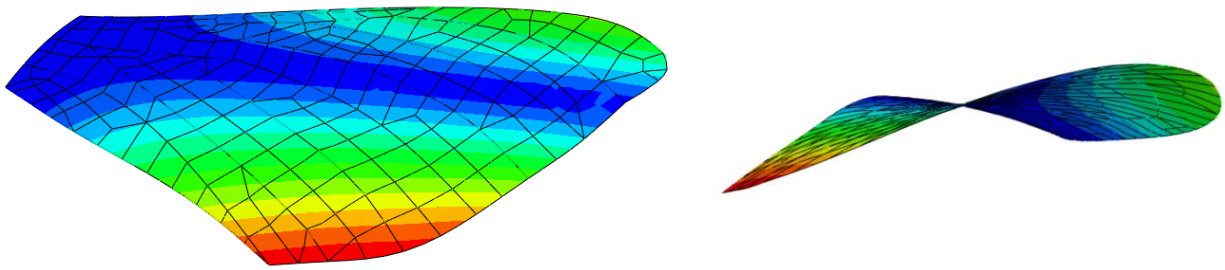

(a) (b)

Figure 66: Second modeshape (106.1 Hz) of FE *Manduca Sexta* wing model, shown from an isometric view (a) and a tip view (b).

The third modeshape is a saddle-mode and is shown below, in Figure 67. Although the frequency value predicted by the finite element model does not coincide with the 155 Hz value observed in the hawkmoth wing, its modeshape is stunningly similar. Like the saddle mode shown in Figure 24, the finite element model predicts a smooth deflection of nearly constant radius from the tip view. Likewise, the chordwise deflection is angled, so that the axis of rotation is slightly off center, giving the trailing edge the greatest magnitude of deflection in the vertical direction. This effect causes the trailing edge slope to be greater than that of the leading edge; as a result, the root is visible in the upper left corner of Figure 67 (b) – mimicking the *Manduca Sexta's* response in Figure 24 (b).

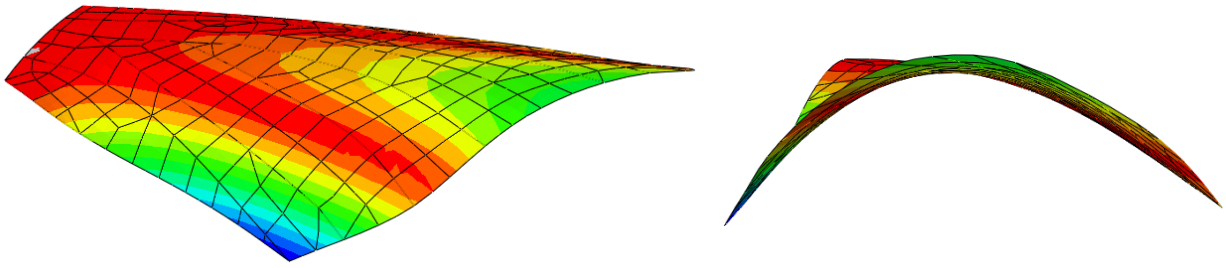

(a) (b)

Figure 67: Third modeshape (317.7 Hz) of FE *Manduca Sexta* wing model, shown from an isometric view (a) and a tip view (b).

4.4. Convergence Studies

Convergence studies were carried out to ensure accuracy of the finite element solutions. Mesh sizes between 295 and 80,633 elements were investigated, and the results of these studies are plotted in the figures below. For each mode, the trend observed in the convergence plots is the same: as the mesh size is increased, the solution obtained by the eigenvalue solver decreases to some asymptotic value. In this analysis, the mesh was considered sufficiently refined when a large change in the number of elements produced a frequency shift of less than one percent in

any mode. During the convergence studies, the number of beams and shells was controlled by assigning a global seed size, thus controlling the length of any single element along its edge. Curvature control was enforced to ensure that highly curved surfaces were adequately meshed.

A solution satisfying the above convergence criterion was found with a mesh consisting of three-noded quadratic beam elements (B32) and four-noded general-purpose shell elements. The converged mesh used a total of 80,633 elements (83,664 nodes). The second most refined mesh contained 13,969 elements (15,330 nodes), and had a maximum frequency shift of 1.0% (in the third mode) from the converged solution. Since the most refined mesh contained more than six times the number of elements as the second most refined mesh but lacked significant variation in frequency values, the solution was considered sufficiently converged. From a computational standpoint, an efficient solution was obtained with 3,850 elements (4,570 nodes), at which point all modes were within 1.5% of the converged value obtained with 80,633 elements. Likewise, the robustness of the selected elements is evident in the solution obtained with only 636 elements (896 nodes); here, the largest difference with the converged solution is 2.8%, observed in the second mode. Table 16 indicates the number of elements and nodes used during the convergence study, and how many of these elements were beams (B32) and shells (S4R).

Table 16. Number of elements and nodes (and of which type) used during convergence studies.

Total Elements	Nodes	Beams (B32)	Shells (S4R)
251	389	116	135
316	481	138	178
428	627	167	261
636	896	221	415
1,199	1,582	332	867
3,850	4,570	658	3,192
5,754	4,774	823	4,931
13,969	15,330	1,314	12,655
80,633	83,664	3,285	77,348

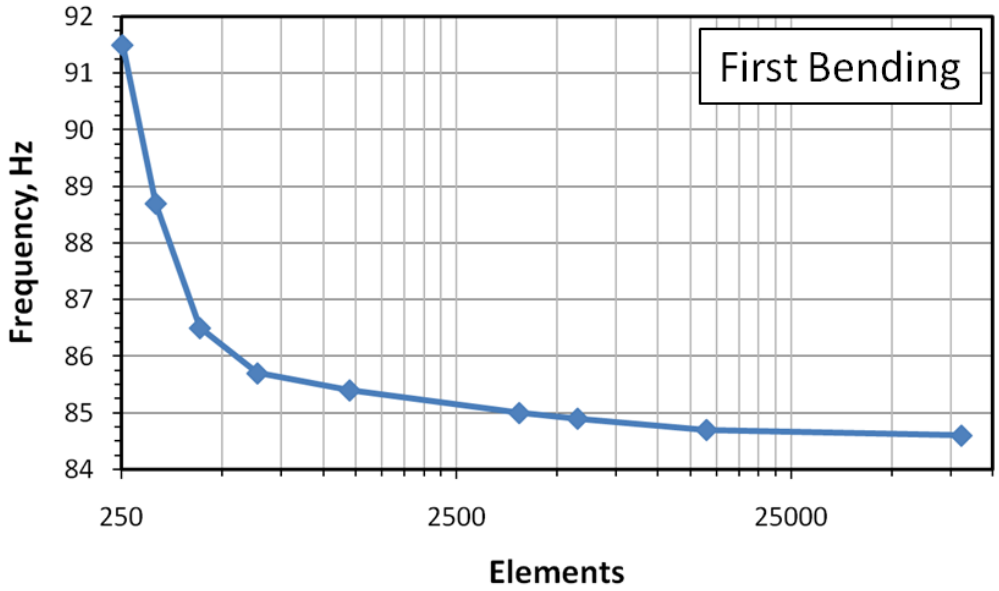

Figure 68: Convergence study results for the first mode of a *Manduca Sexta* finite element model.

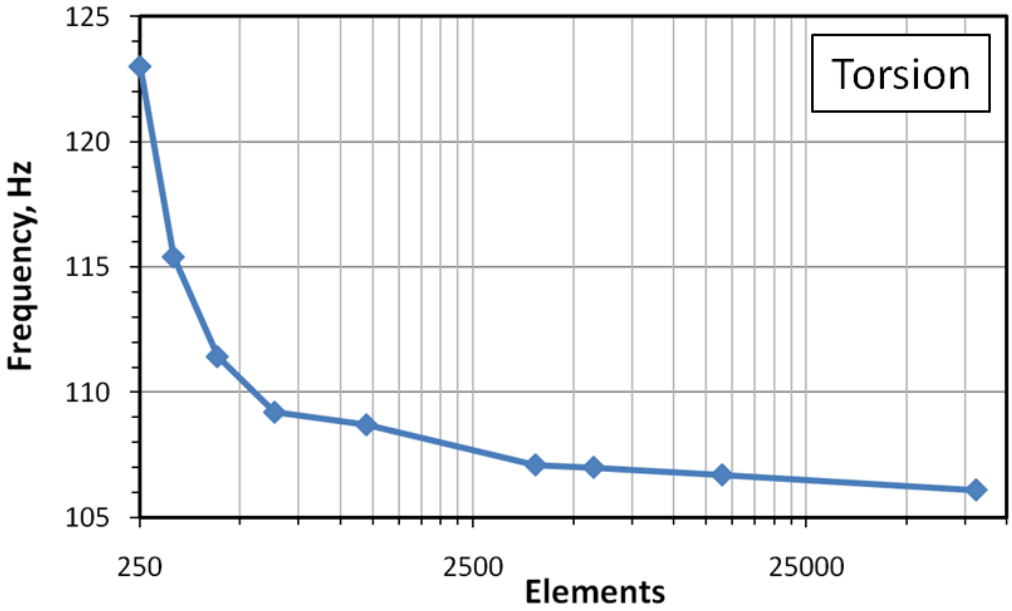

Figure 69: Convergence study results for the second mode of a *Manduca Sexta* finite element model.

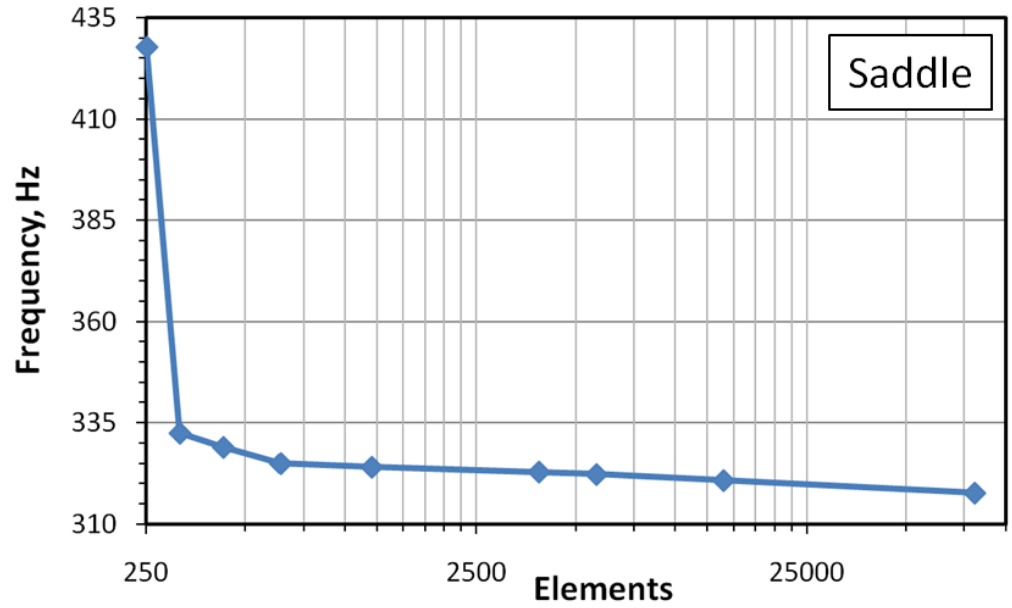

Figure 70: Convergence study results for the third mode of a *Manduca Sexta* finite element model.

4.5. Model Limitations

Before undertaking a numerical analysis of the *Manduca Sexta* wing, one of the stated objectives was to develop a finite element model capable of adequately representing the first three natural frequencies and their associated modeshapes. The above results indicate that the finite element model produced acceptable results for the first two frequencies and modeshapes. While the third modeshape appears qualitatively similar to the saddle mode observed in the *Manduca Sexta* wing experiment, the frequency values are different by approximately a factor of two. There are several possible reasons why this deviation might exist: low resolution during component dimensioning, inadequate characterization of wing camber, and poor estimation of material properties. Each of these possibilities is explored below.

4.5.1. Component Dimensioning

The dimensions of the vein and membrane structures were obtained via computed tomography (CT) measurements. During this process it was observed that the vein dimensions (and to a lesser extent the membrane thickness) are a function of span. As the cross-section location moves from root to tip the veins taper, and the low resolution of the CT imager prohibits accurate measurement. Figure 71 compares images of the first three veins (leading edge is to the left) at the wing root, and approximately the half-span location (20 mm from the root). Due to the change in vein dimensions, the differences in image quality are striking. Gone from the half-span image is the clear inner-diameter, and the separation of the first two veins is indistinguishable.

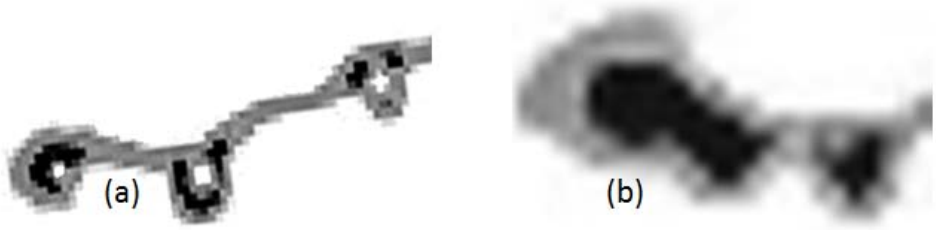

Figure 71: Comparison of first three veins at the wing root (a) and 20 mm (approximately half-span) from the root (b). In both cases, the leading edge is to the image left.

Figure 70 (b) highlights the effect of decreasing the vein diameter at constant image resolution: the relative importance of a single pixel is dramatically elevated. The pixel size is the limiting value of precision in digital image measurement, thus attempting to dimension structures with length scales of the same order of magnitude as the pixel size greatly increases the probability of measurement errors. The trend observed in Figure 70 continues as the cross-section location advances toward the tip. As the veins taper, they become less visible, and finally appear to blend into the membrane prior to their terminal locations.

The effects of varying vein dimensions on frequency content were studied in Chapter III. These parametric studies demonstrated that all modes are strongly affected by even small changes in vein diameter. As discussed in Chapter III, the first two modes are linear functions of vein thickness, while the third mode can be approximated by a polynomial that changes rapidly with diameter variation. A notable result from this parametric study is that the frequency separation between the first two modes appears fixed, regardless of vein diameter.

Comparing the results of the vein thickness (diameter) studies to the results of the finite element model of the *Manduca Sexta* wing suggests the outer diameter of the veins may have been overestimated. The higher-quality CT images near the wing root reveal that the veins are surrounded by a coating of membrane tissue. As the cross-section location moves from root to

tip, the relative thickness of the membrane coating increases due to a corresponding decrease in vein thickness.

It is likely that low CT image quality resulted in measuring the total diameter of what appeared to be the vein structure, instead of dimensioning only the vein and excluding the surrounding membrane (see Figure 72, below). Since the assumed value of Young's modulus of the veins (beams) was more than twice that of the membrane tissue (shells), measuring the *total* diameter surrounding the vein would result in a significant stiffening effect[29]. Conversely, because the veins and membrane are assumed to be of the same density, over-measuring the vein diameter would not increase the mass of the model – making measurement errors more difficult to detect. Thus, if a more accurate model is to be produced, a geometry measurement technique that offers higher resolution than the CT imager is necessary.

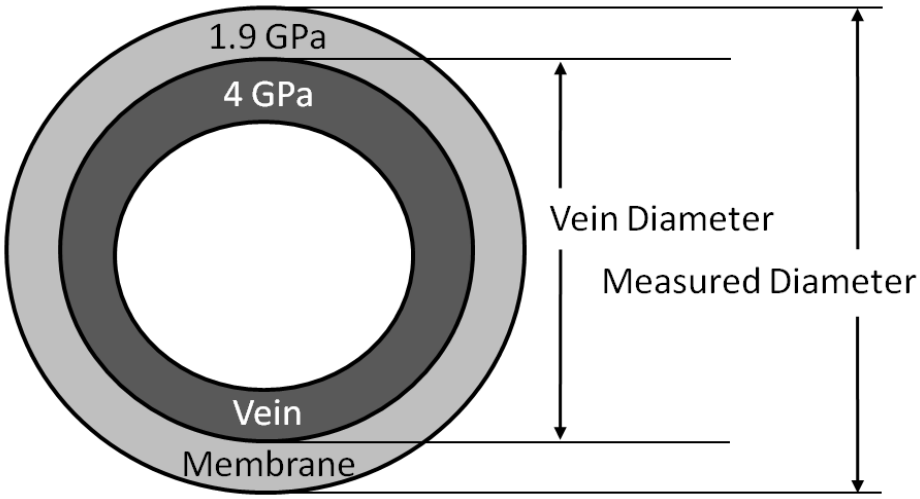

Figure 72: Schematic of membrane tissue surrounding the vein. Low CT resolution results in measuring the outer-diameter of both structures, instead of the vein only.

[29] This extent to which this over-dimensioning of vein diameter affects frequency results increases with the number of poorly-dimensioned veins. If the CT resolution were such that only a few vein segments had questionable dimensions, this effect might be negligible; this is not the case here.

4.5.2. Modeling Camber

Camber is an important feature of many wings, and the *Manduca Sexta* forewing is no exception. While often examined for reasons relating to fluid dynamics, the finite element results of Chapter III demonstrate that camber also has an important role in structural dynamics. Adding curvature to the *Manduca Sexta* wing adds stiffness, which in turn increases its natural frequencies. The approach taken during the finite element modeling process was to model the wing with a shell of constant radius and thickness. The selected camber was an average value based on CT measurements, and was measured using the NACA wing standard: the maximum distance between the chord line and the mean camber line is the camber value.

The curvature of a *Manduca Sexta* wing is far more complex than that of wings typical of man-made designs. Instead of the smooth wing surface of constant concavity seen in most commercial wing designs, the *Manduca Sexta* wing is of positive concavity near the leading edge, and negative concavity over the majority of the wing surface, as shown in Figure 19. Additionally, the camber is a function of span in the *Manduca Sexta* wing. Future modeling efforts should include this geometric sophistication if high-frequency modes are to be matched.

4.5.3. Material Properties

No material properties for the *Manduca Sexta* (or monarch butterfly, a similar species of the order *Lepidoptera*) are currently published, leaving one forced to estimate Young's modulus, Poisson's ratio, and density. As a result, the material properties used in the finite element model were based on those of the *Tibicen Canicularis* (cicada), as reported by Mengesha, Vallance, Barraja and Mittal. The cicada is of the order *Hemiptera*, a class of species observed to have stiff, semi-rigid wings; conversely, the *Manduca Sexta* (hawkmoth) is of the order *Lepidoptera*, and is known to have more flexible wings than *Hemipterae* [25]. Based on this knowledge, the

assumption that the Young's modulus of the *Manduca Sexta* wing components is likely the reverse of the *Tibicen Canicularis* was made.

Stiffness is a function of Young's modulus, geometry, and mass-density. While the mass of the finite element model was representative of what one might expect from a typical *Manduca Sexta* wing, it is possible that the agreement with the first two experimental modes was the result of the non-uniqueness of the stiffness value. In other words, the vein and membrane densities of the hawkmoth might be different than those of the cicada. If this is the case, assuming the same values as the cicada forced the moduli of elasticity to also reflect the values reported in Ref. [25]. Thus, it may be said that the ratio of Young's modulus to mass density, E/μ, is an important characteristic in the frequency response of the *Manduca Sexta* forewing. While the model produces good results for the first two modes, further investigation into the material properties is required to determine whether the values of E and μ are correct, or whether their ratio was arbitrarily satisfied.

The fact that the natural frequencies of the finite element model agree with the experimental results only in the first two modes likely indicates some total stiffness error in the model. Indeed, a fundamental concept in vibration theory is the effect of density and stiffness on frequency. A more accurate finite element model of the *Manduca Sexta* will likely require one to obtain material properties for the hawkmoth.

4.6. Modeshape Stresses

It is important to quantify the stresses the *Manduca Sexta* wing undergoes during operation. Although the magnitude of velocity and displacement at the modes may be greater than typically experienced in normal operation, the wing is evidently capable of sustaining such large oscillations. From a design life and fatigue analysis standpoint, a stress analysis of the

observed operational deflection shapes will likely play an important role in future MAV design. As discussed in the preceding sections, the final finite element model produced accurate results for the first two modes, but was unable to accurately predict the third natural frequency value. With this in mind, a von Mises stress analysis of the first two operational deflections shapes was conducted; the third modeshape was omitted from this analysis due to the lack of confidence in the results.

4.6.1. Scaling of Results

An important result from the experimental work detailed in Chapter II was the structural linearity observed in the *Manduca Sexta* wing. By definition of a linear system, the *Manduca Sexta* wing satisfies additivity and homogeneity of response to an input. The modeshapes in Abaqus are normalized to report some relative value of displacement at the nodes for a mode of vibration, however this value is different than the displacement reported by the Polytec scanning laser vibrometer. Although a modeshape is magnitude independent in its mathematical formulation, the *Manduca Sexta* forewing was underwent oscillations of a known magnitude. By comparing the wing deflections recorded during the experimental phase to the relative displacements predicted by Abaqus, one can determine what stresses were present in the wing at the time of its vibration.

In order to correlate the analytical and experimental displacements (and stresses), a proportional scaling factor, λ, must be developed. By the property of homogeneity, this scaling factor will serve as a coefficient to correlate stresses reported in Abaqus to those experienced in the wing. This scaling method will only be used for analyzing stress in the first two modes where the frequency results of the finite element model and the experimental wing are close.

Since the third mode is not adequately represented in the finite element model, it will be excluded from stress analysis using the scaling factor, λ.

Invoking the property of superposition, the scaling factor, λ, is simply the ratio of the wing tip displacements from the Polytec output and Abaqus model:

$$\lambda = \frac{\delta_{PSV}}{\delta_{Abq}} \tag{7}$$

where δ_{PSV} is the wing tip displacement measured by the Polytec scanning laser vibrometer, and δ_{Abq} is the wing tip displacement reported by Abaqus. Using Eq. (7), scaling factors for the first bending mode, λ_1, and for the torsional mode, λ_2, are computed.

The tip displacement in the first mode reported by the Polytech scanning vibrometer (PSV) software was 27.29 x10^{-6} meters, while Abaqus reported a first mode displacement of 3.09 x10^{-3} meters. Inserting these values into Eq. (7),

$$\lambda_1 = \frac{27.29\ \text{x}10^{-6}\ \text{m}}{3.09\ \text{x}10^{-3}\ \text{m}}$$
$$\lambda_1 = 8.92\ \text{x}10^{-3} \tag{8}$$

Similarly, Abaqus reported the tip displacement in the second mode as 1.98 x10^{-3} meters, while the laser vibrometer reported a second mode displacement of 3.32 x10^{-6} meters. Substituting these values into Eq. (7) gives,

$$\lambda_2 = \frac{3.32\ \text{x}10^{-6}\ \text{m}}{1.98\ \text{x}10^{-3}\ \text{m}}$$
$$\lambda_2 = 1.68\ \text{x}10^{-3} \tag{9}$$

With the scaling factors (λ_1 and λ_2) obtained, the model stress values can be related to the stresses in the *Manduca Sexta* wing.

4.6.2. Wing Stress Analysis – First Bending Mode

A von Mises stress analysis of the first operational deflection shape (first bending, 84.6 Hz) was conducted using the finite element model described previously[30]. Since the proportional limit of the materials used in the wing are unknown, this analysis assumes purely elastic behavior.

The maximum (scaled by λ_1) von Mises stress is 258.4 KPa, and occurs at the trailing edge near the clamp. The scaled minimum stress is 567 Pa (0.08 psi – essentially zero stress), and occurs at the wing tip. Stress contour plots given in Abaqus indicate that the veins appear to be the primary load-bearing members, and have an average stress of approximately three orders of magnitude greater than that of the membrane. The most striking feature is the nearly uniform low stress in the membrane; only portions near the clamped boundary – and a small section at approximately one-third of the wing span – are significant stress concentrations visible. Likewise, it is apparent that the stress in the veins is the highest in approximately the first third of the span. It was observed that vein intersections in which new veins are created tend to increase the von Mises stress to approximately 65 KPa (scaled value), while intersections that combine existing veins tend to have little effect on stress concentrations.

4.6.3. Wing Stress Analysis – Torsional Mode

The stress analysis was repeated for the second (torsional) mode, this time scaling the results by the torsional factor, λ_2. The maximum von Mises stress observed in the torsional eigenvector is 28.91 KPa, and occurs in the leading edge vein at approximately 80% of the span. The minimum stress is located in the membrane near the leading edge and was found to be 277 Pa – approximately half that of the first mode. In general, the second modeshape causes a lower

[30] Contour plots of this analysis are given in Appendix E – Stress Plots.

average state of stress than the first mode, with less variation between the minimum and maximum stress values.

A more even stress distribution is present in the torsional mode than in the first bending mode, but many of the trends are similar. The maximum stresses are located near the clamp and at vein intersections, and generally decrease with span. In a noticeable departure from this trend, the thickening of the first vein slightly beyond the half-span results in stress reduction; this reduction appears to also cause a local stress reduction in the veins behind it. As the cross-section of the leading edge vein narrows near the tip, the stress increases to 24.88 KPa (scaled value), reflecting the large leading-edge displacement in the torsional mode. Unlike the behavior observed in the first mode, the vein oriented in the chordwise direction plays a dramatic stiffening role in the torsional mode. Indeed, its stresses are much higher than observed in the bending mode, with an average von Mises stress of 9.22 KPa.

V. Conclusions and Recommendations

The focus of this research was to conduct a system identification of a *Manduca Sexta* forewing, and develop a finite element model capable of accurately predicting the observed modes. During this process, parametric studies were conducted examining the effects of vein diameter and camber on the natural frequencies of vibration. Convergence studies and a stress analysis was conducted by normalizing the displacement of the finite element model to that obtained by the laser vibrometer. The conclusions reached during each phase of these investigations are detailed below.

5.1. Analysis of Boundary Conditions

A foam-lined clamp was used to secure the *Manduca Sexta* wing during the experimental portion of the system identification. Before frequency extraction was conducted on the *Manduca Sexta* wing, a paper beam was placed inside the clamp and analyzed in vacuum (< 4 Torr) conditions. The ratio of modes, ω_2/ω_1 is 6.40 and ω_3/ω_2 is 2.813. The analytical solution for the modes of a prismatic, homogeneous, isotropic beam with a clamped boundary condition (cantilever) were developed in Chapter II, and deviated from the experimental values by 2.08% for ω_3/ω_2 and 0.45% for ω_3/ω_2. Thus, the foam-lined clamp used during the frequency analysis of the hawkmoth wing may be considered rigidly clamped.

5.2. Wing Preparation and CT

Wing selection and preparation were carefully controlled to ensure repeatability of results. Only healthy, adult, female *Manduca Sextae* were used. Before wing liberation, each hawkmoth was placed into a refrigerator (34°F) and cooled for 30 minutes to induce hypothermia. The moths were checked for responsiveness before wing liberation. Liberation

was accomplished using a scalpel, and the wings were carefully cut adjacent to the thorax. Once removed, the wings were placed into a foam-lined clamp for analysis.

Wing geometry and dimensions were measured using a computed tomography (CT) imager. The CT software created a digital, three-dimensional model using a series of X-Ray images. CT imaging lasted approximately 20 minutes, and the model was saved for later analysis. Vein dimensions, camber, and membrane thickness were measured, and the membrane was found to be of a generally constant 0.12 mm thickness. Significant estimation of vein diameter was necessary, due to the low resolution of the CT images. In order to create a model representative of the *Manduca Sexta* wing, it is recommended that an imaging technique of higher resolution than CT be used.

5.3. System Identification of a Manduca Sexta *Forewing*

A *Manduca Sexta* forewing was placed inside the foam-lined clamp described above, and secured to a flapping motor. The motor excited the wing only in the direction normal to the wing planform and at low voltage (0.2 V) to produce small displacements. A pseudo-random input was used from frequencies approaching zero to 1 kHz. The low voltage in the motor produced a maximum displacement of 27.29 μm at the tip during the first bending mode, and a corresponding maximum velocity of 282.7 μm/s; similarly, the tip displacement during the torsional mode was 3.32 μm, and the maximum tip velocity was 215.0 μm/s. Frequency values and modeshapes were recorded using a Polytec® scanning laser vibrometer. The first three natural frequencies of the wing in vacuum were 86 Hz, 106 Hz, and 155 Hz, with an error margin of ± 2 Hz at all modes; the corresponding modeshapes were first bending, torsion, and saddle, respectively.

Tests were conducted in air and vacuum to gage the extent of aeroelastic effects on the *Manduca Sexta* wing. Due to drying concerns, a wing cannot be used for air, vacuum, and CT experiments within the 3-hour freshness criterion set by Norris [32]. To circumvent this aging problem, a fresh wing was used for comparison of modes in air and vacuum. Vibration tests in air resulted in frequency values of 58.75 Hz, 75, Hz, and 95 Hz for the first three modes. Frequency testing in vacuum (< 4 Torr) resulted in the following first three modes: 80 Hz, 98 Hz, and 118 Hz. The conclusion from these experiments is that aeroelasticity plays some role in the frequency response of a *Manduca Sexta* wing; contributions from air decrease first three modes by an average of 23.17%.

5.4. Linearity of Wing Structure

The spectral coherence from the *Manduca Sexta* system identification is plotted in Figure 20. Only the first three modes of the forewing were considered during this investigation, the lowest of which occurred at 86 Hz, while the third mode appeared at 155 Hz. The average coherence within the range of 30 Hz to 200 Hz was 0.983, with a standard deviation of 0.014. The high coherence value observed in the *Manduca Sexta* forewing indicates that the behavior of the wing structure is linear – that is, satisfies homogeneity and additivity – within the regime tested. This important result allows scaling of stress analyses using normalization factors, λ_1 and λ_2, corresponding to the ratios of the tip displacements observed in experiment to the first and second modes, respectively.

It should be noted that although a linear response was observed during low amplitude flapping, one cannot conclusively claim that the wing behaves linearly for all flapping conditions. Without additional experimentation, it is unknown whether the *Manduca Sexta* wingbeat produces nonlinear structural effects.

5.5. Inadequacy of Flat, Homogeneous Wings

A system identification of a paper wing of the same planform as a *Manduca Sexta* forewing was also conducted using a laser vibrometer. The first three modeshapes of the actual *Manduca Sexta* wing were first bending, torsion and saddle; the first four modeshapes of the paper wing were first bending, torsion, second bending, and saddle (with negative tip-deflection). The ratios of the *Manduca Sexta* wing modes in vacuum (< 4 Torr) were $\omega_2/\omega_1 = 1.23$ and $\omega_3/\omega_1 = 1.80$; the ratios of the paper wing modes (in vacuum) were $\omega_2/\omega_1 = 4.80$, and $\omega_3/\omega_1 = 8.10$. The inclusion of the spurious second-bending mode and the considerable differences in the frequency ratios highlight the inability for a flat, homogeneous, isotropic wing to characterize a hawkmoth wing. Based on these findings, it is strongly recommended that future researchers not conduct analogous *Manduca Sexta* (or any *Lepidoptera*) wing studies using flat, one-piece wings.

5.6. Modeling with Membrane Elements

Finite element studies were conducted to examine what type of element best describes the membrane tissue found in the *Manduca Sexta* wing. A model consisting of three beams separated by two membrane sections was used. The elements selected were the eight-noded, quadratic, quadrilateral membrane (M3D8), and the four-noded linear quadrilateral membrane (M3D4). Since membrane elements only carry in-plane stresses, kinking was observed at the membrane-beam interaction for all mesh sizes. Convergence studies were conducted showing that even with nearly one million membrane elements, the discontinuity of slope at the beams could not be resolved. The conclusion from these studies is that the membrane tissue in the *Manduca Sexta* contains bending and transverse shear components not carried by membrane elements.

5.7. Modeling with Shell Elements

The model used in the investigation of membrane elements was modified to consist of three beams separated by two shell sections. Based on the documentation supplied with Abaqus, the four-noded, doubly-curved, reduced-integration, shells (S4R) of the Koiter-Sanders formulation were selected. The results of even a simple model (5,814 degrees of freedom) were remarkably better than those observed using membrane elements. The modeshapes contained no discontinuities of slope at the beams. As a result of these studies, shell elements were selected for future modeling of the *Manduca Sexta* wing.

5.8. Effects of Camber on Natural Frequency

A homogeneous, isotropic shell model of the same planform as the *Manduca Sexta* wing was constructed in Abaqus. A parametric study of the effect of camber on natural frequency was conducted. Camber values between 0 %c and 13 %c (15^o angle between the leading edge and maximum mean camber line location) were considered, using a converged mesh of 300 elements (954 nodes, 5724 degrees of freedom). All modes except the torsional mode were observed to be strongly dependent on camber-induced stiffness. The spurious second-bending mode observed in the flat paper wing disappeared at a wing camber of 4.5 %c, at which point the saddle mode became the third mode.

5.9. Effects of Vein Diameter on Natural Frequency

A parametric study of the effects of vein thickness on natural frequency was conducted using a flat wing of the same planform as the *Manduca Sexta* forewing. Ten veins were modeled as prismatic beams using average cross-sectional data obtained from CT images. A vein thickness factor was applied as a scaling coefficient for all veins and the first four modes were

recorded. Scaling factors between 0.5 and 2 were used, and data were collected at semi regular intervals with a thickness factor step size of approximately 0.4. At a vein thickness factor of 1.2 (*i.e.*, the veins cross sections were 20% larger than observed from CT images), the spurious second-bending mode disappeared, and the saddle mode became the third mode.

All veins were strongly correlated to vein thickness. The first bending mode and torsional mode increased at approximately the same rate with vein thickness, though the saddle mode diverged from the first bending and torsion as vein diameter increased. The second bending mode changed by the greatest frequency value (129 Hz) in the domain of the investigation, while the first bending mode increased by the greatest factor (4.42). There are two conclusions from this study: first, adequately modeling the natural frequencies of a *Manduca Sexta* wing is strongly dependant on obtaining correct vein dimensions; second, the frequency difference between the first bending and torsional modes is relatively fixed, though the frequency difference between the first and third modes diverges rapidly with increasing vein diameter.

5.10. Material Property Considerations

The material properties of the *Manduca Sexta* are unknown as of this document's publication. Published values for the *Tibicen Canicularis* (cicada) [25] and preliminary findings by O'Hara [31] place the material properties of the vein and membrane structures between 1.9–5 GPa. Mengesha, Vallance, Barraja and Mittal report the veins and membrane having Young's moduli of 1.90 GPa and 3.70 GPa, respectively [25]. O'Hara's research indicates that the hawkmoth's material values may be the reverse of the cicada's, with a membrane modulus of 2 GPa [31]. Although the values reported in Refs. [25] and [31] vary by a factor of approximately two, they are within the same order of magnitude.

The vein diameter studies of Chapter III indicate that varying Young's modulus within the regime of 2-5 GPa plays a relatively small role in changing the natural frequencies of the *Manduca Sexta* wing. Examining the vein diameter plots at a vein thickness factor of one gives the following frequency values using the material properties from the cicada wing: $\omega_1 = 33$ Hz, $\omega_2 = 89$ Hz, $\omega_3 = 206$ Hz, and $\omega_4 = 297$ Hz. In comparison, reversing the moduli of the veins and membranes gives the following frequency values: $\omega_1 = 41$ Hz, $\omega_2 = 91$ Hz, $\omega_3 = 226$ Hz, and $\omega_4 = 308$ Hz. While these changes are significant in the first mode (a change of 19.5%), modulus variation nevertheless has a less dramatic effect than altering camber or vein diameter by a similar magnitude (a factor of two, in this case).

Density values for the *Manduca Sexta* are also unknown. Unlike the elastic moduli, the mass densities of the veins and membrane have yet to be evaluated – even preliminarily. The density values used during the modeling process were taken from the cicada (2.30 g/cm^3) and produced a model with mass representative of a *Manduca Sexta* (0.04 g). During this analysis, an inherent assumption is that the densities of the membrane and veins are equal; this assumption may be the root cause of relative invariance of frequency with changing Young's moduli. Borrowing from beam theory, the ratio of elastic modulus to mass density, E/μ, is the only influence of material property values on natural frequency. The others – length and moment of inertia – are set by geometry. In the case of the *Manduca Sexta*, it may be that the ratio of E/μ plays a critical role that is understated by the equal vein and membrane density assumption. In short, before a more accurate model can be produced, Young's modulus and density values must be investigated further. Without doing so, it is impossible to verify the conclusions of the material property influence on frequency given in Chapter III, because they are based upon unvalidated underlying assumptions regarding density.

5.11. Modeling and Model Limitations

A finite element model of a *Manduca Sexta* wing was produced to accurately predict the first two natural frequencies and mode shapes as seen in the experimental data. The third mode shape is qualitatively similar to that observed in the *Manduca Sexta* wing, though the frequency values differ by 102%. The laser vibrometry experiments predicted modes in the *Manduca Sexta* wing at 86 Hz, 106 Hz, and 155 Hz, with an error margin of ± 2 Hz for each mode. The finite element model gives the first bending mode at 84.6 Hz, a torsional mode at 106.1 Hz, and a saddle mode at 317.7 Hz. These values were obtained using a converged model with a total of 80,633 quadratic beam and general-purpose shell elements, comprised of 83,664 nodes. The agreement of the first two natural frequencies of the experimental wing and finite element model suggest that the model is useful for characterizing frequencies up to and including the second mode only. Further research is required to determine the importance of the experimental and numerical disagreement seen in the third and higher natural frequencies.

Comparing the model to the parametric studies of camber and vein diameter versus natural frequency suggest more precise modeling is required. While it is possible to model a more accurate distribution of camber using the CT images, the resolution is not sufficient to accurately measure vein profiles. It is strongly recommended that higher resolution imaging techniques be investigated if accuracy beyond the second mode is required.

5.12. Stress Analysis of the First Bending Mode

A stress analysis was conducted on the first bending mode (84.6 Hz) of the finite element model. A scaling factor, λ_1, was developed to normalize the displacement results reported in Abaqus to those of the wing examined using a laser vibrometer. The scaling factor, λ_1, was defined as the ratio of the tip displacement recorded experimentally to the tip displacement

reported by Abaqus: $\lambda_1 = \delta_{PSV}/\delta_{Abq}$, and was found to be 8.92 x10^{-3} for the first bending mode. Since the *Manduca Sexta* wing is behaves linearly, the scaling factor approach is valid.

The maximum stress in the first bending mode occurs in the trailing edge at the clamped boundary. The maximum (λ-scaled output) von Mises stress experienced in the first mode was 258.4 KPa. The minimum von Mises stress was computed to be 567 Pa, and occurred at the wing tip. Notable was the consistently low stress observed in the membrane, while the veins carried the bulk of the stresses in this mode. Vein (beam) stress was observed to decrease with span in all members, with stress concentrations arising at the vein intersections. The cyclic operation and high stress concentrations near the wing root suggest fatigue failure may be a design challenge in future MAVs; appropriate materials and geometry must be carefully selected to secure the wing-body interface.

5.13. Stress Analysis of the Torsional Mode

Using the approach described above to determine the scaling factor, λ, a stress analysis of the torsional mode was conducted. The scaling factor corresponding to the torsional mode, λ_2, was computed to be 1.68 x 10^{-3}. The maximum (scaled) von Mises stress in the torsional eigenvector was 28.91 KPa, located in the leading edge at approximately 80% of the span. The minimum von Mises stress was 277 Pa, located in the membrane just aft of the leading edge, near the ¾ span location. The stress variation in the torsional mode was significantly less than that of the first bending mode. While the veins still carried the majority of the load, a far greater stress distribution was found in the membrane. Stress was observed to be a function of span, with concentrations in the chordwise vein not observed in the previous mode.

5.14. Recommendations for Future Work

With the above conclusions in mind, it is recommended that future researchers work to reduce the number of model approximations and conduct further parametric analyses. From an experimental perspective, future work should focus on obtaining high-fidelity geometry measurements. Second, the material properties of the *Manduca Sexta* wing components should be investigated. Third, in light of the observed frequency shift when comparing air and vacuum measurements, one should undertake a comprehensive, noninvasive experimental study of the aeroelastic effects on the *Manduca Sexta* wing.

Focusing on possible numerical research, a model that represents camber as a function of wing coordinates should be created, with special attention paid to the bi-camber observed using the CT imager. Finally, to aid future MAV designers, a parametric study of the wing structure and its components should be conducted. At this point, it is evident that the venation observed in the hawkmoth wing has a dramatic effect on frequency response; it is unclear, however, whether the specific venation pattern is optimized for flight or circulation – or neither.

Appendix A – CoordGen

The following software uses input files generated in Abaqus to write text files containing the three-dimensional coordinates of geometric sets. These sets are created by the user in Abaqus during the modeling process. The purpose of CoordGen is to address Abaqus's inability to internally sketch wire beams in three dimensions. CoordGen is a program written in Python 2.6, and feeds coordinates for splines into SolidWorks; these splines can be imported back into Abaqus as wire beams in a common format (IGES, STEP, etc.). With permission, the code is reprinted below.

```
# Copyright (c) 2010 Jason R. Sims, jsims02@gmail.com

# Permission is hereby granted, free of charge, to any person
# obtaining a copy of this software and associated documentation
# files (the "Software"), to deal in the Software without
# restriction, including without limitation the rights to use,
# copy, modify, merge, publish, distribute, sublicense, and/or sell
# copies of the Software, and to permit persons to whom the
# Software is furnished to do so, subject to the following
# conditions:

# The above copyright notice and this permission notice shall be
# included in all copies or substantial portions of the Software.

# THE SOFTWARE IS PROVIDED "AS IS", WITHOUT WARRANTY OF ANY KIND,
# EXPRESS OR IMPLIED, INCLUDING BUT NOT LIMITED TO THE WARRANTIES
# OF MERCHANTABILITY, FITNESS FOR A PARTICULAR PURPOSE AND
# NONINFRINGEMENT. IN NO EVENT SHALL THE AUTHORS OR COPYRIGHT
# HOLDERS BE LIABLE FOR ANY CLAIM, DAMAGES OR OTHER LIABILITY,
# WHETHER IN AN ACTION OF CONTRACT, TORT OR OTHERWISE, ARISING
# FROM, OUT OF OR IN CONNECTION WITH THE SOFTWARE OR THE USE OR
# OTHER DEALINGS IN THE SOFTWARE.


# Following are objects and their properties:
#     Instance
#     --------
#         * name - string
#         * nodes - list of Nodes
#         * nsets - list of Nsets
#
```

```
#     Node
#     ----
#         * x - x-coord (float)
#         * y - float
#         * z - float
#         * id - id in Node list (int)
#
#     Nset
#     ----
#         * name - string
#         * instance_name - string
#         * nodes - list of ints representing Node ids

from optparse import OptionParser


class Context(object):
    is_done = False

    def add_line(self, line):
        if self.__class__.end_pred(line):
            self.is_done = True
        else:
            self._add_line(line)

class Instance(Context):
    def __init__(self, line):
        Context.__init__(self)
        self.nodes = list()
        self.nsets = list()

        self._parsing_nodes = False

        self._parse_name(line)

    def _add_line(self, line):
        if self._parsing_nodes:
            if Node.end_pred(line):
                self._parsing_nodes = False
            else:
                self.nodes.append(Node(line))
        elif Node.start_pred(line):
            self._parsing_nodes = True

    def _parse_name(self, line):
        for res in filter(lambda l: "name" in l, line.split(",")):
            self.name = res.strip().split("=")[1]

    @classmethod
    def start_pred(cls, line):
        return "*Instance" in line
```

```
    @classmethod
    def end_pred(self, line):
        return "*End Instance" in line

class Node:
    def __init__(self, line):
        self.id,  self.x,  self.y,  self.z  =  [float(s)  for  s  in
line.split(",")]

    @classmethod
    def start_pred(cls, line):
        return "*Node" in line

    @classmethod
    def end_pred(self, line):
        return "*" in line

class Nset(Context):
    def __init__(self, line):
        Context.__init__(self)
        self.nodes = list()
        self._parse_name(line)

    def _add_line(self, line):
        self.nodes += [int(n) for n in line.split(",")]

    def _parse_name(self, line):
        for res in filter(lambda l: "nset" in l, line.split(",")):
            self.name = res.strip().split("=")[1]
        for res in filter(lambda l: "instance" in l, line.split(",")):
            self.instance_name = res.strip().split("=")[1]

    @classmethod
    def start_pred(cls, line):
        return "*Nset" in line

    @classmethod
    def end_pred(self, line):
        return "*" in line


def map_nsets_to_instances(elts):
    def partition((insts, nsets), elt):
        if type(elt) is Instance:
            insts.append(elt)
        else:
            nsets.append(elt)
        return insts, nsets

    insts, nsets = reduce(partition, elts, [[], []])
    for nset in nsets:
        for inst in insts:
```

```
            if nset.instance_name == inst.name:
                inst.nsets.append(nset)
    return insts

def gen_lines(file):
    fd = open(file, "r")
    for line in fd:
        yield line
    fd.close()

def process_file(file):
    def do_process((context, acc), line):
        if context is not None:
            context.add_line(line)
            if context.is_done:
                return (None, acc)
            return (context, acc)
        for kls in [Instance, Nset]:
            if kls.start_pred(line):
                context = kls(line)
                acc.append(context)
        return (context, acc)

    return  map_nsets_to_instances(reduce(do_process,  gen_lines(file),
(None,

list()))[1])


def write_instance(inst):
    for nset in inst.nsets:
        fd = open("%s.txt" % nset.name, "w")
        for n in nset.nodes:
            node = inst.nodes[n-1]
            fd.write("%s %s %s\n" % (node.x, node.y, node.z))
        fd.close()

if __name__ == "__main__":
    parser = OptionParser(usage="coordgen.py [files]")
    (options, args) = parser.parse_args()

    map(write_instance, sum(map(process_file, args), []))
```

Appendix B – CT Images

These images are supplemental to those supplied in Chapter II. Figure 73 shows the unaltered version of Figure 19. Although visible at high-zoom levels, the inner portions of the leading and trailing edge veins are difficult to distinguish. Unmagnified versions of this image do not adequately reproduce the grey discoloration present to the CT operator. As a result, the areas inside the inner diameters were converted to white, with a 3% coloration threshold. In other words, if the color of the pixels adjacent to the inner portion was more than 3% different than the grey inside the vein, it kept its original coloring. By applying this color change with a small threshold, the reader is better able to see the circulatory, inside portion of the vein. Finally, the noise at the left of the image was removed in Figure 19.

Figure 73: Unaltered version of Figure 19.

The next figure shows the exact locations of the cross-sectional measurements described in Chapter II. The solid, vertical lines represent the digital "slices" taken to characterize the geometry of the wing. Finally, Figure 75 shows the stereo-lithographic planform view of the *Manduca Sexta* forewing, as exported from the CT.

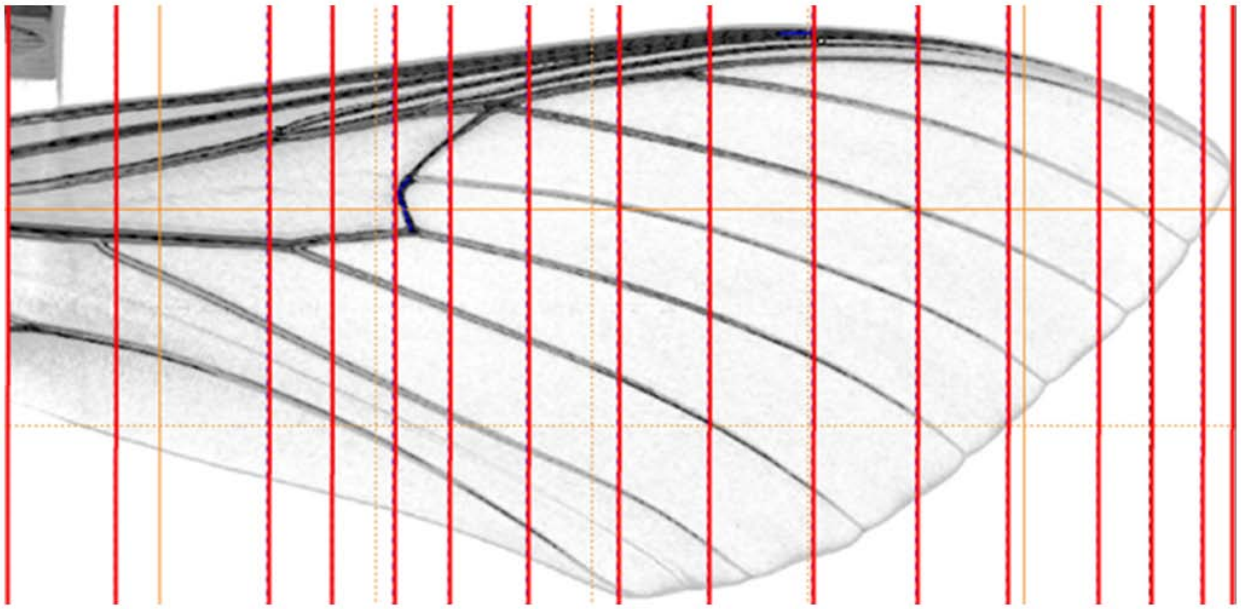

Figure 74: Location of cross-sectional measurements, denoted by vertical lines.

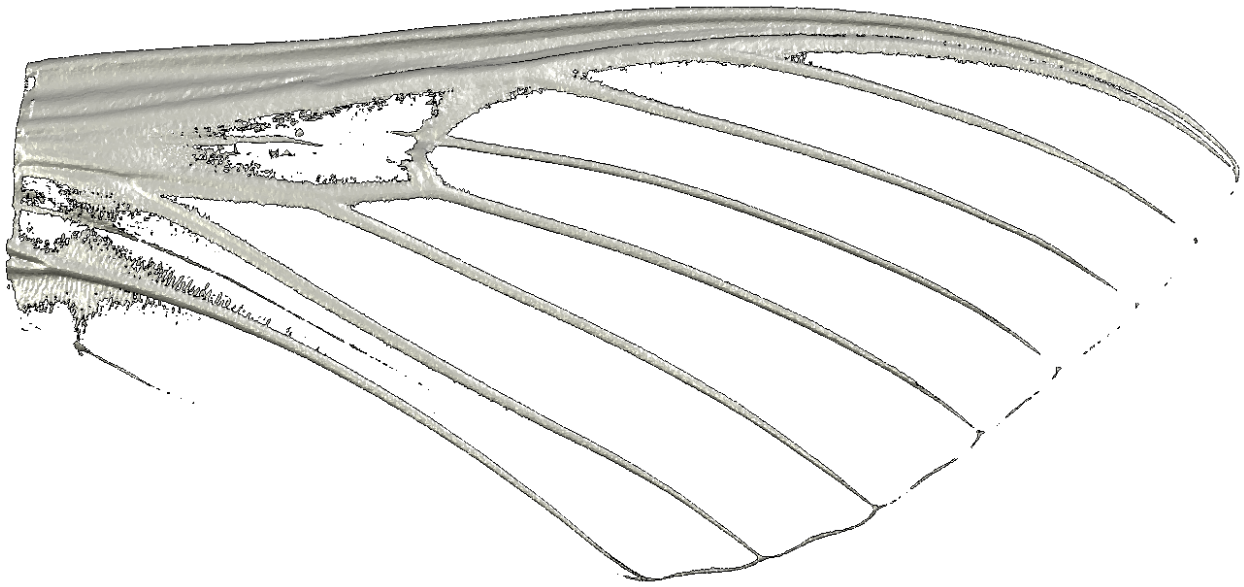

Figure 75: Stereo-lithographic planform view of the *Manduca Sexta* wing.

Appendix C – Higher Order Modes

The following images show the modeshapes of the hawkmoth's fourth and fifth modes. These modes were collected in the laboratory, but omitted from analysis. Since every continuous structure has an infinite number of natural frequencies and associated mode shapes, one is forced to narrow an analysis to a set number of modes. In this case, the first three modes were deemed sufficient for a preliminary finite element comparison.

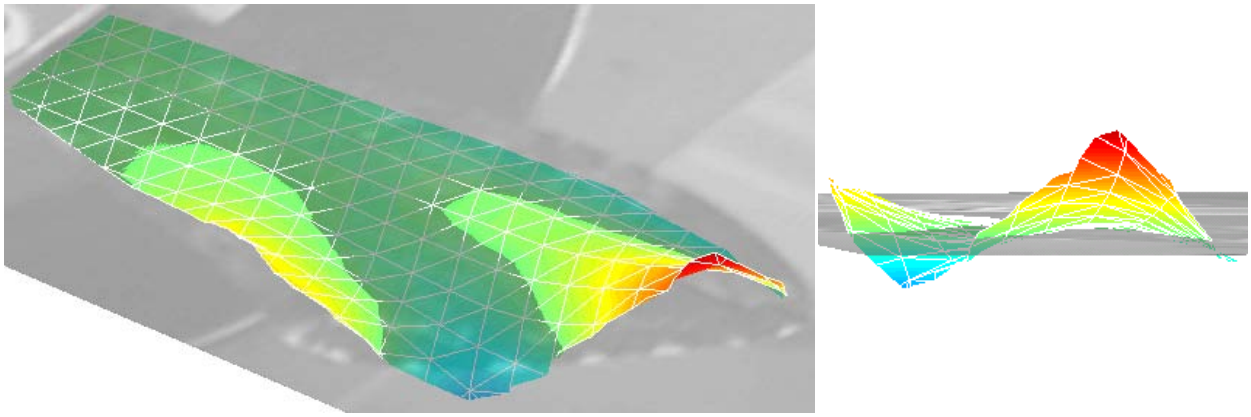

(a) (b)

Figure 76: Fourth modeshape (187 Hz) of a *Manduca Sexta* wing, shown from an isometric view (a) and a tip view (b).

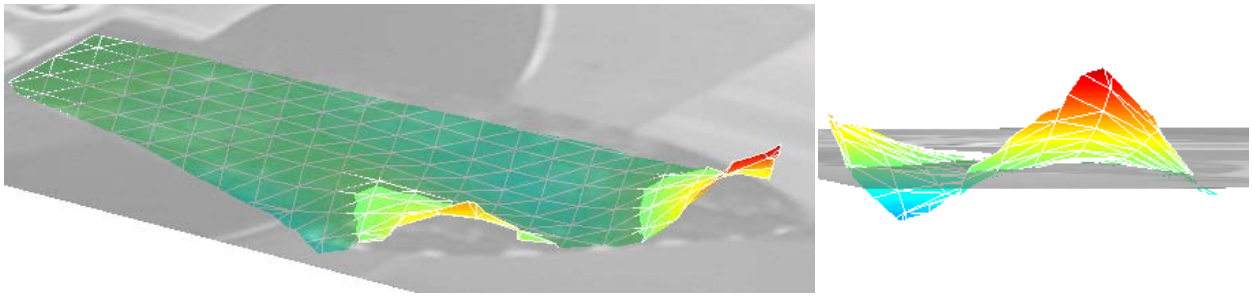

(a) (b)

Figure 77: Fifth modeshape (231 Hz) of a *Manduca Sexta* wing, shown from an isometric view (a) and a tip view (b).

The following figure shows the fifth modeshape of the paper wing tested for comparison to the hawk moth. This mode has the same qualitative characteristics as the *Manduca Sexta*

saddle mode, with the exception of the circular, plate-like vibration in the center (see image (a) in Figure 78), below.

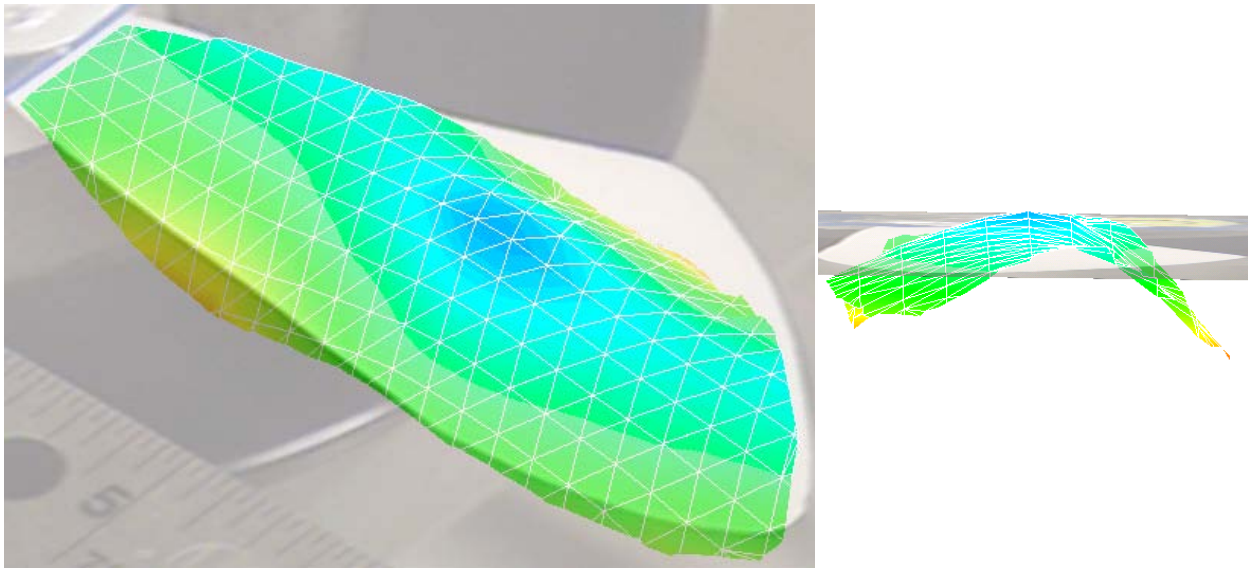

(a) (b)

Figure 78: Fifth modeshape (692 Hz) of a paper *Manduca Sexta* wing, shown from an isometric view (a) and a tip view (b).

Appendix D – Wing Camber

Wing camber is defined as the maximum distance between the mean camber line and the chord line [41]. Typically, the camber is expressed as a percentage of chord (%c) – the linear distance between the leading and trailing edges. The mean camber line (technically a curve, though called a "line" by convention) is the collection of points that is half-way between the upper and lower surfaces of the wing – hence *mean* camber line). Figure 79 shows a side view of a conventional airfoil, with the mean camber line, chord line, thickness and camber labeled.

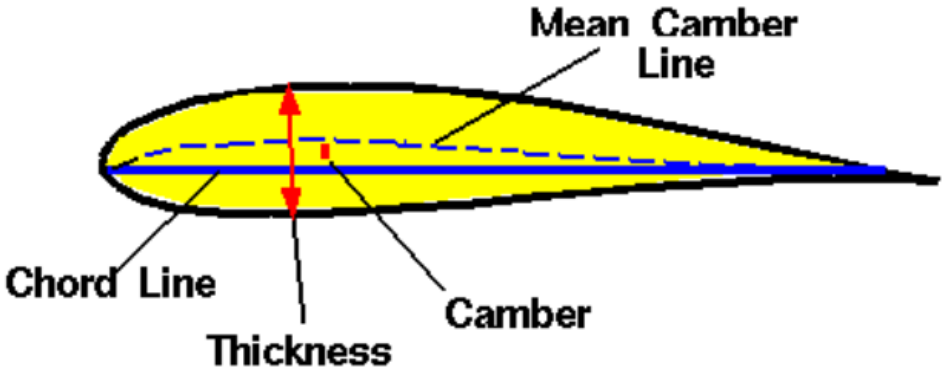

Figure 79: Wing geometry image, courtesy NASA Glenn Research Center.

The *Manduca Sexta* wing has a thin membrane structure, such that the mean camber line is essentially the midpoint of the membrane curvature. As discussed in Chapter IV, there is a difference between the camber modeled in the finite element studies, and the camber of the actual *Manduca Sexta* wing. The finite element model features a single shell of constant radius, to which beams are tied at the midpoint, as shown in Figure 80. The actual wing, however, features a double camber, with both positive and negative concavity, as shown in Figure 81.

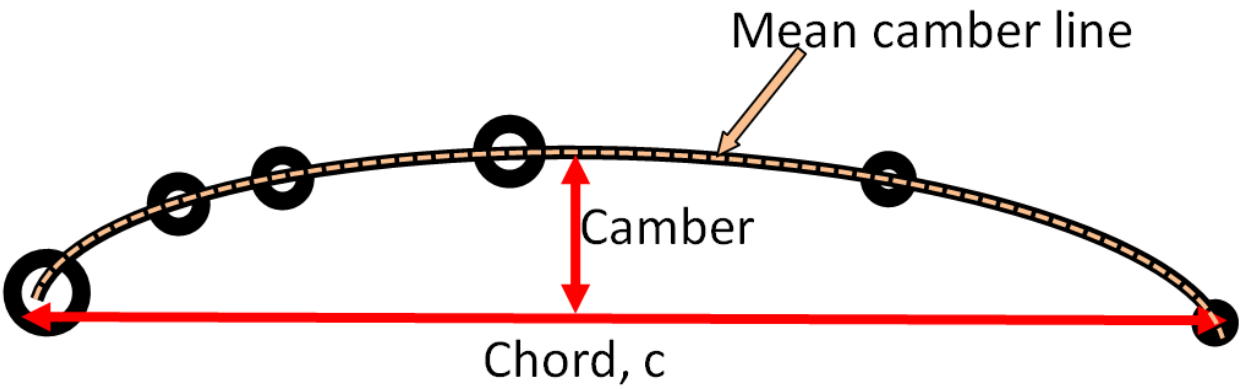

Figure 80: Schematic of modeled FE wing at the root.

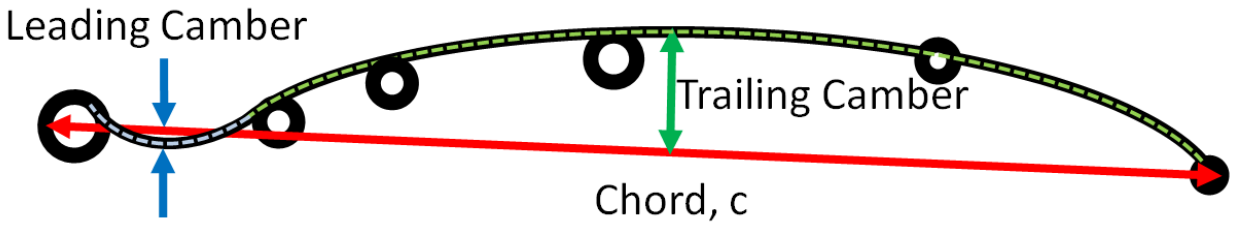

Figure 81: Schematic of a *Manduca Sexta* wing at the root.

Appendix E – Stress Plots

The images that follow are contour plots corresponding to the stress analyses of Chapter IV. Figure 82 shows the von Mises stress contour of the first bending mode. Figure 83 also shows the stress in the first bending mode, with the shells made transparent for easier viewing of the beams.

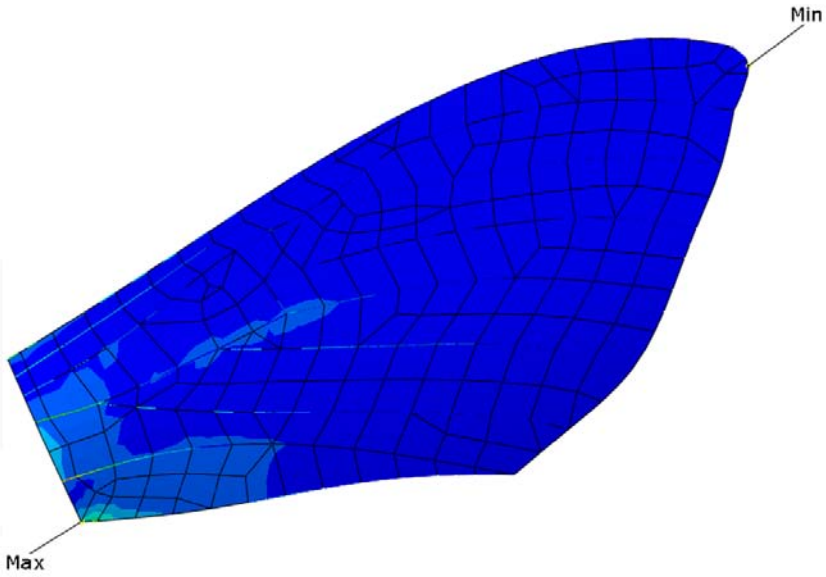

Figure 82: First mode von Mises stress contour for a finite element model of a *Manduca Sexta* forewing.

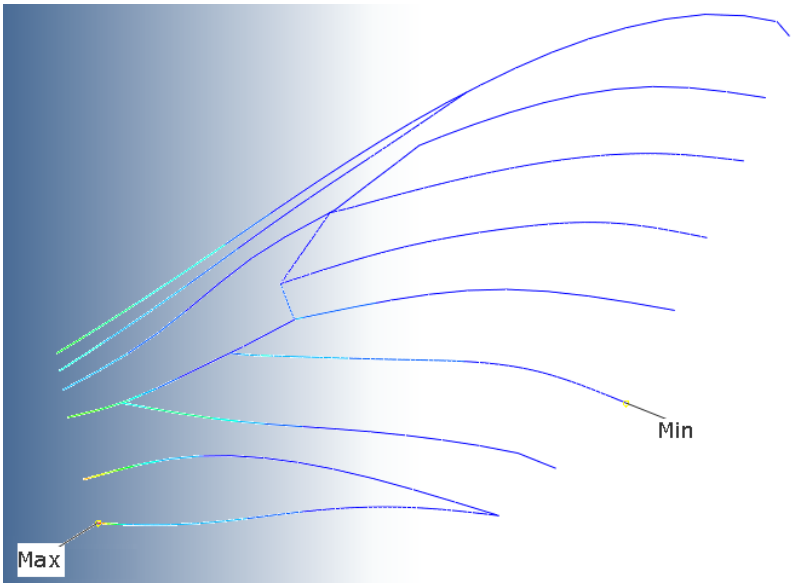

Figure 83: First mode stress in a finite element model showing *Manduca Sexta* wing veins.

Figure 84 and Figure 85 show the von Mises stress contour for the second mode (torsion). As before, the shells are present in Figure 85, but are transparent to better illustrate the stress distribution in the veins.

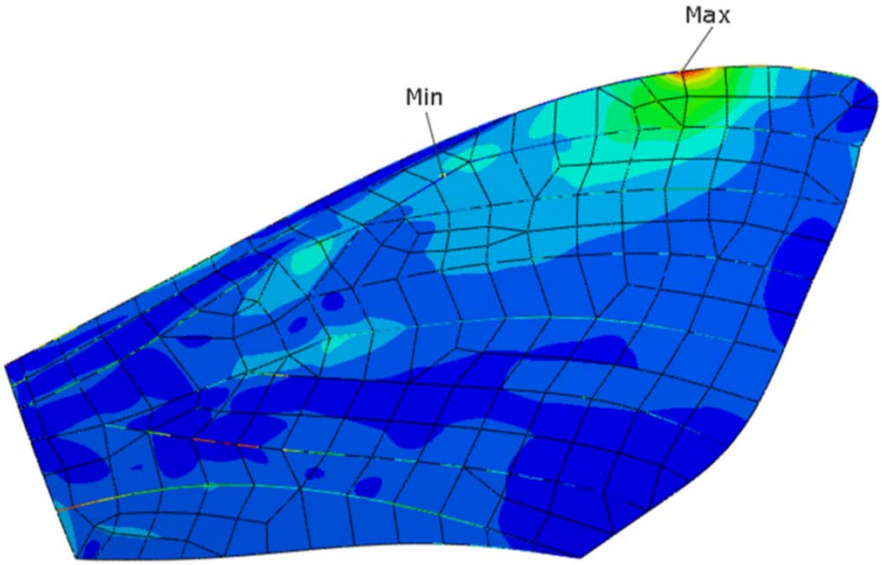

Figure 84: Second mode stress in a finite element model of a *Manduca Sexta* forewing.

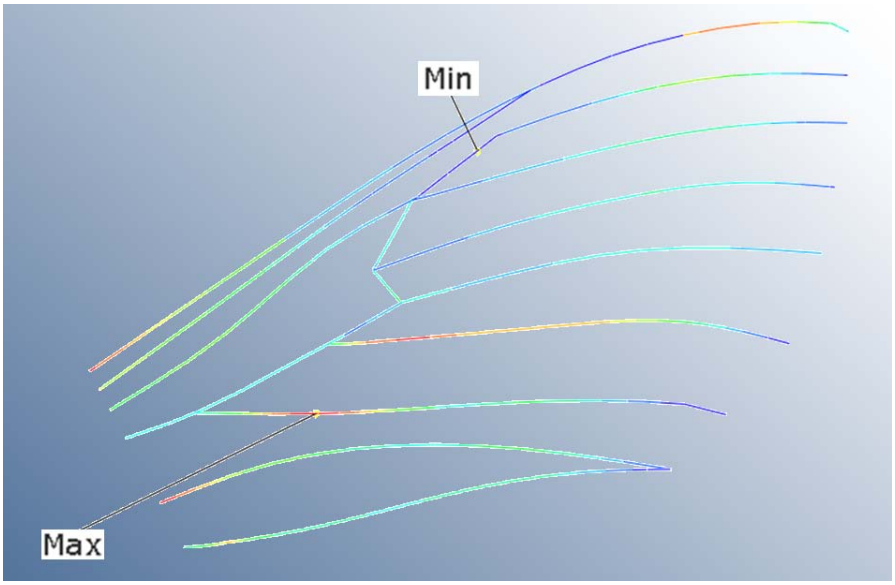

Figure 85: Second mode stress in a finite element model showing *Manduca Sexta* wing veins.

Bibliography

1. *Abaqus Theory Manual*, Ver. 6.8., Dassault Systèmes Simulia Corporation, 2008.

2. *Abaqus/CAE User's Manual*, Ver. 6.8., Dassault Systèmes Simulia Corporation, 2008.

3. "ATSC Digital Television Standard: Part 4 -MPEG-2 Video System Characteristics," Advanced Television Systems Committee, Inc., Document A/53, Part 4, 2009.

4. Betts, C. R., and Wootton, R. J., "Wing Shape and Flight Behaviour in Butterflies (Lepidoptera: Papilionoidea and Hesperioidea): a Preliminary Analysis," *Journal of Experimental Biology*, 1988, Vol. 138, pp. 217-288.

5. Bendat, J.S, and Piersol, A. G., Random Data: Analysis and Measurement Procedures, 2nd Ed., John Wiley & Sons, Inc., 1986.

6. Binden, J. A., *X-Wing Helicopter-Scout Attack Configuration,* Northrop Corporation, U.S. Patent 4711415, 1985.

7. Bjorkman, G. S., and Piotter, J. M., "Finite Element Mesh Considerations for Reduced Integration Elements," *Transactions*, SMiRT 19, No. J01/1, 2007.

8. Bunker, S. J., "Form, Flight Pattern and Performance in Butterflies (Lepidoptera: Papilionoidea and Hesperioidea). PhD Thesis, University of Exeter, 1993.

9. Chen, J. S., Chen, J. Y., and Chou, Y. F., "On the Natural Frequencies and Mode Shapes of Dragonfly Wings," *Journal of Sound and Vibration*, 2008, Vol. 313, pp. 643-654.

10. Combes, S. A., & Daniel, T. L., "Flexural Stiffness In Insect Wings I. Scaling And The Influence Of Wing Venation", Journal of Experimental Biology, 2003, Vol. 206, pp. 2979-2987.

11. Combes, S. A., & Daniel, T. L., "Flexural Stiffness In Insect Wings II. Spatial Distribution And Dynamic Wing Bending", *Journal of Experimental Biology*, 2003, Vol. 206, pp. 2989-2997.

12. Combes, S. A., & Daniel, T. L., "Into Thin Air: Contributions Of Aerodynamic And Inertial-Elastic Forces To Wing Bending In The Hawkmoth Manduca Sexta", *Journal of Experimental Biology, 2003, Vol. 206*, pp. 2999-3006

13. Combes, S. A., & Daniel, T. L., "Shape, Flapping And Flexion: Wing And Fin Design For Forward Flight", *Journal of Experimental Biology*, 2001, Vol. 204, pp. 2073-2085

14. Cook,R.D., Malkus,D.S., Plesha,M.E., and Witt,R.J., Concept and Applications of Finite Element Analysis, 4th Ed., John Wiley & Sons, 2002.

15. Cooper, A. J., "Limitations of Bumblebee Flight Performance," PhD Thesis, University of Cambridge, 1993.

16. Daniel, I. M., Ishai, O., *Engineering of Mechanics of Composite Materials*, 2nd Ed., Oxford University Press, 2006.

17. *Draganflyer X6,* Draganfly Innovations, Inc., www.draganfly.com.

18. Gere, J. M., *Mechanics of Materials*, Thomson Brooks/Cole, 2004.

19. Gordon, J. E., *Structures, or Why Things Don't Fall Down*, University of Reading, De Capo Press, 1978.

20. Gogulapati, A., Friedmann, P.P., Shyy, W., "Nonlinear Aeroelastic Effects in Flapping Wing Micro Air Vehicles", 49th AIAA/ASME/ASCE/AHS/ASC Structures, Structural Dynamics, and Materials Conference, 2008, AIAA-2008-1817.

21. Hanrahan, S., Photo of a *Manduca Sexta*, Texas A&M University, Department of Entomology, 2006.

22. Herman, G. T., Fundamentals of Computerized Tomography, 2nd Ed., Springer, 2009.

23. Hodges, D. H., and Pierce, G. A., *Introduction to Structural Dynamics and Aeroelasticity*, Cambridge, 2002.

24. Jantzen, B., and Eisner, T., "Hind Wings are Unnecessary for Flight but Essential for Execution of Normal Evasive Flight in Lepidoptera," *Proceedings of the National Academy of Sciences*, 2008, Vol. 105, 16636, Num. 40.

25. Mengesha, T. E., Vallance, R. R., Barraja, M., and Mittal, R., "Parametric Structural Modeling of Insect Wings," *Bioinspiration and Biommetics*, 2009.

26. Meirovitch, L., *Fundamentals of Vibrations,* McGraw-Hill, 2001.

27. McMichael, J. M., and Francis, M. S., "Micro Air Vehicles – Toward a New Dimension in Flight," *Unmanned Systems*, 1997, Vol. 15, No. 3, pp.8-17.

28. Michelson, R. C., and Reece, S., "Update on Flapping Wing Micro Air Vehicle Research," 13th Bristol International RPV Conference, 1998.

29. Norris, A., *Investigation of Reinforced Membrane Wings for Use in Flapping Wing Micro Air Vehicles.* Air Force Institute of Technology, Dissertation Prospectus AFIT/GA/ENYDSY-09S, 2008.

30. Personal Communication, Asif Khan, Product Manager, Abaqus/CAE, Simulia Research and Development, Request for Enhancement (RFE) 11597, 2010.

31. Personal Communication, Captain Ryan O'Hara, PhD Student, Air Force Institute of Technology, 2010.

32. Personal Communication, Major Aaron Norris, PhD Student, Air Force Institute of Technology, 2009.

33. Raymer, D. P., *Aircaft Design: A Conceptual Approach*, 4th Ed., AIAA Education Series, 2006, pp. 620-636.

34. Saada, A. S., Elasticity: Theory and Applications, Krieger Publication Company, 1993.

35. Sims, J. R., "CoordGen," Jason R. Sims, Sole Proprieter, 2010.

36. Singer, P. W., *Wired for War: The Robotics Revolution and Conflict in the 21st Century.* Penguin, 2009. pp. 263-265.

37. Strang, G., Linear Algebra and its Applications, Thomson Brooks/Cole, 2006.

38. Tobias, A., "Experimental Methods to Characterize Nonlinear Vibration of Flapping Wing Micro Air Vehicles," Master's Thesis, Air Force Institute of Technology, 2005.

39. Weis-Fogh, T., "Quick Estimates of Flight Fitness in Hovering Animals, Including Novel Mechanisms for Lift Production," *Journal of Experimental Biology*, 1973, Vol 59, pp. 169-230.

40. Willmott, A. P., and Ellington, C. P., "The Mechanics Of Flight In The Hawkmoth Manduca Sexta, I. Kinematics Of Hovering And Forward Flight", *Journal of Experimental Biology,* 1997, Vol. 200, No. 21, pp. 2705-2722.

41. *Wing Geometry Definitions*, NASA Glenn Research Center, *http://www.grc.nasa.gov/WWW/K-12/airplane/geom.html*, 2009.

42. *X-Wing Research Vehicle*, EC86-33555-2, NASA Dryden Flight Research Center, 1986. *http://nix.larc.nasa.gov/info?id=EC86-33555-2&orgid=7*.

43. Zhao, L., and Deng, X., "Power Distribution in the Hovering Flight of the Hawk Moth *Manduca Sexta*," Bioinspiration and Biommetics, Num. 046003, 2009.

44. Zienkiewicz, O. C., and Taylor, R. L., The Finite Element Method for Solid and Structural Mechanics, 6th Ed., Elsevier Ltd., 2005.

REPORT DOCUMENTATION PAGE

Form Approved
OMB No. 074-0188

PLEASE DO NOT RETURN YOUR FORM TO THE ABOVE ADDRESS.

1. REPORT DATE *(DD-MM-YYYY)*	**2. REPORT TYPE**	**3. DATES COVERED** *(From – To)*
25-03-2010	Master's Thesis	Sep 2008 – March 2010

TITLE AND SUBTITLE

A Structural Dynamic Analysis of a *Manduca Sexta* Forewing

5a. CONTRACT NUMBER

5b. GRANT NUMBER

5c. PROGRAM ELEMENT NUMBER

6. AUTHOR(S)

Travis W. Sims, 2d Lt, USAF

5d. PROJECT NUMBER

5e. TASK NUMBER

5f. WORK UNIT NUMBER

7. PERFORMING ORGANIZATION NAMES(S) AND ADDRESS(S)

Air Force Institute of Technology
Graduate School of Engineering and Management (AFIT/ENY)
2950 Hobson Way, Building 640
WPAFB OH 45433-8865

8. PERFORMING ORGANIZATION REPORT NUMBER

AFIT/GAE/ENY/10-M22

9. SPONSORING/MONITORING AGENCY NAME(S) AND ADDRESS(ES)

Dr. Philip Beran, AFRL/RBSD
Air Force Research Laboratory, Air Vehicles Directorate
Wright-Patterson Air Force Base, OH 45433-7542

10. SPONSOR/MONITOR'S ACRONYM(S)

11. SPONSOR/MONITOR'S REPORT NUMBER(S)

12. DISTRIBUTION/AVAILABILITY STATEMENT

APPROVED FOR PUBLIC RELEASE; DISTRIBUTION UNLIMITED.

13. SUPPLEMENTARY NOTES

14. ABSTRACT

Micro air vehicles (MAVs) are intended for future intelligence, surveillance, and reconnaissance use. To adequately fulfill a clandestine capacity, MAVs must operate in close proximity to their intended target without eliciting counter-observation. This objective, along with DARPA's constraint of a sub-15 centimeter span, requires future MAVs to mimic insect appearance and flight characteristics. This thesis describes an experimental method for conducting a structural analysis of a Manduca Sexta (hawkmoth) forewing. Geometry is captured via computed tomography (CT), and frequency data is collected using laser vibrometry in air and vacuum. A finite element (FE) model is constructed using quadratic beams and general-purpose shell elements, and a linear dynamic analysis is conducted. A preliminary verification of the FE model is carried out to ensure the Manduca Sexta forewing is adequately characterized, providing a basis for future fluid-structural interaction computations. Included is a study regarding the aeroelastic effects on flapping-wing insect flight, and an analysis of the structural dynamic anomalies of conventional, flat, semi-rigid flapping wings.

15. SUBJECT TERMS

Micro Air Vehicle, MAV, Structural Dynamics, Finite Element, Laser Vibrometry, *Manduca Sexta*

16. SECURITY CLASSIFICATION OF:			**17. LIMITATION OF ABSTRACT**	**18. NUMBER OF PAGES**	**19a. NAME OF RESPONSIBLE PERSON**
a. REPORT	**b. ABSTRACT**	**c. THIS PAGE**			Dr. Anthony N. Palazotto, PE, ADVISOR
U	**U**	**U**	**UU**	136	**19b. TELEPHONE NUMBER** *(Include area code)* (937) 255-6565, ext 4599 (anthony.palazotto@afit.edu)

Standard Form 298 (Rev. 8-98)
Prescribed by ANSI Std. Z39-18